

PHYSICAL AND CHEMICAL PROCESSING METHODS FOR PRODUCING
NANOCRYSTAL FILMS WITH PROPERTIES BY DESIGN

A Dissertation

Presented to the Faculty of the Graduate School

of Cornell University

In Partial Fulfillment of the Requirements for the Degree of

Doctor of Philosophy

by

Benjamin Edward Treml

May 2016

© 2016 Benjamin Edward Treml

PHYSICAL AND CHEMICAL PROCESSING METHODS FOR PRODUCING NANOCRYSTAL FILMS WITH PROPERTIES BY DESIGN

Benjamin Edward Treml, Ph. D.

Cornell University 2016

As quantum dot (QD) synthesis techniques and device architectures advance, it has become increasingly apparent that new ways of connecting QDs with each other and the external environment are required in order to realize the considerable potential of QDs for optoelectronic applications. Throughout my PhD studies at Cornell, I have worked to establish the scientific and engineering foundation for processing techniques to produce designer materials from QD building blocks. Specifically, I have investigated two general processing methods, thermal annealing and solution based chemical treatments to remove or replace the insulating native ligands and produce electronically coupled thin films. In a series of studies on thermal annealing of QD films across 10 orders of magnitude in time, I show how nonequilibrium laser annealing over ns and μ s can be used to precisely control the structure of QD thin films to increase electronic coupling while maintaining quantum confinement, how *in situ* studies of QDs arranged in a periodic nanoreactor can shed light on QD fusion at the second to minute time scale, and how spatial temperature gradients during nonequilibrium laser annealing can be exploited to reveal that QD sintering is a thermally activated process with a constant activation energy over two orders of magnitude of QD growth rate. My work on

chemical processing of QD films focuses on low temperature solution processing methods. I demonstrate how simultaneous cation and ligand exchange at the surface of QDs can electronically couple and passivate QD films in a single step, leading to a 4 fold increase in Förster resonant energy transfer rate and order of magnitude reduction in trap density. Through controlled removal of ligands and post assembly QD growth, I show how building epitaxial bonds among QDs in a long range ordered assembly can lead to a ~3 order of magnitude increase in the mobility of carriers in QD films. This work is an illustration of how detailed understanding of the processing-structure-property relationships in QD assemblies over multiple length scales can produce functional thin films with properties by design. Further advances that build on this work and others will take full advantage of the unprecedented flexibility provided by the size tunable properties of QDs to expand the periodic table into another dimension and drive materials innovation.

BIOGRAPHICAL SKETCH

Benjamin Trembl was born in Green Bay, Wisconsin in 1989. As a result, he is a diehard Packers fan. In high school he developed a strong interest in science, the environment, and energy issues thanks to the influence and guidance of his teachers, specifically Dwight Will and Charles Frisk (the man, the myth, the legend).

The potential for nanotechnology to revolutionize energy applications attracted him to the Engineering Physics program at the University of Wisconsin-Madison. He graduated with a BS with Honors in Research in 2012. The EP program at Madison is a graduate school prep program that is roughly 1/3 each Mechanical Engineering, Physics, and Materials Science. Materials Science's interdisciplinary approach to problem solving focusing on controlling materials at the atomic level fascinated Ben, so he chose to pursue a PhD in Materials Science and Engineering at Cornell University.

At Cornell, Ben has worked in the laboratory of Prof. Tobias Hanrath studying nanocrystal thin films for use in energy applications, such as solar cells and light emitting diodes. He obtained his PhD in 2016.

Ben is married to Stephanie, a teacher who is blessed with seemingly endless patience for Ben's rambles about science. They have a dog named Rodger (after the Packers' QB) and together have spent their time in Ithaca hiking, wine tasting, playing soccer, and exploring the east coast.

To my wife, who moved 900 miles away from family and friends so that I could pursue my passion, and to my parents, who encouraged me to always think even if I wasn't thinking straight.

ACKNOWLEDGMENTS

First, I would like to thank my advisor, Prof. Tobias Hanrath. In all of my interactions with Prof. Hanrath, he has displayed an endless enthusiasm for science and research that is truly contagious and has certainly infected me. I highly value the freedom he gave me to follow the science where it led regardless of if it followed the original aim of the project. I cannot imagine getting to where I am today as a scientist without his guidance and input, and I will always be grateful for the impact he has had on my career.

I would also like to thank the other two members of my committee, without collaborating with them and their graduate students this dissertation would not exist. Prof. Lena Kourkoutis and her course on nanocharacterization emphasized that in order to get the most out of an instrument you need to understand how it works, which I have taken to heart. Her student, Ben Savitzky has provided me with too many atomic resolution images of my nanocrystals, which is a great problem to have. Even though nanoparticles are not his area of expertise, Prof. Michael Thompson was always willing to talk through a narrative with me, identify the weak points and provide suggestions to strengthen it. Bob Bell and Alan Jacobs are laser wizards, and without their hard work calibrating and maintaining the laser spike annealing system, my thermal annealing work would be significantly poorer.

I have a special place in my heart for the Cornell High Energy Synchrotron Source and all of the scientists, engineers, and staff that keep it (mostly) up and running. CHESS is a large reason that I joined the Hanrath group, as they needed another warm body for a CHESS run in early October 2012. Having a synchrotron on campus is a phenomenal resource, and the ability to use it two or three times a year allowed me to try riskier and more interesting experiments than if my access to a synchrotron were

more limited. I want to specifically thank Dr. Detlef Smilgies for being so helpful and patient with my GISAXS/WAXS experiments. He is a phenomenal resource and always seems to have an idea for how to kick an experiment up to 11.

I would like to thank Prof. Frank Wise and his former student Dr. Jun Yang for their help with measurement and interpretation of PL and TRPL of my nanocrystal films. I would like to thank Prof. Paulette Clancy and her postdoc Dr. Binit Lukose for performing MD simulations of my binary nanocrystal superlattices. Prof. Kit Umbach was very helpful and accommodating when I wanted to use the Raman microscope to measure the PL of my rainbow stripes, without his help that project would never have gotten off the ground. I want to thank the whole CCMR staff for all of the training, troubleshooting, and advice they have given me. In particular I would like to thank John Grazul, who has probably had to put up with most of my questions and mistakes. He still owes me a coffee and a cookie from one of his email contests.

I would like to thank the rest of the Hanrath lab: Ben Richards, Kaifu Bian, Kevin Whitham, Will Baumgardner, David Moore, Victor Lambert, Jessica da Silva, Kevin Kimura, Doug Nevers, Curtis Williamson, Ali Tirmzi, and Eliad Peretz, who have critiqued my work and provided suggestions to improve it in and out of group meetings. The group is a concentration of nanomaterials experts, and convincing them of my interpretation of data was a crucial high pass filter. In particular, I would like to single out Dr. Will Baumgardner who got me oriented in the lab, taught me how to make NCs, and mentored me as a first year graduate student. Thanks to Will I was able to hit the ground running.

TABLE OF CONTENTS

1. INTRODUCTION	1
1.1 Nanocrystals as Artificial Atoms	1
1.2 Primary Structure: Making the ‘Atom’	4
1.3 Secondary Structure: Designing the ‘Atom’	6
1.3.1 Tuning Energy Levels in Semiconductor Nanocrystals	7
1.3.2 Heterostructured Nanocrystals	9
1.4 Tertiary Structure: Building Designer Materials	11
1.4.1 Control over Superlattice Structure	11
1.4.2 Control over Nanocrystal Bonding	14
1.5 Quaternary Structure: Exploiting Designer Materials in Devices	19
1.5.1 Photovoltaics	19
1.5.2 Photodetectors	22
1.5.3 Thermoelectrics	24
1.5.4 Electroluminescent Light Emitting Diodes	26
1.5.5 Nanocrystals as Downconverters	27
1.6 Structure of the Dissertation	28
REFERENCES	31
2. PROCESSING-STRUCTURE-PROPERTY RELATIONSHIPS IN LASER ANNEALED PbSe NANOCRYSTAL THIN FILMS	35
2.1 Introduction	36
2.2 Structural Characterization of Laser Annealed Films	41
2.3 Thermal Transport in LSA and PLA Films	43
2.4 Property Control via Structure Control	46
2.5 Conclusions	49
REFERENCES	51
3. CONNECTING THE PARTICLES IN THE BOX - CONTROLLED FUSION OF HEXAMER NANOCRYSTAL CLUSTERS WITHIN AN AB₆ BINARY NANOCRYSTAL SUPERLATTICE	53

3.1 Introduction	54
3.2 GISAXS Characterization of Assembled BNSLs	57
3.3 Molecular Dynamics Simulations	60
3.4 Structural Transformation of the PbS Hexamer and the BNSL During Thermal Annealing	63
3.5 Laser Annealing of BNSLs	71
3.6 Conclusions	72
REFERENCES	74

4. μ -RAINBOW: CdSe NANOCRYSTAL PHOTOLUMINESCENCE

GRADIENTS VIA LASER SPIKE ANNEALING FOR KINETIC

INVESTIGATIONS AND TUNABLE DEVICE DESIGN 76

4.1 Introduction	77
4.2 Characterization of Single Laser Scans	81
4.3 Kinetic Analysis of Nanocrystal Fusion	84
4.4 Tunable Emission from NC films	88
4.5 Conclusions	90
REFERENCES	92

5. SIMULTANEOUS LIGAND AND CATION EXCHANGE IN PbSe/CdSe

NANOCRYSTAL FILMS 94

5.1 Introduction	95
5.2 Surface Limited Cation Exchange	97
5.3 Simultaneous Ligand Exchange	101
5.4 Probing Transport via Photoluminescence	102
5.5 Conclusions	107
REFERENCES	109

6. SUCCESSIVE IONIC LAYER ABSORPTION AND REACTION FOR POST-ASSEMBLY CONTROL OVER INORGANIC BONDS IN LONG RANGE ORDERED NANOCRYSTAL FILMS	112
6.1 Introduction	113
6.2 Effect of SILAR on CBC Structure and Optical Properties	115
6.3 Quantification of Structural Changes	117
6.4 Effect of SILAR on Transport Properties	120
6.5 Conclusions	123
REFERENCES	124
7. A QUANTITATIVE FRAMEWORK FOR EVALUATING SEMITRANSSPARENT PHOTOVOLTAIC WINDOWS	126
7.1 Introduction	127
7.2 Developing a Quantitative Framework for stPV	128
7.3 Optimization of Spectrally Selective stPV	131
7.4 Conclusions	134
REFERENCES	137
8. FUTURE WORK AND CONCLUSIONS	138
8.1 Laser Annealing for White Light LEDs	139
8.2 Improving Confined-but-Connected Films	141
8.3 Expanding the stPV Model	143
8.4 Conclusion	143
REFERENCES	145
A. SUPPLEMENTARY INFORMATION: PROCESSING-STRUCTURE-PROPERTY RELATIONSHIPS IN LASER ANNEALED PbSe NANOCRYSTAL THIN FILMS	146
A.1 Advice for Students	146

A.2 Materials and Methods_____	147
A.3 Lower Magnification SEM Images of Annealed Films _____	149
A.4 Details of the PLA Thermal Transport Model_____	150
A.5 Detailed Relationship Between LSA temperature and NC Film Morphology_____	151
A.6 Electrical Conductivity Measurements_____	152
REFERENCES_____	154
B. SUPPLEMENTARY INFORMATION: CONNECTING THE PARTICLES IN THE BOX-CONTROLLED FUSION OF HEXAMER NANOCRYSTAL CLUSTERS WITHIN A AB₆ BINARY NANOCRYSTAL SUPERLATTICE	
155	155
B.1 Advice for Students_____	155
B.2 Materials and Methods_____	156
B.3 Single Component vs Binary Superlattices_____	158
B.4 Molecular Dynamics Simulations_____	159
B.5 Rearrangement of Nanocrystals After Annealing_____	162
REFERENCES_____	163
C. SUPPLEMENTARY INFORMATION: μ-RAINBOW: CdSe NANOCRYSTAL PHOTOLUMINESCENCE GRADIENTS VIA LASER SPIKE ANNEALING FOR KINETIC INVESTIGATIONS AND TUNABLE DEVICE DESIGN_____	
164	164
C.1 Advice for Students_____	164
C.2 Materials and Methods_____	165
C.3 Photoluminescence Sizing Curve_____	166
C.4 Laser Stripe Annealing of Larger CdSe NCs_____	168
C.5 Calculation of Thermal Diffusion Length_____	169
C.6 Calculation of Emission Position for a Partially Fused Dimer_____	170

C.7 Second Quantized Fusion Event_____	171
C.8 Photoluminescence Intensity_____	172
REFERENCES_____	175
D. SUPPLEMENTARY INFORMATION: SIMULTANEOUS LIGAND AND CATION EXCHANGE IN PbSe/CdSe NANOCRYSTAL FILMS_____	176
D.1 Advice for Students_____	176
D.2 Materials and Methods_____	177
D.3 Composition of NC Film after Cation Exchange_____	179
D.4 Kinetics of Cation Exchange_____	180
D.5 Transport of Excitons in Mixed Films_____	181
D.6 Change in Förster Radius Following Cation/Ligand Exchange_____	182
D.7 Cation/Ligand Exchange with Other Cations_____	183
REFERENCES_____	185
E. SUPPLEMENTARY INFORMATION: SUCCESSIVE IONIC LAYER ABSORPTION AND REACTION FOR POST-ASSEMBLY CONTROL OVER INORGANIC BONDS IN LONG RANGE ORDERED NANOCRYSTAL FILMS	
E.1 Advice for Students_____	186
E.2 Materials and Methods_____	187
E.3 Additional TEM Images_____	189
E.4 Details of EELS Analysis_____	191
E.5 Transport in Se Terminated NC Films_____	192
REFERENCES_____	195
F. INCOMPLETE AND UNPUBLISHED EXPERIMENTS_____	196
F.1 Nanoparticle Epitaxy_____	196
F.2 Self-Striping Nanocrystal Inks_____	198
F.3 Inductive Heating of Binary Nanocrystal Assemblies_____	199

F.4 Confined-but-Connected Film Formation on PEG Functionalized	
Substrates_____	200
F.5 Magic to Magic Cation Exchange_____	202
REFERENCES_____	204

CHAPTER 1

INTRODUCTION

1.1 Nanocrystals as Artificial Atoms

One of the most attractive facets of nanotechnology are the novel behaviors and properties exhibited by materials with nanoscale dimensions. Specifically for nanocrystals (NCs), this often manifests itself as size dependent optical, electronic, or magnetic properties. Since the initial studies of colloidal CdS and ZnS NCs by Brus and coworkers in the mid-80's^{1, 2}, fundamental understanding of these nanoscale phenomena has advanced rapidly. While development of new synthesis techniques and fundamental studies of isolated NCs continue, an emphasis is now being placed on formation of and control over assemblies of NCs at the μm to cm length scale for integration into real world devices³⁻⁷.

Broadly, the properties of a material are a complicated interrelated function of the energy levels of the constituent atoms, the bonding interactions among atoms, and the periodic structure, or lack thereof, that that atoms adopt. Typically, these factors are highly coupled; the electronic configuration of an atom influences the orbitals available for bonding, which in turn place constraints on the crystal structure a material can adopt. The ability to change the properties of a NC independent of its chemical composition makes NCs attractive as “artificial atoms” for producing designer materials. In assemblies of NCs these factors can be decoupled and independently manipulated through application of established processing-structure-property relationships⁸. NCs

and their size tunable properties provide an opportunity to expand the periodic table and provide a new avenue for addressing materials related challenges.



Figure 1.1: Control over the properties of NCs via structure control of the individual NC provides scientists and engineers access to additional dimensions of the periodic table for producing materials with properties by design.

It is helpful to separate the structure of NC based designer materials into several orders of structure, analogous to the classification of protein structure⁹. At the lowest, primary level of structure we can precisely control the atomic composition of NCs. A wide range of materials are able to be synthesized in NC form, including metals, semiconductors, complex oxides, and even hybrid organic/inorganic crystals such as methylammonium perovskites¹⁰⁻¹². At the secondary level of order, we consider the isolated NC. Here, for a given composition the size and shape of a NC can be controlled, allowing for exploitation of the size dependent properties of nanomaterials¹³. Additionally, completely new compositions of matter can be created based on careful

manipulation of primary structure in a single NC, such as core-shell, dot-in-rod, Janus, or other even more complicated structures¹⁴⁻¹⁶.

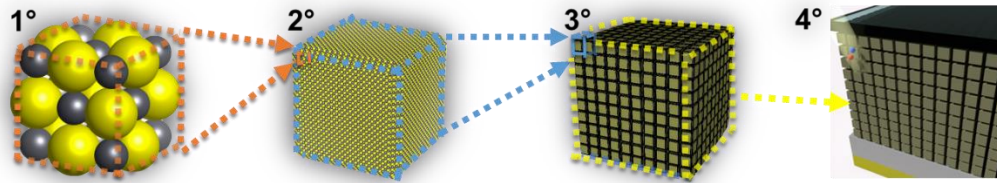


Figure 1.2: Four levels of control over nanocrystal thin films. From left to right, crystal structure, NC size and shape, supercrystal structure and bonding, and integration into devices.

At the tertiary level of order, the precisely controlled NC building blocks can be assembled into functional thin films accessible at the macroscale level^{8,17}. The structure of these assemblies is highly dependent on the interactions among NCs during assembly as well as the method of assembly¹⁸⁻²⁰. Additionally, the properties of these films can be tuned via careful control over the “bonding” between NCs via control over the distance between NCs in the assemblies^{21,22}. The specific nature of the bonding, and the required interparticle spacing depends critically on the specific particles being used and property or application being studied. For example, while solar cells and LEDs have essentially the same device structure, the requirements for electronic coupling among NCs in the active layers are different²³. As with secondary structure, precise control at the prior level enables novel material compositions at the tertiary level. Binary and ternary nanocrystal assemblies can present novel collective properties beyond the sum of their parts. Lastly, at the quaternary level of structure, these functional thin films can be combined with other materials to produce prototype devices

that take advantage of the precisely programmable properties of NC assemblies to enhance device performance.

1.2 Primary Structure: Making the ‘Atom’

The promise of novel properties at the nanoscale and general interest in nanoscience has led to the development of a large and ever growing library of nanomaterials that can be easily synthesized²⁴. There is a corresponding large variety of synthesis methods developed to precisely control the reaction products or use cheaper or less dangerous chemicals. For colloidal NCs, the most common synthesis method, and the one used for all of the NCs studied in this work is the hot injection synthesis^{5, 24-26}. The hot injection synthesis is outlined schematically in Figure 1.3. Figure 1.3a shows a typical reaction setup using a three neck flask kept under an inert environment filled with a high boiling point solvent and a syringe loaded with precursor ready for the injection.

The change in supersaturation during a reaction in the La Mer model of colloidal growth is shown in Figure 1.3b. In region I, precursors are injected into a three neck flask containing hot solvent, stabilizing ligands, and frequently other precursors. The precursor(s) degrade into a monomer species that quickly surpasses a critical supersaturation level in the hot solvent. This leads to homogeneous nucleation of nanoparticle seeds in region II until the monomer concentration drops below the nucleation threshold. After nucleation, particles continue to grow in region III via addition of monomer units until the supply of monomer has been exhausted or the solution temperature is decreased to quench the reaction. Particle size can be tuned through changing the temperature of the reaction, which affects the number of nuclei formed as well as the growth rate of the particles, and the growth time.

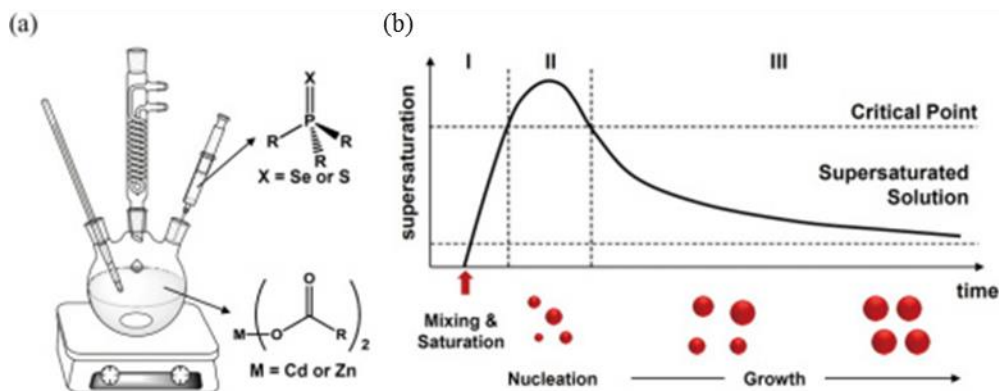


Figure 1.3: Nanocrystal Synthesis a) Schematic of a synthesis in a 3 neck flask. Anionic precursors are injected rapidly to cause a discrete nucleation event. b) The La Mer model of colloidal particle growth. Adapted from ⁵ Copyright 2012 OSA Publishing

For the study of NCs, as well as many applications it is desirable to have a narrow size distribution. NCs are generally considered monodisperse if the standard deviation of the particle size distribution is 5% or less. This corresponds to lattice constant or less deviation in particle diameter for NCs around 10 nm or smaller. Narrow size distributions are achieved through a combination of precise synthesis methodologies involving rapid injection of precursors and quenching of the reaction, and size focusing during the growth of NCs. Burst nucleation and rapid quenching of growth solutions ensure that all particles have nearly identical growth histories. Size focusing during growth of NCs also helps to produce monodisperse NCs^{25, 27}. In a growth solution of NCs dilute enough that the NC do not interact with one another, the growth rate can be described as diffusive flux of monomer to the NC surface. As the size of a NC increases, the flux of monomer to the particle increases with the surface area of the particle (i.e. R^2), but the total amount of monomer required to grow radially increases with R^3 . As a result, smaller particles grow faster than larger particles, damping out initial inhomogeneities in the particle size distribution. In order to prevent Ostwald ripening syntheses are typically quenched via injection of cold solvent or

submersion of the reaction vessel in water before all of the free monomer has been consumed²⁶.

After a synthesis has ended the particles must be separated from the high boiling point solvent and unreacted precursor via precipitation with an antisolvent. The most common method is to add ethanol to the reaction mixture, causing the nanocrystals to “crash out” of solution. The NCs can then be separated via centrifugation, redispersed in hexane and washed again. Typically, this procedure is repeated three times. Other solvent/antisolvent pairs can be used in order to prevent degradation of the NC surface. Acetonitrile/toluene is one of the gentlest solvent/antisolvent pairs, but may not be as effective at removing unreacted precursors^{28, 29}. Air sensitive NC such as PbSe or PbS should be stored in the glovebox as soon as possible after synthesis in order to avoid oxidation. If the NC will be used in applications where the results are highly sensitive to the quality of the NC surface, such as electronic transport measurements or oriented attachment, NC can be synthesized, washed, and stored in a glovebox by adapting the general procedure outlined above appropriately. See Appendices D and E for details regarding PbSe glovebox synthesis in the Hanrath Lab.

1.3 Secondary Structure: Designing the ‘Atom’

The precise control over NC’s enabled by the synthesis method detailed in the previous section enables scientists and engineers to control the size and shape of NCs, as well as spatially control the crystal structure or composition. This gives us access to an expanded periodic table full of “artificial atoms” with properties that are tunable and inaccessible in other systems. The mechanisms for the size tunable properties generally fall into two categories, properties like enhanced catalytic activity and superparamagnetism result from the changing surface area to volume ratio as particle sizes shrink³⁰⁻³³. Assuming that the outermost .3 nm shell of a NC, approximately an

Au-Au or Pb-Se bond length, is a reasonable approximation for the surface of a nanocrystal, then the percentage of surface atoms goes from 2% to 17% to 38% as the size of a nanocrystal is reduced from 100 nm to 10 nm and 4 nm. This has implications for the properties and performance of NC based materials beyond just property control. When over 30% of a material is comprised of surface atoms, understanding and controlling the surface chemistry of NCs becomes critical.

1.3.1 Tuning Energy Levels in Semiconductor Nanocrystals

Novel optical and electronic properties, such as the size dependent bandgap of semiconductor NCs (also known as quantum dots, QDs) and tunable plasmon resonance of metal NCs, frequently result from quantum confinement effects^{1, 34, 35}. Nearly all NCs studied in this work are QDs, so the underlying physics of their novel size dependent properties merit further discussion. In semiconductors, absorption of a photon with $h\nu > E_g$ leads to generation of a bound electron-hole pair, also known as an exciton. The exciton forms a hydrogenic state where electrons and holes are separated by a distance known as the Bohr exciton radius, which is determined using the Bohr model of a hydrogen atom and accounting for the effective masses of the electron and hole as well as the dielectric constant of the semiconductor³⁶. Typical exciton binding energies in bulk semiconductors are on the order of a few meV and so excitons readily dissociate into free carriers at room temperature.

When a semiconductor is reduced in size, such that the radius of the semiconductor is comparable to the Bohr exciton radius, the bandgap of the semiconductor NC increases and both the absolute position and spacing between energy levels change^{37, 38}. As a result, semiconductor NCs frequently exhibit a series of discrete, isolated energy levels like a molecule rather than the continuum of energy levels that make up an energy band in a bulk semiconductor.

The quantum mechanical effects that lead to changing energy levels and increased separation between levels can be understood by considering the electron and hole as quasiparticles in a 3D box. Critical assumptions include: choosing an s-like wavefunction for the electron and hole, assuming a spherical NC with an infinite potential outside the NC, and taking the effective masses from the edge of the bulk conduction and valence bands. The resulting analytical solution is similar to the simple 1D case covered in a basic quantum mechanics course, reducing the size of the box leads to an increased energy for the ground state as well as larger separation between higher energy states^{35, 39}. More detailed models can include additional details from the bulk band structure and provide more accurate calculations for a specific NC under consideration⁴⁰.

In addition to the quantum mechanical effect, forcing an electron and hole closer together than the Bohr exciton radius leads to an increase in the attractive Coulombic interaction between particles. This interaction works in opposition to the quantum confinement effect and decreases the bandgap of the NC. Of particular note for optoelectronic applications of semiconductor NCs, the increased Coulombic interaction between electron and hole creates an increased exciton binding energy and hence presents a barrier for exciton dissociation into free carriers. The total effect of these two phenomena is summarized in equation 1.1.

$$\Delta E = \frac{\hbar^2 \pi^2}{2R^2} \left[\frac{1}{m_e} + \frac{1}{m_h} \right] - \frac{1.8e^2}{\epsilon R} \quad \text{Eq. 1.1}$$

Where ΔE is the change in bandgap relative to the bulk material, $m_{e(h)}$ is the effective mass of the electron (hole), R is the radius of the NC, and ϵ is the dielectric permittivity of the NC. The first term represents the quantum confinement energy, and the second term represents the Colombic energy. The relative strength of the R^{-2} and R^{-1} terms depend on the precise NC under consideration, but generally the effects are of comparable magnitude and most NCs show an $\sim R^{-1.5}$ dependence of the band gap on

NC size. This is detailed for PbSe particles in Fig 1.4. The lead chalcogenides have some of the largest Bohr exciton radii, 46 nm for PbSe and 18 nm for PbS⁴¹. This makes the bandgap highly sensitive to changes in the QD size and makes the lead chalcogenides an interesting experimental platform for fundamental studies of quantum size effects in NCs.

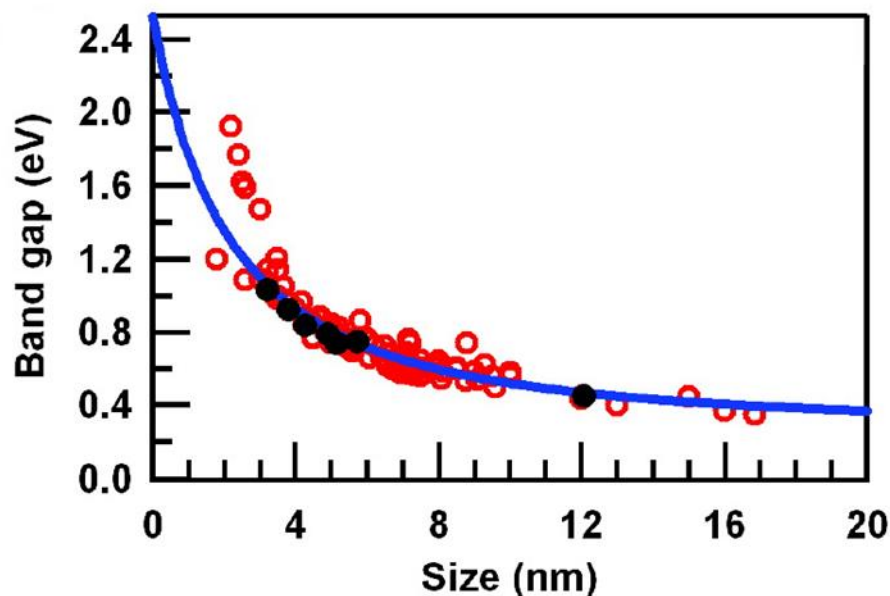


Figure 1.4: Size (diameter) dependence of the bandgap of spherical PbSe nanocrystals. Adapted from ⁴² Copyright 2007 American Chemical Society

1.3.2 Heterostructured Nanocrystals

In addition to the tunable bandgap and energy levels of semiconductor NCs, they are also interesting as “artificial atoms” due to the ability to make novel heterostructures. The creation of heterostructures with properties beyond those obtainable from single material NCs stems from the precise control developed at the primary level of NC structure. The simplest, and most common form of heterostructures for QDs are core-shell QDs where a QD of interest is surrounded by another semiconducting material in a shell that can range in thickness from a single monolayer to several times the radius of the core^{14, 43-46}. Heterostructures are classified as either type I or type II based on the

energy level alignment⁴⁷. Type I heterostructures have a straddling bandgap, resulting in confinement of both electrons and holes to the same, lower bandgap material. In contrast, type II heterostructures have an offset bandgap where electrons reside preferentially in one semiconductor and holes in the other.

Type I core-shell heterostructures are commonly used in order to improve the quantum yield of QDs for luminescent applications. The shell material passivates the surface of the core, moving dangling bonds that can act as traps and degrade the properties of the QD to the edge of the shell material. As the shell is a higher bandgap, the wavefunctions of excitons generated in the core are less likely to interact with dangling bonds at the surface, reducing nonradiative decay in these structures.

Beyond using heterostructures to passivate surfaces, reduce trapping, and improve the properties of the core QD, more complicated structures can be created that have novel properties inaccessible to other materials systems. Nanorods can be grown around a QD to produce dot-in-rod structures with liquid-crystalline like assembly properties and anisotropic absorption properties^{15, 48}. In addition, the size tunable energy levels of the core can be exploited to tune the energy alignment between core and shell such that a type I alignment in the bulk can be turned into a quasi-type II alignment that has been shown to stabilize high energy holes and lead to record carrier multiplication performance⁴⁹.

The ability to produce building blocks with size tunable properties as well as new properties based on careful heterostructuring of materials provides a wide range ‘designer atoms’ for assembly into functional thin films. This new, expanded periodic table contains additional dimensions full of promise for materials innovations.

1.4 Tertiary Structure: Building Designer Materials

In order to take advantage of the expanded periodic table enabled by precise control over NC structure at the secondary level, we must have an equally detailed understanding of the processing-structure-property relationships in NC films that can meaningfully interact with the outside world. Control of the structure of NC films at the tertiary level allows for tuning the structure and strength of interactions among the assembled NCs independent of the properties of the “designer atoms”. Long range order in NC assemblies has been sought after, as the periodic arrangement of NCs in a film is expected to lead to novel collective properties such as minibands⁵⁰. Coupling between NCs in a film is critical for enabling carrier transport in optoelectronic applications that seek to take advantage of the tunable bandgap of NC films. The ability to control both the structure and bonding in a NC assembly independent of one another provides the opportunity to create materials with widely different properties starting from the same NC building blocks.

1.4.1 Control over Superlattice Structure

NCs can be assembled into a wide range of superlattice crystal structures. The precise structure and degree of long range ordering in a NC assembly is a function of the interparticle interactions and the film formation method⁵¹. A combination of entropic and enthalpic interactions drive NC assembly. Entropic factors favor structures with the highest packing density due to excluded volume effects⁵². Enthalpic interactions in NCs are dominated by ligand-ligand interactions. With a full ligand shell, NCs interact like soft spheres, and so prefer to pack in FCC structures. Changing the ligand-ligand interactions, either through using a poor solvent or reducing the ligand coverage can cause the NCs to interact anisotropically due to the underlying faceted

crystal⁵³. This leads to a wider range of structures such as assemblies with BCC and tetragonal symmetry.

Beyond single component assemblies, a wide diversity of binary and ternary NC assemblies can be accessed through careful control of the relative NC sizes and “stoichiometry” of a NC solution. Similar to how binary compounds such as NaCl exhibit collective properties distinct from their constituent atoms, these binary NC superlattices exhibit phenomena such as magnetoresistance,⁵⁴ catalytic activity,⁵⁵ and conductivity⁵⁶ greater than the sum of the constituent parts.

NC films can be formed in a variety of ways. As a general rule, the longer NCs are given to assemble, the higher the amount of order in the resulting NC film. The largest, most well-ordered single supercrystals are formed through diffusion of an antisolvent into a NC suspension^{57,58}. However, this approach is not conducive to large area, high speed fabrication of NC films as would be necessary for deployment in commercial applications. Instead most NC films, and all films studied in this work, are produced using solvent evaporation driven self-assembly. The simplest method is dropcasting, simply allowing a droplet of NC ink to evaporate on a substrate. Despite its simplicity, when the solvent evaporation rate is well controlled, via careful choice of solvent or drying in a saturated vapor environment well-ordered films can be produced^{59,60}. Dropcasting is an attractive film fabrication method for applications that require precise spatial control over composition at the 3° (NC film) and 4° (Device) level, as inkjet printing and some forms of 3D printing are just dropcasting with small droplets.

Spincoating is another common film formation method, used frequently in the formation of prototype devices⁶¹⁻⁶³. The process is taken directly from photolithography, but instead of forming a uniform layer of photoresist, a solution of NCs in a fast drying solvent is used. The thickness of the resulting films can be tuned by the spin speed, NC concentration, and solvent evaporation rate. Film thicknesses are

generally between 20 and 100 nm, and often several spin coating cycles are required to build up a thick and uniform film. While spin coating is fast, it generally produces films with a low degree of ordering and is very material expensive, as most NC ink is spun off of the substrate rather than deposited.

Drag coating and its cousin doctor blading are solution processing techniques adopted from roll to roll manufacture of thin films, such as photographic film⁵¹. Because it is adopted from processing methods used in roll to roll manufacturing, processing-structure relationships established in drag coated films may translate to higher throughput applications. In addition, drag coating is a material efficient coating method. A flat blade, such as a Si wafer or glass slide is held just above the surface of the substrate to be coated. A small amount of NC ink is placed on the substrate in contact with the blade, forming a meniscus. As the blade is dragged across the substrate, the meniscus of NC solution leaves a thin trail that dries quickly. Film thickness can be tuned through control over the concentration of NC in the ink as well as the drag coating speed.

In order to produce highly ordered thin NC films, liquid interface assembly can be used. In this method, a small volume of NC solution is dispensed on the surface of an immiscible liquid. The NC solution spreads out producing a uniform NC film in thickness ranging from a submonolayer to ~10 NCs (~50 nm) thick. The solvent evaporation rate is controlled by covering the trough used to contain the subphase. NCs on a liquid subphase have more mobility compared to NCs assembled on a solid substrate, and as a result the film can solvent anneal during the slow drying process. This method has been successful in producing single, binary, and ternary films with impressive long range ordering⁶⁴⁻⁶⁶.

1.4.2 Control over Nanocrystal Bonding

For optoelectronic applications of NC films, the electronic coupling among NC is critically important. However, the requirements for electronic coupling can vary depending upon the specific application required. This is an opportunity where the ability to independently tune the properties of the “artificial atoms” and the bonding in a material provides scientists and engineers the opportunity to produce designer solids precisely tailored for a specific application.

The ligands that enable colloidal NCs to stay suspended in solution pose a problem for electron conduction when NCs are assembled into a solid film. Transport between NCs in films commonly occurs via tunneling from NC to NC²¹. The tunneling rate between two NC can be described by equation 1.2.

$$\tau = \tau_o \exp(-\beta l) \quad \text{Eq. 1.2}$$

Where τ is the tunneling rate, τ_o is an attempt frequency, β is a decay constant related to the barrier height, and l is the surface to surface NC spacing.

The ligands used in synthesis, often termed “native ligands”, are generally about 2 nm long, which leads to large tunneling barrier widths, and as a result insulating films. Many processing methods have been investigated in order to deal with the ligand issue. The most common method is ligand exchange, where a chemical displacement reaction occurs resulting in either reduced interparticle spacing or barrier height. Physical processing methods such as thermal annealing and high pressure treatments, which aim to couple nanocrystals inorganically, have also been investigated with varying degrees of success⁶⁷⁻⁶⁹.

Ligand Exchange

In order to exchange the native ligands for a new, more compact ligand that will enhance transport, an as deposited NC film is exposed to a solution containing a large

excess of the new ligand dissolved in a solvent that the NCs are not soluble in. There are several chemical reactions that can occur at the surface of a NC during ligand exchange depending upon the precise chemical nature of the incoming ligand. Ligands can be categorized as X, L, or Z type using the covalent bond classification method⁷⁰. X type ligands are one electron donors (ex: carboxylate anions), L type ligands are neutral Lewis bases (ex: amines), and Z type ligands are neutral Lewis acids (ex: metal-carboxylate complexes). As synthesized NCs are often cation rich, with a ligand shell of metal-carboxylates^{28, 29, 42}. The mechanism of ligand displacement for all three categories of ligands is shown in Figure 1.5. Most common ligand exchange reactions are X-type ligand exchanges, where a hydrogen is transferred from a thiol, carboxylic acid, or alcohol to the native X-type ligand.

A. classes of ligand exchange reactions

X-type



L-type



Z-type



B. Z-type ligand displacement (L-promoted)



M = Cd, Pb, etc.

E = S, Se

X = O₂CR, Cl, SR, etc.

L = PR₃, NH₂R, etc.



Figure 1.5: Schematic of ligand exchange at the surface of a nanocrystal. Nanocrystals are assumed to initially be terminated by X-type ligands like oleate. From ²⁹ Copyright 2013 American Chemical Society

The large excess of ligands in solution, along with differences in binding energy between the incoming and outgoing ligands leads to a fast exchange⁷¹. Typical ligand exchange times are on the order of 30 s. As the long native ligands are removed, the film compacts and NCs move closer to each other⁷². This generally disrupts the long range order of the NC films and leads to cracking. As a result, assembly of functional films for devices often follows a layer by layer approach, where film formation and ligand exchange steps are alternated until a desired film thickness is reached.

While ligand removal most commonly seeks to reduce the tunneling distance in a process that can be completed in a short time, other approaches have been investigated with interesting results. Rather than try to enhance tunneling by reducing the barrier width, the native ligands can be exchanged to molecules with a HOMO or LUMO level that lines up with the edge of the valence or conduction band edge energy of the NCs⁷³. This is made easier by the size dependent energy levels of NCs, which can be tuned to optimize the energy level alignment. As resonant energy transfer through the linking molecules aids conduction without the need for film compaction, these films simultaneously exhibit long range order and hole mobilities about an order of magnitude larger than non-resonant ligands of comparable length^{21,73}. Another alternative is to use lower concentrations of ligands in solution, and perform the ligand exchange on thicker films for longer times. As ligand exchange slows down, the resulting films retain more long range order while ending with approximately the same interparticle spacing⁷².

Removal of surface ligands can produce surface trap states which degrade the performance of NC films integrated into devices⁷⁴⁻⁷⁶. Understanding and repairing or preventing surface traps has been an avid topic of research in the community. The chemical processing methods developed to passivate surface traps, such as metal halide treatments, have been responsible for a significant increase in NC solar cell device efficiencies over the last several years^{62,77}.

Thermal Annealing

Rather than remove the insulating native ligands through chemical means, researchers have also investigated thermal annealing. The potential advantage of thermal annealing is the formation of inorganic connections between NCs, leading to a simultaneous reduction in both the tunnel barrier height and width. A series of studies on thermal annealing of NC, including *in situ* TEM and small angle X-ray scattering have identified a three step process for NC fusion⁷⁸⁻⁸². The first step is degradation of the ligand shell, which provides steric separation between the NCs. Following ligand degradation, NCs come into contact and form a neck or bridge between particles. This step may involve translation or rotation of the NCs in order to reach a relative orientation that is favorable for fusion. Lastly, the two particles rapidly fuse together via surface diffusion of atoms. These three steps are illustrated in Fig 1.6.

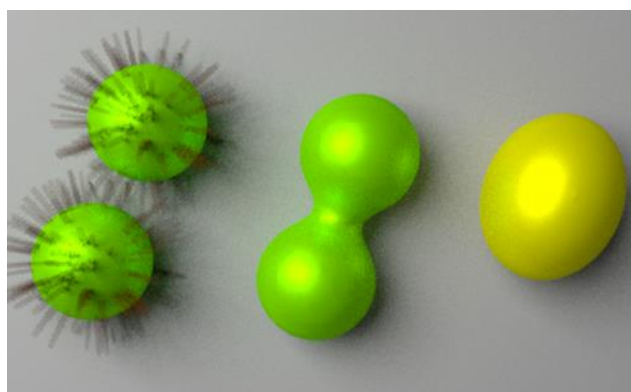


Figure 1.6: The three step process for NC fusion during thermal annealing. From left to right: Ligand degradation, neck formation, and complete fusion to form a new NC

It can be difficult to control thermal annealing in order to produce functional coupled NC thin films. After NCs have undergone the three step sintering process detailed above, their ligands have already been degraded, removing one barrier to

increased sintering. *In situ* TEM studies of thermal annealing have seen a 1-2-4 pattern of NC fusion, where “activated particles” that have already undergone fusion to form a dimer NC rapidly fuse together to form a particle with the volume of 4 initial particles^{78, 83}. The potential for NC fusion to continue uncontrollably after ligand removal makes thermal processing difficult to control, as rapid sintering and particle growth leads to loss of the precisely programmed properties of “artificial atoms”. In studies of thermal annealing of NC films on the minute to hour time scale, there is a narrow temperature range available where NC fuse slightly, but do not lose their quantum confined properties all together. Figure 1.7 illustrates the sensitivity of PbSe NC to changes in thermal processing temperature.

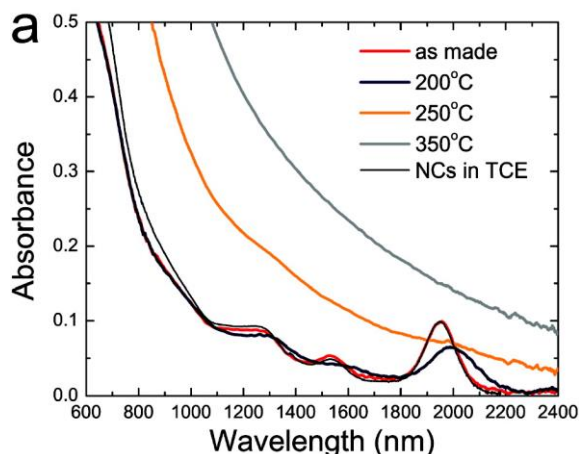


Figure 1.7: Absorption spectra of NC films annealed for 1 hour. The slight redshift in excitonic peak at 200 °C indicates limited fusion among particles. Annealing at a higher temperature obliterates all quantum confined properties due to excessive fusion. Adapted from ⁸⁴ Copyright 2008 American Chemical Society

One way to address the issue of unwanted particle sintering and the corresponding unwanted change in particle properties is to move to rapid thermal annealing approaches in an effort to kinetically trap NCs in a partially fused state. Efforts towards the goal of producing electronically coupled NC films without complete

film coalescence and loss of quantum confined properties are described in detail in Chapter 2.

1.5 Quaternary Structure: Exploiting Designer Materials in Devices

Having control over the structure and properties of NC films at the three levels of order previously discussed enables tuning the properties of NC films to precisely fit the needs of a specific application. Semiconductor NCs have found application in a wide range of devices that take advantage of their size dependent electronic properties and tunable absorption and emission spectra. Each application has a specific set of requirements for the structure of the NC film as well as the degree of electronic coupling required. As a general rule of thumb, applications that exploit the strong, tunable absorption of NCs to generate photoelectrons require strong electronic coupling, and applications that depend on radiative recombination in NCs to emit light require weaker electronic coupling.

1.5.1 Photovoltaics

Perhaps the most exciting and commonly studied application for semiconductor NC films is in photovoltaic devices. This is due primarily to two potential advantages that NC solar cells have over conventional Si PV. The first is that the strong absorption in NC films and ability to be solution processed allow NC PV to be thin and potentially processed in a roll to roll manufacturing method. This would enable NC PV to find economic niches that are not feasible for conventional PV to compete in, such as low weight, flexible PV integrated into clothing⁸⁵. In addition to niche applications, the ability to tune the bandgap of NC solar cells makes them a candidate material to serve as the top cell in a tandem cell with Si PV, with a maximum efficiency of up to 45%.

The second advantage NC solar cells have over conventional PV is the potential to surpass the Shockley-Queisser (SQ) limit for a single junction cell. NCs can violate one of the critical assumptions of SQ by generating more than one electron-hole pair per incident photon. In NCs this is commonly referred to as multiple exciton generation (MEG) or carrier multiplication^{86, 87}. The phenomenon is also known as impact ionization in bulk semiconductor materials. In the bulk, it is difficult for impact ionization to occur because both energy and momentum must be conserved during the creation of a new electron-hole pair. In contrast, for NCs the momentum requirement is relaxed due to the localization of the carriers to a single NC. From the uncertainty principle in quantum mechanics, we know that $\Delta x \Delta p \geq \hbar/2$. When electrons are localized to a NC with diameter on the order of nanometers, there is a compensatingly large uncertainty in the momentum, and hence conservation of momentum becomes meaningless. This is illustrated schematically in Figure 1.8.

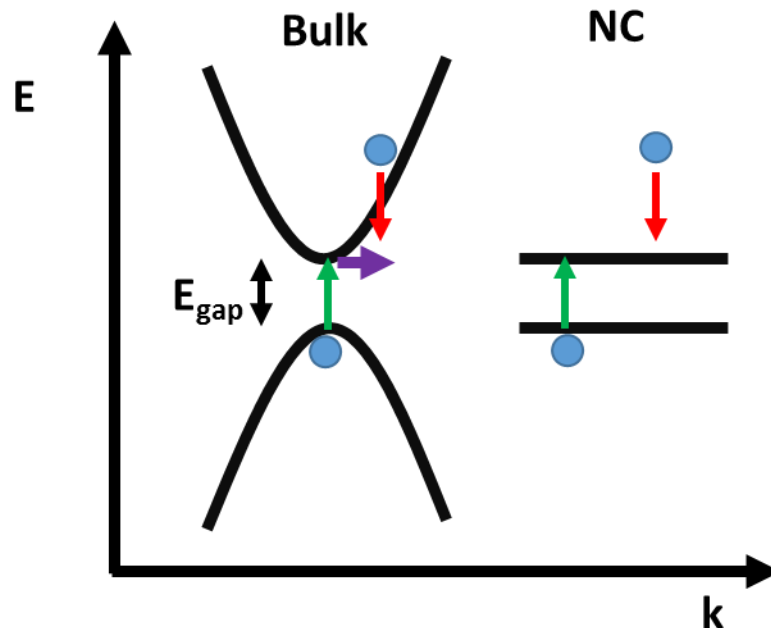


Figure 1.8: Carrier multiplication in bulk materials and nanocrystals. Conservation of momentum requires emission or absorption of a phonon (purple), whereas in NCs this condition is relaxed.

MEG yields up to 75% have been observed in isolated nanocrystals and external quantum efficiencies as high as 120% have been seen in prototype devices^{49, 88}. Integrating carrier multiplication effects into detailed balance calculations predicts an increase in the single bandgap maximum efficiency from 33.7% to 44.4%, which includes a reduction in the optimal bandgap to approximately .7 eV⁸⁹.

The intense research into NC PV has driven record efficiencies up rapidly, from ~3% in 2010 to a current record of 10.6%⁹⁰. Much of the advances in the efficiency of NC PV has been the product of improved understanding of and control over surface trap states created during ligand exchange. PV applications require very strong electronic coupling to assist in exciton dissociation and carrier transport, so ligand exchange, either in solution or after film deposition is an absolutely necessary processing step^{61, 62, 77}. The surface traps created during ligand exchange are critical to device performance and minimization of surface traps can be more important than further increases in carrier transport rates⁹¹. In the so called “mobility invariant regime” faster carrier transport enabled by stronger electronic coupling only serves to get carriers to trap states faster⁹².

By far the most successful chemical treatment to mitigate traps in NC films is incorporation of atomic halide ligands onto the NC surface. These halide ions bind to under-coordinated surface sites and eliminate the corresponding midgap states that can trap carriers. An additional recent film passivation method being explored is the epitaxial fusion of NCs in a film to form “confined-but-connected” NC films. PbX (X=Se, S, Te) NCs have been observed to undergo oriented attachment through their {100} crystal facets as shown in Figure 1.9⁹³⁻⁹⁵. This simultaneously leads to a

significant increase in electronic coupling between NCs, as they are now connected by an inorganic bond, and a decrease in surface trap states, as the surface area of the NC film is reduced. This passivation technique has produced NC films with record charge carrier diffusion lengths⁹⁶. A detailed study of these confined-but-connected NC films and the effect of inorganic bonds on electronic coupling is presented in Chapter 6.

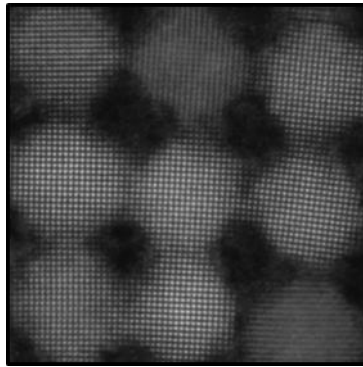


Figure 1.9: Epitaxially connected PbSe nanocrystals. Inorganic bonds decrease the surface area of the NC, reducing the available area for surface traps to form.

1.5.2 Photodetectors

The ability to tune the bandgap of NC films from the UV to IR through control of NC composition at the 1^o level and NC structure at the 2^o level, combined with the potential for low cost, solution processability and integration into novel, flexible device architectures make NC an attractive active material for photodetector applications^{97, 98}. NCs are particularly attractive for detection of IR photons with energy below the 1.1 eV bandgap of Si. NC photodetectors can be separated into two device classifications, diagramed in Figure 1.10 below, photodiodes and photoconductors⁹⁸. In a photodiode, the electrons and holes generated by an absorbed photon are separated and collected at opposite contacts using the same principles behind a pn junction solar cell to drive

charge separation. Photodiodes can have a rapid response time, but are limited to gains ≤ 1 because each generated electron-hole pair can only be collected once. In contrast, in photoconductors one carrier, electrons in Figure 1.10, is trapped in the material and the other carrier drifts from one contact to the next. If the transit time for a carrier in the circuit is less than the recombination time of the mobile carrier with the trapped carrier photoconductors can achieve significant gains, of around 100-1000 in NC films⁹⁸. Recently, a novel device architecture has been developed that involves hole transfer from colloidal NCs to graphene where carrier mobilities are significantly higher⁹⁹. This has enabled gains of up to $\sim 10^8$.

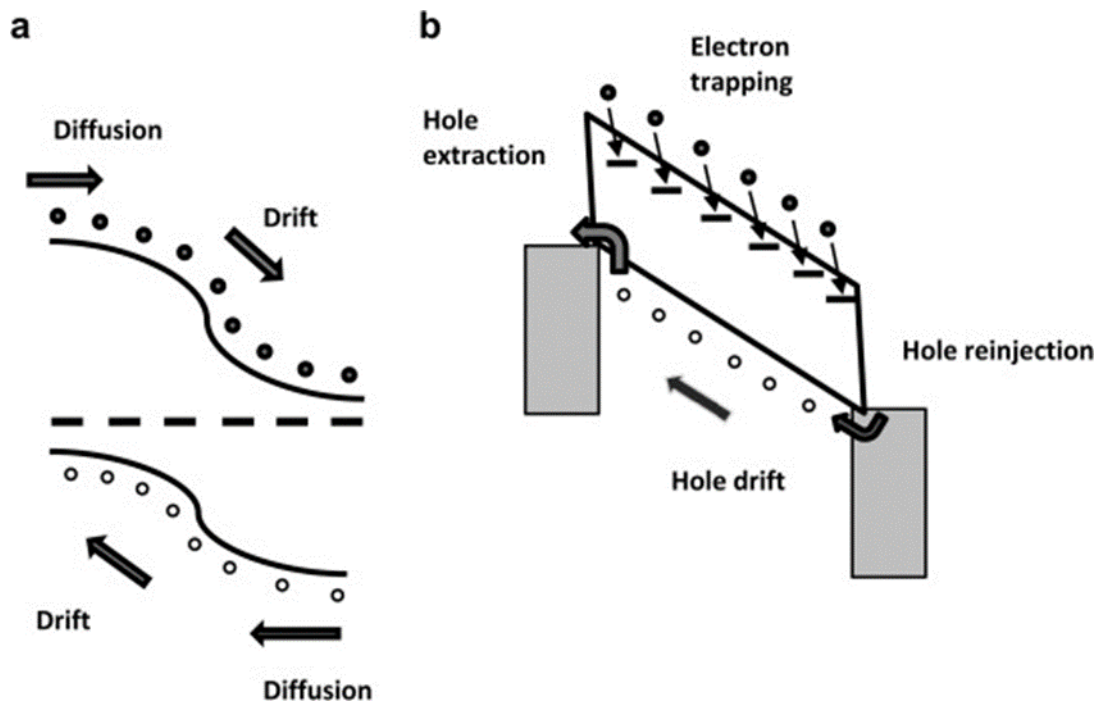


Figure 1.10: Schematic band diagram and carrier flow for an a) photodiode and b) photoconductor. From ⁹⁸ Copyright Elsevier 2011

Both schemes for producing photodetectors using NCs as an active layer require efficient separation of the exciton into separate carriers that can move independently

and fast transport of carriers through the NC film. This requires high electronic coupling between NCs, likely the higher the better for device performance.

1.5.3 Thermoelectrics

Thermoelectric materials seek to harvest energy from waste heat or serve as solid state cooling devices. Materials for thermoelectric applications are judged based on the figure of merit $ZT = S^2 \sigma T / \kappa$, where S is the Seebeck coefficient, σ is the electrical conductivity, κ is the thermal conductivity, and T is the absolute temperature^{100, 101}. It is clear that good thermoelectric materials require good electron transport and poor phonon transport. This is a difficult condition to meet, especially in light of the Wiedemann-Franz law that couples electrical and thermal conductivities. In the field, a significant effort has gone into nanostructured engineering such that grain boundaries and other defects occur on length scales that impede phonon transport but not electrical transport¹⁰¹. This framework for engineering thermoelectric materials is often referred to as the electron crystal-phonon glass paradigm.

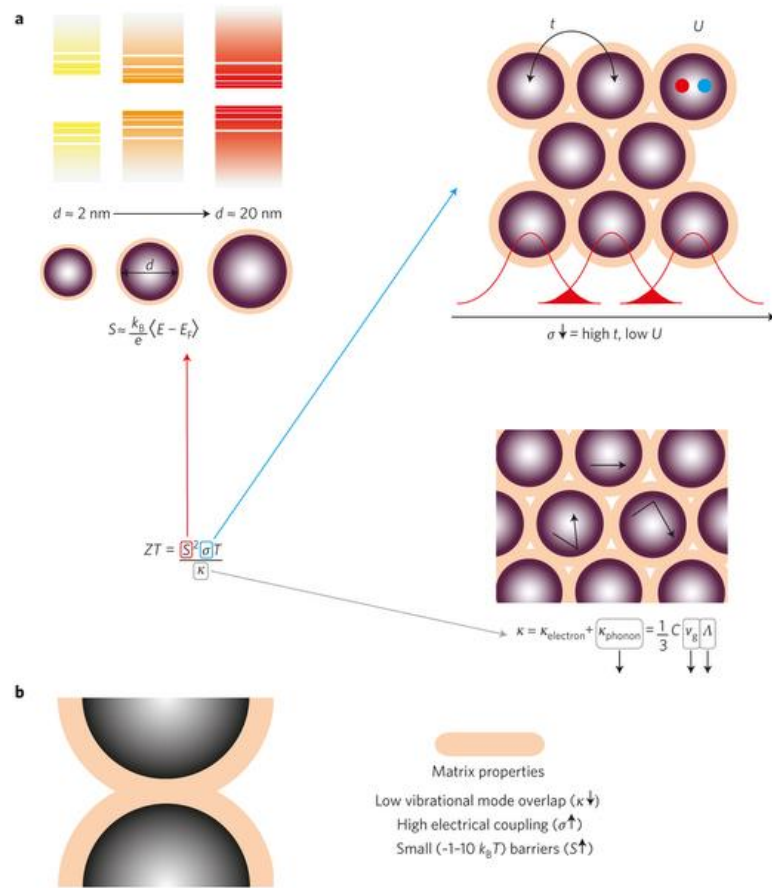


Figure 1.11: a) Control over 2° and 3° structure can enhance each component of ZT. b) The ligand matrix plays a critical role in producing materials with designer properties for thermoelectric applications. From ¹⁰⁰ Copyright 2015 Nature Publishing Group

Due to their nature as a composite material full of interfaces, films of semiconductor NCs are uniquely positioned to provide a revolutionary, rather than evolutionary advance in thermoelectrics. ZT values up to 30 have been predicted for hybrid NC-organic films¹⁰². Thermal transport in NC arrays is mediated by the ligand matrix, which makes up a substantial fraction of the film volume^{103, 104}. Overlap in the vibrational density of states between the NC cores and the organic ligands determines the coupling across the NC-ligand interface for thermal transport. This provides an opportunity for tuning the “artificial atoms” to minimize vibrational density of states overlap and suppress thermal transport. Experimental measurements of the thermal

conductivities of NC films have found thermal conductivities on the order of .1 to 1 W/m·K, approximately 2 orders of magnitude lower than the thermal conductivities in bulk thermoelectrics¹⁰⁰. As the ligands are exchanged from native ligands to shorter ligands to enhance electrical conductance, the thermal conductance has been observed to increase as well¹⁰⁵. There is likely an optimal point at which σ/κ is maximized in a NC assembly. However, it is not obvious that this should occur at the maximal coupling extreme suitable for photodetector and photovoltaic applications. The ability to independently tune the NC properties, assembly structure, and electrical coupling provides the opportunity to explore a large parameter space in order to maximize ZT in these designer materials.

1.5.4 Electroluminescent Light Emitting Diodes

The tunable bandgap of NC films also makes them interesting as the active material in emissive applications such as electroluminescent light emitting diodes⁶. Through precise control over the 1° and 2° structure, NCs with high quantum yield across the whole UV-vis-NIR spectral range can be created. Additionally, the narrow FWHM of emission, typically 50-100 nm, leads to pure color emission that is advantageous for display applications¹⁰⁶.

Although the 4° structure of a PV and LED device are essentially the same, the requirements on the 3° structure are very different. Instead of maximal electronic coupling in order to transport charge to the contacts quickly, the degree of electronic coupling that is optimal for an electroluminescent QD LED is determined by balancing charge transport with efficient radiative recombination of excitons. Too much electronic coupling between QDs can lead to exciton dissociation and reduced emission, while too little electronic coupling can impede charge transport and prevent injected electrons and holes from meeting in the active layer^{22, 23}.

In addition to the different requirements for bonding among the QDs in the active layer, the scale of devices for PV and LED applications and film formation methods are very different. As mentioned above, one of QD PV's advantages is the potential to use roll to roll processing techniques to produce square meters of solar panels quickly and cheaply. In contrast, LEDs, especially in display applications, require precise spatial control. In order to fabricate electroluminescent LEDs with small feature size, more precise fabrication processes, such as ink jet or 3D printing are necessary. Electroluminescent LEDs have already achieved RGB pixel densities that surpass the requirements for a "retina" display and the first all 3D printed QD LED has been demonstrated^{107, 108}. Taken together, these manufacturing successes, combined with the narrow, tunable emission in QD indicate that the future of QD LEDs is bright.

1.5.5 Nanocrystals as Downconverters

The final applications I will discuss all fall under the broad category of using NCs as downconverters. In all cases, NCs are excited by absorbing incident light and then reemit the photons with high quantum yield at the bandgap of the NC. This general scheme for exploiting the size tunable, narrow emission of semiconductor NCs finds applications in solid state lighting as a phosphor, display technologies such as Sony Triluminous and the Amazon Fire tablet, and in energy harvesting as a luminescent solar concentrator^{106, 109, 110}.

In contrast to all of the applications discussed previously, these applications require no electron transport and are most efficient when the NCs are isolated. As a result, the requirements for the 3° structure of NC films are completely different than the previously discussed applications. NCs are often dispersed in a transparent polymeric matrix at low volume concentrations to ensure that NCs remain isolated¹⁰⁹. As downconverting applications put relatively little burden on the 3° structure of the

NC film, considerable effort is put into controlling the 1° and 2° structures of these particles in order to maximize the quantum yield and optimize other relevant aspects of emission, such as the FWHM or Stokes Shift of the photoluminescence^{43, 46}.

1.6 Structure of the Dissertation

Nanocrystals clearly have the potential to make contributions to advances in a wide range of fields and applications. In the following chapters, I will detail the contributions I have made to understanding the processing-structure-property relationships in NC films. The chapters 2-4 will detail my work on thermal processing of NC films. I will show how non-equilibrium laser annealing can produce films with a tunable degree of fusion among NCs. Using a binary nanocrystal superlattice as a periodic nanoreactor, I investigate fusion of a precisely controlled number of NCs in a confined volume. By exploiting spatial gradients in annealing temperature I produce NC films with tunable emission at the 3° level of structure. Chapters 5 and 6 comprise my investigation into post-assembly chemical processing of NC films to improve their properties. I investigate simultaneous cation and ligand exchange in PbSe nanocrystal films that both increases the rate of Förster resonant energy transfer and the photoluminescence of a NC film in a single processing step. In addition, I examine in detail the effect of post assembly growth of long range ordered confined-but-connected nanostructures to control the size of the inorganic bonds between particles. Chapter 7 presents a theoretical work examining semitransparent photovoltaics and explicitly accounts for the value of both energy generation and light transmission in order to produce a quantitative framework for evaluating semitransparent photovoltaics, which was missing in the literature. I will end with a section detailing future directions that build on the work presented in the previous chapters as well as broad conclusions that can be drawn from my dissertation as a whole.

Additionally, each chapter has a corresponding appendix filled with materials and methods, and other supplementary information that was not included in the main text. Each appendix begins with a short section of advice for any future students that wish to replicate or build on my work that details common pitfalls, or areas that deserve special emphasis and attention. Lastly, I have included a catch all appendix containing incomplete and failed experiments that would not otherwise be presented elsewhere. I consider this my scientific blooper reel and I hope that by including it, I may be able to save any future researchers from duplicating my mistakes. If a reader has any questions regarding some aspect of this work that has not be covered in sufficient detail, please do not hesitate to contact me at btrem1@outlook.com.

REFERENCES

1. Rossetti, R.; Hull, R.; Gibson, J. M.; Brus, L. E. *The Journal of Chemical Physics* **1985**, 82, 552.
2. Rossetti, R.; Ellison, J.; Gibson, J.; Brus, L. *The Journal of Chemical Physics* **1984**, 80, 4464-4469.
3. Talapin, D. V.; Lee, J.-S.; Kovalenko, M. V.; Shevchenko, E. V. *Chem. Rev.* **2009**, 110, 389-458.
4. Nozik, A. J.; Beard, M. C.; Luther, J. M.; Law, M.; Ellingson, R. J.; Johnson, J. C. *Chem. Rev.* **2010**, 110, 6873-6890.
5. Lim, J.; Bae, W. K.; Kwak, J.; Lee, S.; Lee, C.; Char, K. *Opt. Mater. Express* **2012**, 2, 594-628.
6. Shirasaki, Y.; Supran, G. J.; Bawendi, M. G.; Bulovic, V. *Nat Photon* **2013**, 7, 13-23.
7. Sargent, E. H. *Adv. Mater.* **2008**, 20, 3958-3964.
8. Talapin, D. *ACS nano* **2008**.
9. Echols, H. G., *Operators and promoters: The story of molecular biology and its creators*. Univ of California Press: 2001.
10. Yu, W. W.; Falkner, J. C.; Shih, B. S.; Colvin, V. L. *Chem. Mater.* **2004**, 16, 3318-3322.
11. Kwon, S. G.; Hyeon, T. *Acc. Chem. Res.* **2008**, 41, 1696-1709.
12. Schmidt, L. C.; Pertegás, A.; González-Carrero, S.; Malinkiewicz, O.; Agouram, S.; Mínguez Espallargas, G.; Bolink, H. J.; Galian, R. E.; Pérez-Prieto, J. J. *Am. Chem. Soc.* **2014**, 136, 850-853.
13. El-Sayed, M. A. *Acc. Chem. Res.* **2004**, 37, 326-333.
14. Reiss, P.; Protière, M.; Li, L. *Small* **2009**, 5, 154-168.
15. Carbone, L.; Nobile, C.; De Giorgi, M.; Sala, F. D.; Morello, G.; Pompa, P.; Hytch, M.; Snoeck, E.; Fiore, A.; Franchini, I. R.; Nadasan, M.; Silvestre, A. F.; Chiodo, L.; Kudera, S.; Cingolani, R.; Krahne, R.; Manna, L. *Nano Lett.* **2007**, 7, 2942-2950.
16. Jiang, S.; Chen, Q.; Tripathy, M.; Luijten, E.; Schweizer, K. S.; Granick, S. *Adv. Mater.* **2010**, 22, 1060-1071.
17. Crabtree, G. W.; Sarrao, J. L. *MRS Bull.* **2012**, 37, 1079-1088.
18. Choi, J. J.; Bian, K.; Baumgardner, W. J.; Smilgies, D.-M.; Hanrath, T. *Nano Lett.* **2012**, 12, 4791-4798.
19. Bian, K.; Choi, J. J.; Kaushik, A.; Clancy, P.; Smilgies, D.-M.; Hanrath, T. *ACS Nano* **2011**, 5, 2815-2823.
20. Choi, J. J.; Bealing, C. R.; Bian, K.; Hughes, K. J.; Zhang, W.; Smilgies, D.-M.; Hennig, R. G.; Engstrom, J. R.; Hanrath, T. *J. Am. Chem. Soc.* **2011**, 133, 3131-3138.
21. Liu, Y.; Gibbs, M.; Puthussery, J.; Gaik, S.; Ihly, R.; Hillhouse, H. W.; Law, M. *Nano Lett.* **2010**, 10, 1960-1969.
22. Choi, J. J.; Luria, J.; Hyun, B.-R.; Bartnik, A. C.; Sun, L.; Lim, Y.-F.; Marohn, J. A.; Wise, F. W.; Hanrath, T. *Nano Lett.* **2010**, 10, 1805-1811.

23. Sun, L.; Choi, J. J.; Stachnik, D.; Bartnik, A. C.; Hyun, B.-R.; Malliaras, G. G.; Hanrath, T.; Wise, F. W. *Nature nanotechnology* **2012**, *7*, 369-373.
24. Park, J.; Joo, J.; Kwon, S. G.; Jang, Y.; Hyeon, T. *Angew. Chem. Int. Ed.* **2007**, *46*, 4630-4660.
25. de Mello Donegá, C.; Liljeroth, P.; Vanmaekelbergh, D. *Small* **2005**, *1*, 1152-1162.
26. Klimov, V. I., *Nanocrystal quantum dots*. CRC Press: 2010.
27. Peng, X.; Wickham, J.; Alivisatos, A. P. *J. Am. Chem. Soc.* **1998**, *120*, 5343-5344.
28. Hassinen, A.; Moreels, I.; Nolf, K.; Smet, P. *Journal of the* **2012**.
29. Anderson, N. C.; Hendricks, M. P.; Choi, J. J.; Owen, J. S. *J. Am. Chem. Soc.* **2013**, *135*, 18536-18548.
30. Frey, N. A.; Peng, S.; Cheng, K.; Sun, S. *Chem. Soc. Rev.* **2009**, *38*, 2532.
31. Kittel, C. *Rev. Mod. Phys.* **1949**, *21*, 541-583.
32. Zhou, Z.-Y.; Tian, N.; Li, J.-T.; Broadwell, I.; Sun, S.-G. *Chem. Soc. Rev.* **2011**, *40*, 4167-4185.
33. Zhou, X.; Xu, W.; Liu, G.; Panda, D.; Chen, P. *J. Am. Chem. Soc.* **2010**, *132*, 138-146.
34. Scholl, J. A.; Koh, A. L.; Dionne, J. A. *Nature* **2012**, *483*, 421-427.
35. Brus, L. E. *The Journal of Chemical Physics* **1984**, *80*, 4403-4409.
36. Nelson, J., *The physics of solar cells*. World Scientific: 2003; Vol. 1.
37. Jasieniak, J.; Califano, M.; Watkins, S. E. *ACS Nano* **2011**, *5*, 5888-5902.
38. Jasieniak, J.; Smith, L.; Embden, J. v.; Mulvaney, P.; Califano, M. *The Journal of Physical Chemistry C* **2009**, *113*, 19468-19474.
39. Woggon, U., *Optical properties of semiconductor quantum dots*. Springer: 1997.
40. Kang, I.; Wise, F. W. *J. Opt. Soc. Am. B* **1997**, *14*, 1632-1646.
41. Wise, F. W. *Acc. Chem. Res.* **2000**, *33*, 773-780.
42. Moreels, I.; Lambert, K.; De Muynck, D.; Vanhaecke, F.; Poelman, D.; Martins, J. C.; Allan, G.; Hens, Z. *Chem. Mater.* **2007**, *19*, 6101-6106.
43. Ghosh, Y.; Mangum, B. D.; Casson, J. L.; Williams, D. J.; Htoon, H.; Hollingsworth, J. A. *J. Am. Chem. Soc.* **2012**, *134*, 9634-9643.
44. Stouwdam, J.; Shan, J.; Veggel, F. *The journal of* **2007**.
45. Neo, M. S.; Venkatram, N.; Li, G. S.; Chin, W. S.; Ji, W. *The Journal of Physical Chemistry C* **2010**, *114*, 18037-18044.
46. Chen, O.; Zhao, J.; Chauhan, V. P.; Cui, J.; Wong, C.; Harris, D. K.; Wei, H.; Han, H.-S.; Fukumura, D.; Jain, R. K.; Bawendi, M. G. *Nat Mater* **2013**, *12*, 445-451.
47. Piryatinski, A.; Ivanov, S. A.; Tretiak, S.; Klimov, V. I. *Nano Lett.* **2007**, *7*, 108-115.
48. Ocier, C. R.; Smilgies, D.-M.; Robinson, R. D.; Hanrath, T. *Chem. Mater.* **2015**, *27*, 2659-2665.
49. Cirloganu, C. M.; Padilha, L. A.; Lin, Q.; Makarov, N. S.; Velizhanin, K. A.; Luo, H.; Robel, I.; Pietryga, J. M.; Klimov, V. I. *Nat Commun* **2014**, *5*.
50. Lazarenkova, O. L.; Balandin, A. A. *J. Appl. Phys.* **2001**, *89*, 5509-5515.
51. Maenosono, S.; Okubo, T.; Yamaguchi, Y. *J. Nanopart. Res.* *5*, 5-15.

52. Dinsmore, A.; Yodh, A.; Pine, D. *Physical Review E* **1995**, 52, 4045.
53. Kaushik, A. P.; Clancy, P. *J. Comput. Chem.* **2013**, 34, 523-532.
54. Dong, A.; Chen, J.; Vora, P.; Kikkawa, J.; Murray, C. *Nature* **2010**.
55. Kang, Y.; Ye, X.; Chen, J.; Qi, L.; Diaz, R. E.; Doan-Nguyen, V.; Xing, G.; Kagan, C. R.; Li, J.; Gorte, R. J.; Stach, E. A.; Murray, C. B. *J. Am. Chem. Soc.* **2013**, 135, 1499-1505.
56. Urban, J. J.; Talapin, D. V.; Shevchenko, E. V.; Kagan, C. R.; Murray, C. B. *Nature Materials* **2007**, 6, 115-121.
57. Li, R.; Bian, K.; Wang, Y.; Xu, H.; Hollingsworth, J. A.; Hanrath, T.; Fang, J.; Wang, Z. *Nano Lett.* **2015**, 15, 6254-6260.
58. Li, R.; Bian, K.; Hanrath, T.; Bassett, W. A.; Wang, Z. *J. Am. Chem. Soc.* **2014**, 136, 12047-12055.
59. Weidman, M. C.; Smilgies, D.-M.; Tisdale, W. A. *Nature Materials* **2016**.
60. Hanrath, T.; Choi, J. J.; Smilgies, D.-M. *ACS Nano* **2009**, 3, 2975-2988.
61. Fischer, A.; Rollny, L.; Pan, J.; Carey, G. H.; Thon, S. M.; Hoogland, S.; Voznyy, O.; Zhitomirsky, D.; Kim, J. Y.; Bakr, O. M.; Sargent, E. H. *Adv. Mater.* **2013**,
62. Ning, Z.; Ren, Y.; Hoogland, S.; Voznyy, O.; Levina, L.; Stadler, P.; Lan, X.; Zhitomirsky, D.; Sargent, E. H. *Adv. Mater.* **2012**, 24, 6295-6299.
63. Zhang, J.; Gao, J.; Church, C. P.; Miller, E. M.; Luther, J. M.; Klimov, V. I.; Beard, M. C. *Nano Lett.* **2014**, 14, 6010-6015.
64. Dong, A.; Ye, X.; Chen, J.; Murray, C. *Nano Lett.* **2011**.
65. Dong, A.; Jiao, Y.; Milliron, D. J. *ACS Nano* **2013**, 7, 10978-10984.
66. Whitham, K.; Yang, J.; Savitzky, B. H.; Kourkoutis, L. F.; Wise, F.; Hanrath, T. *Nature materials* **2016**.
67. Li, W.; Fan, H.; Li, J. *Nano Lett.* **2014**.
68. Farva, U.; Park, C. *Sol. Energy Mater. Sol. Cells* **2010**, 94, 303-309.
69. Baik, S. J.; Kim, K.; Lim, K. S.; Jung, S.; Park, Y. C.; Han, D. G.; Lim, S.; Yoo, S.; Jeong, S. *Journal of Physical Chemistry C* **2011**, 115, 607-612.
70. Green, M. L. H. *J. Organomet. Chem.* **1995**, 500, 127-148.
71. Luther, J. M.; Law, M.; Song, Q.; Perkins, C. L.; Beard, M. C.; Nozik, A. J. *ACS Nano* **2008**, 2, 271-280.
72. Weidman, M. C.; Yager, K. G.; Tisdale, W. A. *Chem. Mater.* **2014**, 27, 474-482.
73. Scheele, M.; Hanifi, D.; Zherebetsky, D.; Chourou, S. T.; Axnanda, S.; Rancatore, B. J.; Thorkelsson, K.; Xu, T.; Liu, Z.; Wang, L.-W. *ACS nano* **2014**, 8, 2532-2540.
74. Katsiev, K.; Ip, A. H.; Fischer, A.; Tanabe, I.; Zhang, X.; Kirmani, A. R.; Voznyy, O.; Rollny, L. R.; Chou, K. W.; Thon, S. M.; Carey, G. H.; Cui, X.; Amassian, A.; Dowben, P.; Sargent, E. H.; Bakr, O. M. *Adv. Mater.* **2014**, 26, 937-942.
75. Thon, S. M.; Ip, A. H.; Voznyy, O.; Levina, L.; Kemp, K. W.; Carey, G. H.; Masala, S.; Sargent, E. H. **2013**.
76. Kim, D.; Kim, D.-H.; Lee, J.-H.; Grossman, J. C. *Phys. Rev. Lett.* **2013**, 110, 196802.

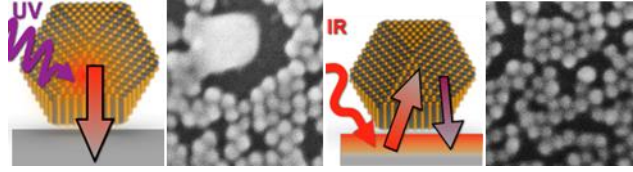
77. Tang, J.; Kemp, K. W.; Hoogland, S.; Jeong, K. S.; Liu, H.; Levina, L.; Furukawa, M.; Wang, X.; Debnath, R.; Cha, D.; Chou, K. W.; Fischer, A.; Amassian, A.; Asbury, J. B.; Sargent, E. H. *Nat Mater* **2011**, 10, 765-771.
78. Chen, Y.; Palmer, R. E.; Wilcoxon, J. P. *Langmuir* **2006**, 22, 2851-2855.
79. Ingham, B.; Lim, T. H.; Dotzler, C. J.; Henning, A.; Toney, M. F.; Tilley, R. D. *Chem. Mater.* **2011**, 23, 3312-3317.
80. van Huis, M. A.; Kunneman, L. T.; Overgaag, K.; Xu, Q.; Pandraud, G.; Zandbergen, H. W.; Vanmaekelbergh, D. I. *Nano Lett.* **2008**, 8, 3959-3963.
81. Goodfellow, B. W.; Rasch, M. R.; Hessel, C. M.; Patel, R. N.; Smilgies, D.-M.; Korgel, B. A. *Nano Lett.* **2013**, 13, 5710-5714.
82. Goodfellow, B. W.; Patel, R. N.; Panthani, M. G.; Smilgies, D.; Korgel, B. A. *The Journal of Physical Chemistry C* **2011**, 115, 6397-6404.
83. Baumgardner, W. J.; Yu, Y.; Hovden, R.; Honrao, S.; Hennig, R. G.; Abruña, H. D.; Muller, D.; Hanrath, T. *ACS nano* **2014**, 8, 5315-5322.
84. Law, M.; Luther, J.; Song, Q.; Hughes, B. *Journal of the* **2008**.
85. Schubert, M. B.; Werner, J. H. *Mater. Today* **2006**, 9, 42-50.
86. Nozik, A. *Physica E: Low-dimensional Systems and Nanostructures* **2002**, 14, 115-120.
87. Shabaev, A.; Efros, A. L.; Nozik, A. J. *Nano Lett.* **2006**, 6, 2856-2863.
88. Davis, N. J. L. K.; Bohm, M. L.; Tabachnyk, M.; Wisnivesky-Rocca-Rivarola, F.; Jellicoe, T. C.; Ducati, C.; Ehrler, B.; Greenham, N. C. *Nat Commun* **2015**, 6.
89. Hanna, M.; Nozik, A. J. *Appl. Phys.* **2006**, 100, 074510.
90. Kim, G.-H.; García de Arquer, F. P.; Yoon, Y. J.; Lan, X.; Liu, M.; Voznyy, O.; Yang, Z.; Fan, F.; Ip, A. H.; Kanjanaboos, P.; Hoogland, S.; Kim, J. Y.; Sargent, E. H. *Nano Lett.* **2015**, 15, 7691-7696.
91. Guglietta, G. W.; Diroll, B. T.; Gauding, E. A.; Fordham, J. L.; Li, S.; Murray, C. B.; Baxter, J. B. *ACS nano* **2015**, 9, 1820-1828.
92. Zhitomirsky, D.; Voznyy, O.; Levina, L.; Hoogland, S.; Kemp, K. W.; Ip, A. H.; Thon, S. M.; Sargent, E. H. *Nat Commun* **2014**, 5.
93. Baumgardner, W. J.; Whitham, K.; Hanrath, T. *Nano Lett.* **2013**, 13, 3225-3231.
94. Hughes, B. K.; Blackburn, J. L.; Kroupa, D.; Shabaev, A.; Erwin, S. C.; Efros, A. L.; Nozik, A. J.; Luther, J. M.; Beard, M. C. *J. Am. Chem. Soc.* **2014**, 136, 4670-4679.
95. Sandeep, C. S.; Azpiroz, J. M.; Evers, W. H.; Boehme, S. C.; Moreels, I.; Kinge, S.; Siebbeles, L. D.; Infante, I.; Houtepen, A. J. *ACS nano* **2014**, 8, 11499-11511.
96. Carey, G. H.; Levina, L.; Comin, R.; Voznyy, O.; Sargent, E. H. *Adv. Mater.* **2015**.
97. Sun, Z.; Liu, Z.; Li, J.; Tai, G. a.; Lau, S. P.; Yan, F. *Adv. Mater.* **2012**, 24, 5878-5883.
98. Konstantatos, G.; Sargent, E. H. *Infrared Physics & Technology* **2011**, 54, 278-282.
99. Konstantatos, G.; Badioli, M.; Gaudreau, L.; Osmond, J.; Bernechea, M.; de Arquer, F. P. G.; Gatti, F.; Koppens, F. H. L. *Nat Nano* **2012**, 7, 363-368.

100. Urban, J. J. *Nat Nano* **2015**, 10, 997-1001.
101. Vineis, C. J.; Beverly, M.; Shakouri, A.; Cruz, S. C.; Majumdar, A.; California, U. o.; DC, W.; Kanatzidis, M. G.; University, N. *Adv. Mater.* **2010**, 22, 3970-3980.
102. Müller, K.-H. *The Journal of chemical physics* **2008**, 129, 044708.
103. Ong, W.-L.; Majumdar, S.; Malen, J. A.; McGaughey, A. J. H. *The Journal of Physical Chemistry C* **2014**, 118, 7288-7295.
104. Ong, W.; Rupich, S. M.; Talapin, D. V.; McGaughey, A. J.; Malen, J. A. *Nature Materials* **2013**, 12, 410-415.
105. Liu, M.; Ma, Y.; Wang, R. Y. *ACS nano* **2015**, 9, 12079-12087.
106. Bourzac, K. *Nature* **2013**, 493, 283.
107. Kim, B. H.; Onses, M. S.; Lim, J. B.; Nam, S.; Oh, N.; Kim, H.; Yu, K. J.; Lee, J. W.; Kim, J.-H.; Kang, S.-K. *Nano Lett.* **2015**, 15, 969-973.
108. Kong, Y. L.; Tamargo, I. A.; Kim, H.; Johnson, B. N.; Gupta, M. K.; Koh, T.-W.; Chin, H.-A.; Steingart, D. A.; Rand, B. P.; McAlpine, M. C. *Nano Lett.* **2014**, 14, 7017-7023.
109. Meinardi, F.; Colombo, A.; Velizhanin, K. A.; Simonutti, R.; Lorenzon, M.; Beverina, L.; Viswanatha, R.; Klimov, V. I.; Brovelli, S. *Nature Photonics* **2014**, 8, 392-399.
110. Bronstein, N. D.; Li, L.; Xu, L.; Yao, Y.; Ferry, V. E.; Alivisatos, A. P.; Nuzzo, R. G. *ACS nano* **2013**, 8, 44-53.

CHAPTER 2
**PROCESSING-STRUCTURE-PROPERTY RELATIONSHIPS IN LASER
ANNEALED PbSe NANOCRYSTAL THIN FILMS¹**

As nanocrystal (NC) synthesis techniques and device architectures advance, it becomes increasingly apparent that new ways of connecting NCs with each other and their external environment are required to realize their considerable potential. Enhancing inter-NC coupling by thermal annealing has been a long-standing challenge. Conventional thermal annealing approaches are limited by the challenge of annealing the NC at sufficiently high temperatures to remove surface bound ligands while at the same time limiting the thermal budget to prevent large scale aggregation. Here we investigate non-equilibrium laser annealing of NC thin films that enables separation of the kinetic and thermodynamic aspects of nanocrystal fusion. We show that laser annealing of NC assemblies on nano- to microsecond timescales can transform initially isolated NCs in a thin film into an interconnected structure in which proximate dots ‘just touch’. We investigate both Pulsed Laser Annealing and Laser Spike Annealing and show that both annealing methods can produce “confined-but-connected” nanocrystal films. We develop a thermal transport model to rationalize the differences in resulting film morphologies. Finally, we show that the insights gained from study of nanocrystal mono- and bilayers can be extended to three dimensional NC films. The basic processing-structure-property relationships established in this work provide guidance to future advances in creating functional thin films in which constituent NCs can purposefully interact.

¹ The results presented in this chapter have been published in Ref 1. Treml, B. E.; Robbins, A. B.; Whitham, K.; Smilgies, D.-M.; Thompson, M. O.; Hanrath, T. *ACS nano* **2015**, 9, 4096-4102.



2.1 Introduction

Advances in the fabrication of materials with nanoscale control over size, shape, and composition have created a fertile opportunity space for novel materials that continues to intrigue scientists and engineers. Semiconductor nanocrystals (NCs), also referred to as quantum dots, in particular provide versatile building blocks for emerging nanotechnologies by virtue of their size tunable optoelectronic properties and low-cost, solution-based processing.²⁻⁴ To translate this much acclaimed potential to technological fruition, several materials processing and fabrication challenges remain to be resolved; in particular efficiently coupling proximate dots to each other while at the same time preserving the unique quantum-confinement properties of isolated dots persists as a critical challenge. Here we show that the seemingly contradictory requirements can be resolved by rapid non-equilibrium processing techniques.

Previous strategies to improve connections between NCs in thin films can be broadly categorized as chemical and physical approaches. Chemical treatments aim to displace or exchange the native long chain ligand with a shorter ligand. Although these treatments successfully reduce interparticle spacing, chemical treatments generally disrupt long-range ordering of NCs in the film and require layer-by-layer deposition methods.⁵⁻⁷ Recently, precise control over the chemical treatment of specific NC facets has enabled impressive advances in the formation of superstructures with epitaxial connections among proximate NCs⁸⁻¹⁰. An important concern in chemical treatments is that they introduce significant risks to alter the physical and chemical nature of the NC

surface which, in most cases, has detrimental impacts on the electronic properties. In the specific context of optoelectronic applications of NC, ligand exchange and displacement have been shown to lead to the formation of undesirable surface states that trap mobile charges¹¹.

Physical approaches (*e.g.*, thermal annealing or high-pressure treatment) to connect NCs have been less thoroughly explored and present their own challenges. High pressure processing has been shown to cause oriented fusion of NCs into nanosheets^{12, 13}, but this approach has not yet been applied to NC thin films in devices. Thermal annealing of NC films provides an ostensibly simple route to reduce interparticle spacing and enhance interdot coupling. However, thermal treatments involve a delicate balance of removing the stabilizing ligands from the NC surface without causing neighboring particles to aggregate. Unfortunately, the relatively high temperatures required to remove surface bound ligands generally lead to substantial particle aggregation during conventional thermal annealing.¹⁴ *In-situ* TEM studies of NCs with a destabilized ligand shell at elevated temperatures have been observed to rotate and fuse together over time scales as large as minutes *via* surface diffusion.¹⁵

The degree to which annealed NCs sinter can be described by a diffusion length, $l_d = \sqrt{D\tau}$. The diffusion coefficient, D , and time, τ , can be tailored by adjusting the temperature and duration of the thermal anneal, respectively. Structural changes of NC film during thermal annealing can then be qualitatively categorized into three regimes delineated by the ratio of the diffusion length to the nearest neighbor separation between NCs, or l_d/d_{NC} . For $l_d/d_{NC} < 1$, individual NCs effectively stay in their initial position and remain isolated from neighboring particles. On the other hand, for large diffusion

lengths, *i.e.*, $l_d/d_{NC} > 1$, particles aggregate into microscopic structures that lack the desired size-tuned properties. At intermediate diffusion lengths, *i.e.*, $l_d/d_{NC} \sim 1$, annealed NCs diffuse and restructure into assemblies in which proximate particles ‘just touch’.

The ‘confined-but-connected’ superstructures, illustrated schematically in Figure 2.1a, provide the desired balance of quantum-confinement (*e.g.*, to tailor light absorption or emission) and interdot coupling (to efficiently transport charges out of and into the NCs). Achieving this delicate processing balance with conventional thermal annealing approaches is complicated since the large temperatures required to remove ligands (200-300°C) and long annealing times (1-60 min) lead to significant sintering.¹⁶

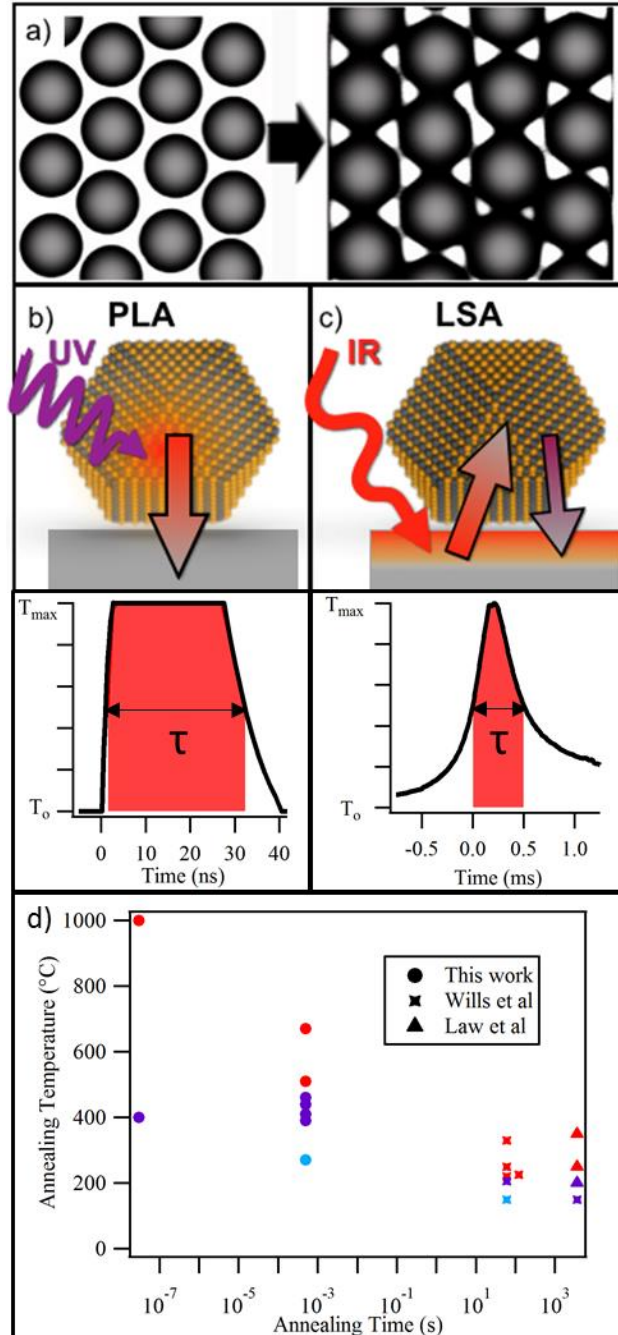


Figure 2.1: a) Formation of ‘confined-but-connected’ nanostructures via controlled fusion. b,c) Cartoons of the method of heating for the excimer (b) and CO_2 (c) lasers used in this work. Below, schematic time-temperature profiles for the lasers. Red shading indicates the time during which films are at or above half of the peak temperature. d) Time-Temperature-Transformation diagram for annealing of PbSe quantum dots in this and previous works. Red, Purple, and Blue markers indicate large, intermediate, and small values of l_d respectively.

Restricting the thermal annealing to nano- to microsecond duration provides access to the desired intermediate fusion regime by limiting the extent of particle diffusion. Photonic curing treatment of semiconductor NC films involving pulsed light (160 μ s) from a xenon flash lamp were recently demonstrated by Stolle *et al.*¹⁸ The laser annealing approaches explored in this work are illustrated in Figure 2.1b,c. Pulsed laser annealing (PLA) and laser spike annealing (LSA) provide access to different annealing times (ns and μ s) and heating strategies (*i.e.* direct and indirect excitation of the NCs). PLA employs an excimer laser ($\lambda=308$ nm) to deliver a single 30 ns pulse to the entire sample (Figure 2.1b). The excimer laser pulse is directly absorbed by NCs resulting in rapid heating followed by rapid thermal quench to the substrate.^{19, 20} In LSA, on the other hand, a continuous wave CO₂ laser ($\lambda=10.6$ μ m) is scanned across the sample. The infrared laser is absorbed by a highly doped silicon substrate, which conducts heat into the NC film (Figure 2.1c). Scanning the laser beam across the sample leads to rapid heating as the laser approaches, followed by rapid cooling into the substrate after the laser passes {Iyengar, 2012 #162}. The duration of the heating can be controlled by the laser scan speed. In the experiments detailed below we focused on a dwell of 500 μ s, as defined by the full-width at half maximum of the laser beam divided by the scan velocity.

Figure 2.1d compares the characteristic annealing time and temperatures explored in this work to earlier literature reports.^{16, 17} This plot illustrates that fast thermal processing enabled by laser annealing provides access to substantially higher annealing temperatures than conventional methods. In combination, PLA and LSA

present complementary processing techniques to systematically explore a significant region of thermal annealing parameter space.

We focus on PbSe NCs as a model system for the formation of confined-but-connected structures since PbSe NC provide highly tunable building blocks with well-defined and pronounced quantum confinement effects. Colloidal NCs with precisely controlled size and shape are readily available thanks to robust synthesis methods.²¹ The electronic and optical properties of nanostructured PbSe are governed by strong quantum confinement effects.²² Due to the large Bohr exciton radius of PbSe (23 nm), the optoelectronic properties are highly sensitive to changes in particle size, which provides a clear and strong indicator for change in quantum confinement. The non-equilibrium laser annealing of PbSe NCs described in this work shows that novel ‘confined-but-connected’ structures be created and the degree of connection can be tuned *via* precise control over the annealing parameters.

2.2 Structural Characterization of Laser Annealed Films

We analyzed the morphology of PbSe NC films with scanning electron microscopy (SEM) before and after laser annealing. For both PLA and LSA laser annealing methods, the NC film morphology can be varied from completely separated NCs to completely sintered structures by controlling the laser power, and hence annealing temperature. Figure 2.2 summarizes the evolution of the morphology of the NC film for a range of annealing conditions. Figure 2.2a presents the initial film of isolated NCs in a film with sub-monolayer coverage. We have identified the processing conditions for both PLA (Figure 2.2b) and LSA (Figure 2.2c) treated films that that

correspond to the three processing regimes discussed above. The left image reflects an annealed film with low diffusion length ($l_d/d_{NC} < 1$). The rightmost image in the sequence illustrates completely fused structures formed under conditions of large diffusion lengths ($l_d/d_{NC} \gg 1$). At intermediate conditions, corresponding to a laser fluence of 90 mJ cm⁻² for PLA and LSA peak temperature near 440°C we observed confined-but-connected structures in which proximate particles ‘just touch’ but maintain their individual particle character. This processing window of opportunity, defined by $l_d/d_{NC} \sim 1$ provides control over the level of connectivity between NCs and to create structures not accessible by conventional processing methods.

Chemical methods for producing physically connected NCs obtain ordered, epitaxially connected structures *via* facet specific ligand removal that produces anisotropic interactions to guide rotation and assembly.^{10, 23} In contrast, laser annealed NC films show reduced order after annealing, indicating that thermal removal of ligands is isotropic or the short annealing times inhibit rotations, as a result connections between nanocrystals may consist of grain boundaries or amorphous PbSe.

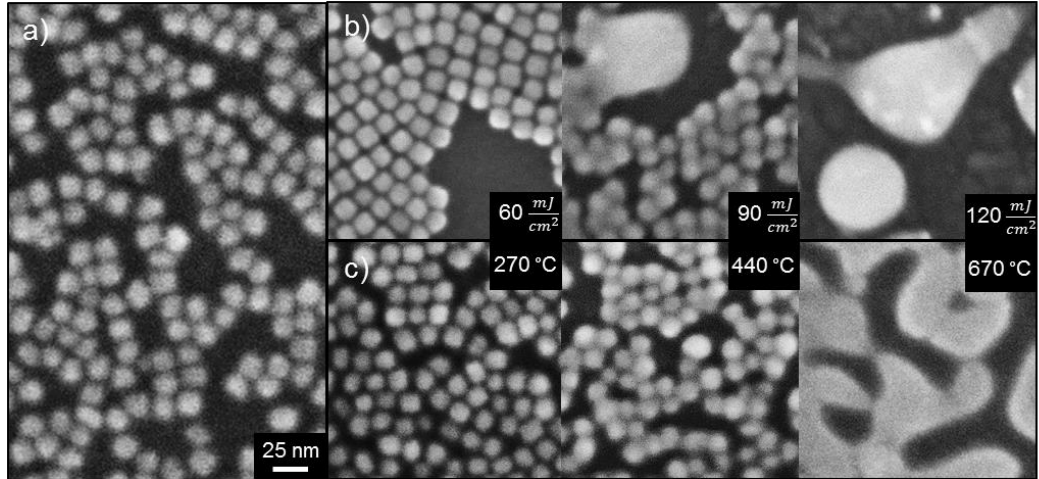


Figure 2.2: Scanning Electron Micrographs of a) an unannealed film b,c) PLA and LSA films respectively. Annealing temperature cannot be determined for PLA films. All micrographs are at the same scale.

Although both PLA and LSA show a transition region defined by $l_d \sim d_{NC}$, we found that the structures formed by direct PLA were less uniform than NC films annealed indirectly by the LSA method. SEM image analysis of PLA treated NC films revealed regions that appear to have melted and completely fused are nanometers away from sections of film that are hardly affected by the annealing at all. The variable degree of connection between proximate dots in PLA treated NC films is undesirable since the structural heterogeneity translates directly into a broad distribution of optical and electrical properties of the NC film.^{24, 25}

2.3 Thermal Transport in LSA and PLA Films

To understand why PLA treated NC films were less uniform than those treated by LSA, we compared the fundamental heat flows involved in both processes. In the case of LSA, the NCs are not directly photoexcited by the CO₂ laser as the dots are transparent at long wavelengths. Instead, the CO₂ laser is absorbed by the underlying

highly doped Si substrate, which then indirectly heats the NC film at the surface. Heat transfer into and out of the NC is therefore by conduction. Following the procedure detailed in recent work by Ong *et al*, we estimate the thermal conductivity of our NC films to be $0.3 \text{ W m}^{-1}\text{K}^{-1}$, which leads to a thermal diffusion length of 800 nm in $1 \mu\text{s}$.²⁶ We can therefore conclude that NC in monolayer and partial bilayer films are exposed to essentially the same time-temperature profile, leading to a uniform NC film after annealing.

In contrast, the excimer laser employed in PLA is directly absorbed in the NC film. The temperature of the NC therefore depends on the balance of heat generated by thermalization of the direct photoexcitation and heat transferred to the underlying substrate. The effects of direct photoexcitation and limited heat transfer out of the dot are particularly pronounced in partial NC bilayer films. SEM images of partial NC bilayer films annealed with the excimer laser (Figure 2.3a) reveal that NC in the top layer are completely fused whereas the character of individual NCs in the bottom layer is preserved. The dramatically different morphologies formed in the top and bottom layer are a manifestation of the limiting heat transfer out of photoexcited dots. Thicker regions of the film absorb more light and conduct heat away more slowly, which leads to higher temperatures and larger diffusion lengths, l_d .

To better understand the interplay of light absorption and heat transport we developed an analytical model for the steady state of the system that balances absorbed energy with heat transport into the substrate *via* conduction. Since the thermal conductivity of the Si substrate is approximately 3 orders of magnitude higher than NC films, we can consider the substrate as a room temperature heat sink. The temperature

differential between the NC and the substrate can then be described by $\Delta T = I * \rho_{th}$, where I is the absorbed power per unit area and ρ_{th} is the thermal resistance of the NC film. We provide values of the NC absorption coefficients, used to determine the absorbed energy, and thermal conductivities of NC core and ligand, as well as an example calculation in Appendix A.

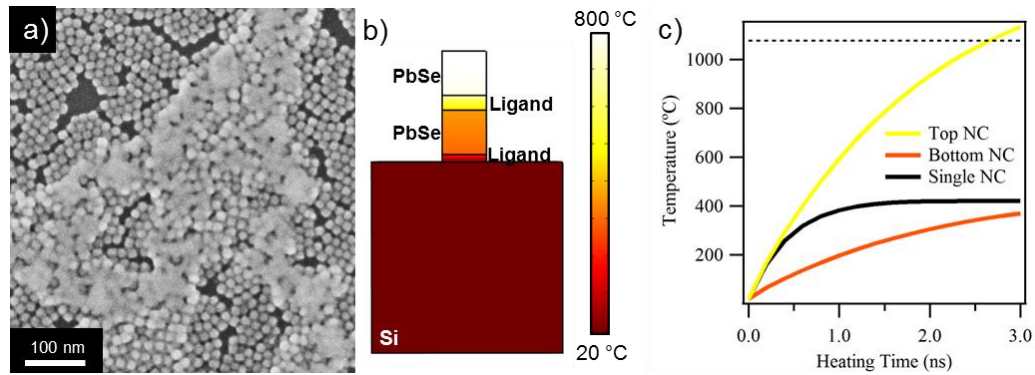


Figure 2.3. Heat transport under direct absorption of light a) A partial bilayer of NCs showing significant sintering in the top layer and limited sintering in a nearby monolayer. b) Simulated temperature profiles for a bilayer of 12 nm PbSe cubes after 1.6 ns of annealing c) Evolution of NCs temperature over 3 ns of heating. The dotted line indicates the melting point of PbSe.

In the case of an NC monolayer, the model predicts a steady state temperature difference of 420 °C at 90 mJ cm⁻² fluence. In the bilayer case, 50% more energy is absorbed and heat transport must occur across additional thermally resistive NC-ligand interfaces. As a result, the model predicts a temperature differential of 1580 °C, significantly above the melting temperature of PbSe (1083 °C). The basic heat transfer model therefore successfully explains the pronounced differences in pulsed laser annealing of monolayer and bilayer NC films.

Beyond the basic temperature differential, we also sought to understand the transient behavior of the temperature profiles resulting from the short ($\tau \sim 30$ -50 ns)

annealing time characteristic for PLA. To simulate the temporal evolution of the temperature in the NC film, we modeled NC monolayer and bilayer films in COMSOL (details of the model are provided in Appendix A). Figure 2.3c compares the simulated temperature transients for monolayer and bilayer NC films during the first 3 ns of heating with a 90 mJ cm^{-2} excimer laser pulse. We can see that the monolayer film reaches the predicted steady state temperature very quickly. In the case of a bilayer, the top NC rises past the melting point of PbSe after only 3 ns of heating.

The significantly higher temperature of the NC in the top layer is consistent with the NC coalescence revealed in our experiments. Figure 2.3b shows a snapshot of the model 1.6 ns after the heating pulse. The PbSe NC cores are nearly isothermal while temperature drops occur in the ligands that separate the NCs. This temperature gradient is consistent with the MD simulations of a 1D chain of NCs by Ong *et al.*²⁶ Our model indicates that due to increased absorption of energy as well as decreased thermal transport away from heated NCs, the precise thickness of a NC film has a large impact on the temperatures experienced due to direct heating. The large variation in temperature exacerbates inhomogeneities in the NC film, leading to a nonuniform film after processing. Collectively, experiments and simulation shown in Figure 2.3 underscore that the morphology of the PLA treated NC depends critically on the thickness (*i.e.* monolayer *vs.* bilayer) coverage of the NC film.

2.4 Property Control via Structure Control

Building on the basic processing-structure relationships established for the mono- and bilayer NC films discussed above, we sought to understand how laser

annealing transforms the structure of thicker multilayered NC films. In particular, we were interested to study how the structure of an ordered 3D NC superlattice may be transformed during laser annealing. Whereas SEM analysis can provide valuable information about the morphological changes of mono- and bilayer NC films, electron microscopy is generally inadequate to gain detailed insights into the three-dimensional structure of the superlattice. To resolve this challenge, we turned to grazing incidence small angle X-ray scattering (GISAXS) to probe three dimensional structural changes in multilayer NC superlattices during laser annealing. The large thermal diffusion length for NC films treated with LSA ensures that thicker (~50 nm) films follow the same time-temperature profiles as the monolayers studied earlier. GISAXS patterns in Figure 2.4 reveal that NC films are initially ordered in a FCC superlattice structure with (111) superlattice plane parallel to the substrate. Annealing at 440 °C leads to disorder in the film, as evidenced by the loss of diffraction peaks and increased intensity in a ring indicating a loss of orientational order. We attribute the partial loss of film order to the limited fusion among particles as observed in the SEM studies. Annealing at higher temperatures leads to a complete destruction of NC superlattice order and only the NC form factor is apparent in GISAXS.

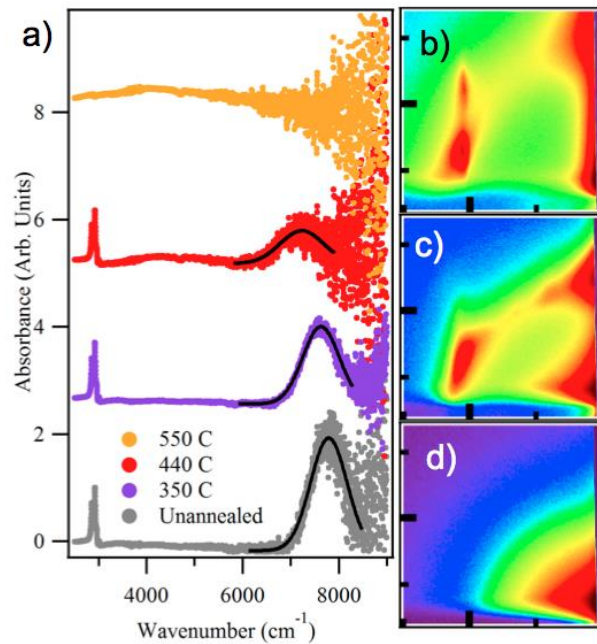


Figure 2.4. Laser annealing of 3D NC superlattices a) FTIR absorption of NC superlattices after annealing. The black line represents a Gaussian fit to the excitonic peak. b,c,d) GISAXS patterns of samples unannealed, annealed at 440°C and 550°C respectively. Bold ticks indicate 1 nm^{-1}

To gain insight into changes of the electronic structure and degree of quantum confinement in the nanostructured films detailed above we analyzed the excitonic peak in the optical spectrum of PbSe nanostructures. By virtue of the large Bohr exciton radius, the optical properties of PbSe NCs are highly sensitive to particle size; therefore, analysis of the evolution of excitonic peak position and width allows us to probe whether quantum-confined electronic structure is preserved, or whether large scale sintering leads to a film with bulk-like optical properties.

Figure 2.4a illustrates the evolution of the excitonic peak of the initial PbSe NC film compared to LSA treated NC films for a range of temperatures. The optical spectra show that the excitonic peak preserved up to annealing temperatures of 440°C, but lost

at higher annealing temperatures corresponding to aggregated PbSe nanostructures formed under conditions for which $l_d/d_{NN} > 1$. FTIR spectra in Figure 2.4a also provide insight into the fate of oleic acid ligands bound to the surface of PbSe NC ligands. NC films annealed up to temperatures of 440°C show characteristic CH stretches near 3000 cm^{-1} whereas the absence of these vibrational signatures at higher temperatures (550°C) suggest complete ligand removal. Interestingly, NC films annealed at 440°C, in the middle of the window of opportunity, reveal an excitonic peak that is red shifted by 60 meV and broadened, which suggests that this film is less confined than the unannealed film.^{27, 28} The decrease in confinement is likely due to a combination of an increase in electronic coupling among neighboring particles due to physical connections among particles and an increased effective permittivity, both of which decrease the energy of creating an exciton. Electrical measurements of NC films deposited in the channel of a pre-fabricated electrode structure show a 300 fold increase in electrical conductivity in response to a 400°C CO₂ laser annealing treatment (See Figure A.2). Taken together, our structural, optical, and electrical characterization of laser annealed NC films indicates that laser processing can be used to create quantum dot films with tunable morphologies and properties not obtainable *via* conventional processing methods.

2.5 Conclusions

We investigated pulsed laser annealing and laser spike annealing as non-equilibrium processing methods to create confined-but-connected NCs films. Both annealing methods provide a window of opportunity that enables the fabrication of structures with limited physical contact among particles. The comparison of direct (PLA) and indirect (LSA) annealing methods revealed that the latter yields more

homogeneous films. We present experimental results and corresponding analytical models to explain the structure transformations in context of the NC film morphology and heat transfer modes. We showed that insights into processing-structure relationships from the study of mono- and bi-layer NC films also guides the laser annealing of thicker three-dimensional NC superlattices. We presented optical spectroscopy of the laser annealed films to illustrate structure dependent changes in the extent of quantum confinement of laser annealed NC films. The basic structure-processing-property relationships established in this work provide valuable guidance to future advances in creating functional thin films in which constituent NCs can purposefully interact *via* non-equilibrium processing.

REFERENCES

1. Treml, B. E.; Robbins, A. B.; Whitham, K.; Smilgies, D.-M.; Thompson, M. O.; Hanrath, T. *ACS nano* **2015**, 9, 4096-4102.
2. Pietryga, J. M.; Schaller, R. D.; Werder, D.; Stewart, M. H.; Klimov, V. I.; Hollingsworth, J. A. *J. Am. Chem. Soc.* **2004**, 126, 11752-11753.
3. Nozik, A. J.; Beard, M. C.; Luther, J. M.; Law, M.; Ellingson, R. J.; Johnson, J. C. *Chem. Rev.* **2010**, 110, 6873-6890.
4. Vineis, C. J.; Beverly, M.; Shakouri, A.; Cruz, S. C.; Majumdar, A.; California, U. o.; DC, W.; Kanatzidis, M. G.; University, N. *Adv. Mater.* **2010**, 22, 3970-3980.
5. Talapin, D. V.; Murray, C. B. *Science* **2005**, 310, 86-89.
6. Liu, Y.; Gibbs, M.; Puthussery, J.; Gaik, S.; Ihly, R.; Hillhouse, H. W.; Law, M. *Nano Lett.* **2010**, 10, 1960-1969.
7. Luther, J. M.; Law, M.; Song, Q.; Perkins, C. L.; Beard, M. C.; Nozik, A. J. *ACS Nano* **2008**, 2, 271-280.
8. Schliehe, C.; Juarez, B. H.; Pelletier, M.; Jander, S.; Greshnykh, D.; Nagel, M.; Meyer, A.; Foerster, S.; Kornowski, A.; Klinke, C. *Science* **2010**, 329, 550-553.
9. Boneschanscher, M. P.; Evers, W. H.; Geuchies, J. J.; Altantzis, T.; Goris, B.; Rabouw, F. T.; van Rossum, S. A. P.; van der Zant, H. S. J.; Siebbeles, L. D. A.; Van Tendeloo, G.; Swart, I.; Hilhorst, J.; Petukhov, A. V.; Bals, S.; Vanmaekelbergh, D. *Science* **2014**, 344, 1377-1380.
10. Baumgardner, W. J.; Whitham, K.; Hanrath, T. *Nano Lett.* **2013**, 13, 3225-3231.
11. Katsiev, K.; Ip, A. H.; Fischer, A.; Tanabe, I.; Zhang, X.; Kirmani, A. R.; Voznyy, O.; Rollny, L. R.; Chou, K. W.; Thon, S. M.; Carey, G. H.; Cui, X.; Amassian, A.; Dowben, P.; Sargent, E. H.; Bakr, O. M. *Adv. Mater.* **2014**, 26, 937-942.
12. Li, W.; Fan, H.; Li, J. *Nano Lett.* **2014**.
13. Wang, Z.; Schliehe, C.; Wang, T.; Nagaoka, Y.; Cao, Y. C.; Bassett, W. A.; Wu, H.; Fan, H.; Weller, H. *J. Am. Chem. Soc.* **2011**, 133, 14484-14487.
14. Goodfellow, B. W.; Rasch, M. R.; Hessel, C. M.; Patel, R. N.; Smilgies, D.-M.; Korgel, B. A. *Nano Lett.* **2013**, 13, 5710-5714.
15. van Huis, M. A.; Kunneman, L. T.; Overgaag, K.; Xu, Q.; Pandraud, G.; Zandbergen, H. W.; Vanmaekelbergh, D. I. *Nano Lett.* **2008**, 8, 3959-3963.
16. Law, M.; Luther, J.; Song, Q.; Hughes, B. *Journal of the* **2008**.
17. Wills, A. W.; Kang, M. S.; Khare, A.; Gladfelter, W. L.; Norris, D. J. *ACS Nano* **2010**, 4, 4523-4530.
18. Stolle, C. J.; Harvey, T. B.; Pernik, D. R.; Hibbert, J. I.; Du, J.; Rhee, D. J.; Akhavan, V. A.; Schaller, R. D.; Korgel, B. A. *The Journal of Physical Chemistry Letters* **2013**, 5, 304-309.
19. Baumgardner, W. J.; Choi, J. J.; Bian, K.; Fitting Kourkoutis, L.; Smilgies, D.-M.; Thompson, M. O.; Hanrath, T. *ACS Nano* **2011**, 5, 7010-7019.

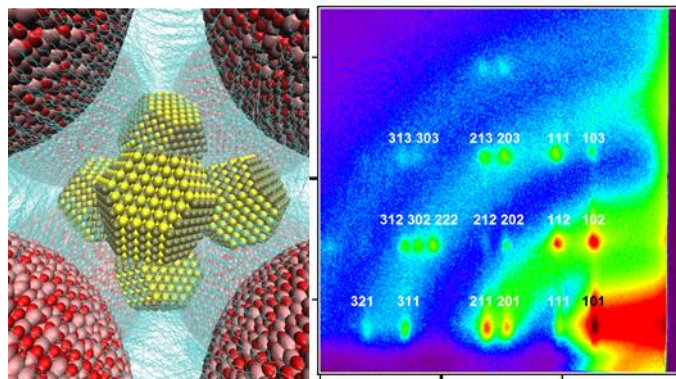
20. Arora, H.; Du, P.; Tan, K. W.; Hyun, J. K.; Grazul, J.; Xin, H. L.; Muller, D. A.; Thompson, M. O.; Wiesner, U. *Science* **2010**, 330, 214-219.
21. Yu, W. W.; Falkner, J. C.; Shih, B. S.; Colvin, V. L. *Chem. Mater.* **2004**, 16, 3318-3322.
22. Wise, F. W. *Acc. Chem. Res.* **2000**, 33, 773-780.
23. Evers, W. H.; Goris, B.; Bals, S.; Casavola, M.; de Graaf, J.; Roij, R. v.; Dijkstra, M.; Vanmaekelbergh, D. *Nano Lett.* **2012**, 13, 2317-2323.
24. Chandler, R.; Houtepen, A.; Nelson, J.; Vanmaekelbergh, D. *Physical Review B* **2007**, 75, 085325.
25. Carbone, I.; Carter, S. A.; Zimanyi, G. T. *J. Appl. Phys.* **2013**, 114, -.
26. Ong, W.; Rupich, S. M.; Talapin, D. V.; McGaughey, A. J.; Malen, J. A. *Nature Materials* **2013**, 12, 410-415.
27. Moreels, I.; Lambert, K.; De Muynck, D.; Vanhaecke, F.; Poelman, D.; Martins, J. C.; Allan, G.; Hens, Z. *Chem. Mater.* **2007**, 19, 6101-6106.
28. Guyot-Sionnest, P. *The Journal of Physical Chemistry Letters* **2012**, 3, 1169-1175.

CHAPTER 3

**CONNECTING THE PARTICLES IN THE BOX - CONTROLLED FUSION
OF HEXAMER NANOCRYSTAL CLUSTERS WITHIN AN AB₆ BINARY
NANOCRYSTAL SUPERLATTICE¹**

Binary nanocrystal superlattices present unique opportunities to create novel interconnected nanostructures by partial fusion of specific components of the superlattice. Here, we demonstrate the binary AB₆ superlattice of PbSe and Fe₂O₃ nanocrystals as a model system to transform the central hexamer of PbSe nanocrystals into a single fused particle. We present detailed structural analysis of the superlattices by combining high-resolution X-ray scattering and electron microscopy. Molecular dynamics simulations show optimum separation of nanocrystals in agreement with the experiment and provide insights into the molecular configuration of surface ligands. We describe the concept of nanocrystal superlattices as a versatile ‘nanoreactor’ to create and study novel materials based on precisely defined size, composition and structure of nanocrystals into a mesostructured cluster. We demonstrate ‘controlled fusion’ of nanocrystals in the clusters in reactions initiated by thermal treatment and pulsed laser annealing.

¹ The results presented in this chapter have been published in Ref 1. Treml, B. E.; Lukose, B.; Clancy, P.; Smilgies, D.-M.; Hanrath, T. *Sci. Rep.* **2014**, 4.



3.1 Introduction

New opportunities to create materials with properties by design continue to emerge from advances in our ability to control structure and composition of nanomaterials through wet-chemistry methodologies. Access to nanomaterial building blocks with precisely programmable size, shape, and composition has provided critical insights into our understanding of and control over fundamental structure-property relationships. At the same time, prototype nanomaterials have enabled rapid advances in nanotechnology underscored by their immense technological potential in a broad range of applications ranging from photovoltaics,²⁻⁴ catalysis,^{5, 6} energy storage,⁷ and thermoelectrics.⁸ Focus in the field is now shifting towards controlling the interactions among nanocrystals (NCs), driven by the desire to create programmable and purposeful connections between NCs and their surrounding in ordered assemblies.

Binary assemblies of NCs with dissimilar properties have drawn particular interest as a model structure for designer metamaterials in which controlled interactions between component NCs lead to magnetoresistance,^{9, 10} catalytic activity,¹¹ and conductivity¹² greater than the sum of the constituent parts.

Moreover, binary nanocrystal superlattices (BNSLs) provide a versatile experimental test bed to study clusters of NCs in confined volumes. The AB_6 superlattice, consisting of type A particles at the corners of the unit cell and a B_6 hexamer in the center position, presents a particularly interesting example. Previous studies have shown that the complete description of the interactions among NCs assembling into superlattices must go beyond the approximation of spherical or polyhedral particles.^{13, 14} To satisfactorily explain the self-assembly behavior of NCs, the molecular-level interactions of ligands bound to the NC surface and electrostatic interactions must be considered. In the specific case of the AB_6 structure, this introduces questions about the orientational alignment of the polyhedral NCs and the configuration of the ligands in the confined volume of the central hexamer.

Understanding and controlling the arrangement of NCs within isolated clusters also presents opportunities to create novel metamaterials *via* selective fusion of one component of the superlattice. ‘*Connecting the dots*’ in the cluster can be achieved by either chemical treatments (*i.e.*, exchanging or displacing the native long-chain ligands¹⁵) or physical treatments (*i.e.* compression¹⁶ or thermal annealing¹⁷). During thermal annealing, single component assemblies are susceptible towards fusion.^{17, 18} On the other hand, NCs isolated in a binary lattice have been demonstrated to be robust to coalescence.¹¹ The structural evolution of the central hexamer of an AB_6 BNSL has, to the best of our knowledge, not yet been investigated.

In this work, we use BNSLs with the AB_6 structure as a self-assembled periodic “nanoreactor”. A framework of Fe_2O_3 NCs confine a cluster of six PbSe NCs, allowing us to study the interactions among a specific number of particles assembled in the center

of the superlattice unit cell. The integration of synchrotron-based X-ray scattering and computational simulation probes the structure of the BNSL at unprecedented level of detail. We show how the periodic nature of the BNSL can be leveraged to study structure transformations by applying grazing incidence small angle X-ray scattering (GISAXS) and investigate a large number ($\sim 10^{10}$) of nanoreactors simultaneously. We demonstrate how PbSe NCs in the central hexamer are transformed into a single particle *via* thermal annealing and how the progress of the nanoreaction can be rationally controlled by changing the time scale of heating *via* laser spike annealing. We show that BNSLs are not only a novel class of metamaterials with promising properties, but also can serve as a powerful tool to study the interparticle interactions of precisely defined numbers of NCs.

We characterized the structure of the self-assembled BNSL using a suite of microscopy and scattering techniques. Analysis of samples prepared on TEM grids confirmed the assembled structure as an AB_6 (A= Fe_2O_3 , B=PbSe, $Pm\bar{3}m$ no. 221) structure comprised of a simple cubic lattice of 13.4 nm Fe_2O_3 NCs with six 4.2 nm PbSe NCs occupying the center of the unit cell. The central hexamer is structurally analogous to the arrangement of NCs in a unit cell of a body-centered tetragonal assembly. Transmission electron micrographs of the assembled BNSLs in Figures 3.1a and 3.1c show the structure of the Fe_2O_3 and PbSe NCs, respectively. Superlattice grains in the optical micrograph display square faceting concomitant with the cubic unit cell of the BNSL.

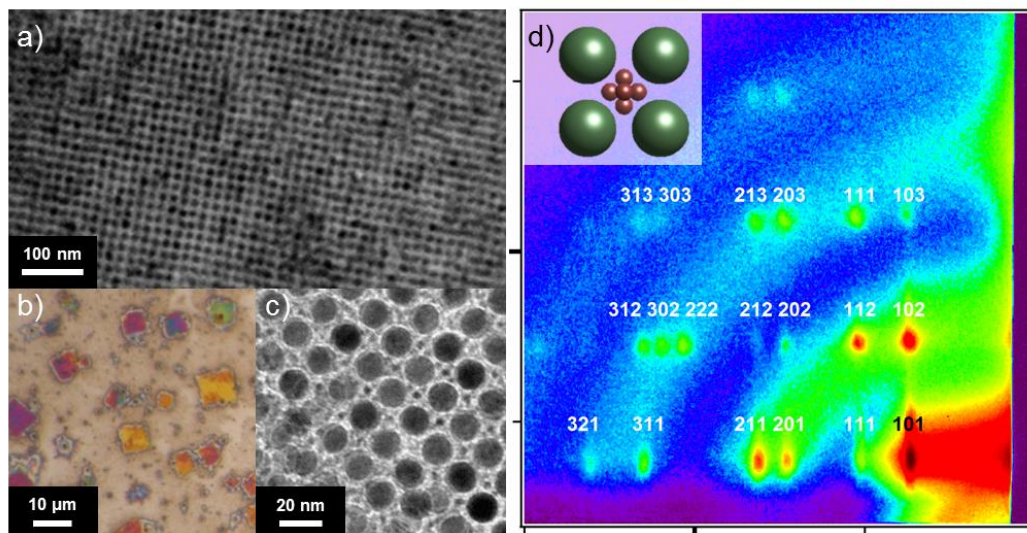


Figure 3.1: Characterization of the assembled BNSL (a) Low magnification TEM of a BNSL showing long-range ordering of the Fe_2O_3 NCs. (b) Optical micrograph of BNSL assembled on a Si wafer. (c) Higher magnification TEM showing the structure of the hexamer (d) Indexed GISAXS scattering pattern of the BNSL. Intensity shown on a logarithmic scale. Bold ticks indicate 1 nm^{-1} Inset: Model of the 001 projection of the assembled AB6 BNSL.

3.2 GISAXS Characterization of Assembled BNSLs

GISAXS provides detailed, unbiased insights into the structure of the BNSL averaged over as many as 10^{10} unit cells. GISAXS corroborates microscopic structure analysis, and adds additional information that would be impractical or impossible to obtain from electron microscopy alone. A typical GISAXS pattern is shown in Figure 3.1d. Along the horizontal axis GISAXS probes the density correlation among nanoparticles in the substrate plane; in the vertical direction density correlations perpendicular to the substrate surface are probed. Analysis of the location of scattering peaks indicates that the BNSL has a simple cubic lattice oriented with the (001) plane parallel to the substrate and a lattice constant of 17 nm. In addition, the width of the

peaks can be used to determine the average supercrystal grain size by extending the Scherrer equation to GISAXS.¹⁹ The scattering patterns give a lower bound of 81 nm for supercrystal thickness, and 186 nm for in plane size. Due to instrument resolution, only lower bounds can be established as many of the scattering peaks were near the instrumental broadening for the GISAXS setup used.

Large superlattices with a high degree of preferential orientation give rise to high quality scattering patterns with many well-resolved, intense peaks. As a result, we could extend the treatment of GISAXS developed in previous studies²⁰ to binary assemblies, and focus on the intensity of the GISAXS peaks to study the internal structure of the unit cell. Simulations of GISAXS have used the quasi-kinematic approximation to produce simulated scattering patterns and quantify NC film order^{20, 21}. Within this approach, the scattering from a NC assembly can be split into contributions from the form factor of the individual NCs and the structure factor of the assembly. The scattering from spheroidal NC can be approximated by the hard sphere form factor^{22, 23}:

$$f(q) = \frac{4}{3} \pi R^3 \rho \left[3 \frac{\sin(qR) - qR \cos(qR)}{(qR)^3} \right] \quad \text{Eq. 3.1}$$

where q is the magnitude of the scattering vector, R is the particle radius, and ρ is the electron density of the material. The calculated form factors used in further calculations are averaged over a population with mean size and standard deviation determined from TEM measurements of at least 100 particles.

The scattering peaks observed in GISAXS patterns are a result of scattering from the structure factor of a superlattice. The structure factor is calculated as:

$$S(\mathbf{q}_{hkl}) = \sum_n f_n(\mathbf{q}_{hkl}) \exp[2\pi i(hx_n + ky_n + lz_n)] \quad \text{Eq. 3.2}$$

where \mathbf{q}_{hkl} is the scattering vector for the hkl reflection, and $x_n y_n z_n$ are the fractional coordinates of the n th NC in the unit cell. We chose that for $n=1$, a Fe_2O_3 NC is located at 0,0,0 and, for $n=2$ through 7, six PbSe NCs are located at permutations of $\frac{1}{2}, \frac{1}{2}, X$ and $\frac{1}{2}, \frac{1}{2}, 1-X$. Our computational model of the scattering intensity systematically varies X to change the interparticle spacing between the PbSe NCs which is $1-2X$ in the [001] direction.

Lastly, we add a Debye-Waller factor, B , to model disorder of the first kind, which involves local deviation from ideal lattice sites without disrupting the long-range order of the supercrystal. The effect of the Debye-Waller factor on scattering is taken into account by W :

$$W(q) = \exp(-B^2 q^2) \quad \text{Eq. 3.3}$$

and is used to give the correct weight to structure and form factors in the calculations. The final intensities are then calculated from²³:

$$I(q) \propto S(q)^2 * W(q) + \left(\sum_n f_n(q) \right)^2 * (1 - W(q)) \quad \text{Eq. 3.4}$$

The large number of scattering peaks (over 15) resolved in our GISAXS analysis of the AB_6 BNSLs presented an opportunity to study the superlattice structure at an unprecedented level of detail. To match experimental and simulated scattering patterns, the intensity of nine peaks common to scattering patterns of interest and of reliable intensity were analyzed for a variety of locations of the PbSe NCs (*i.e.*, X detailed above) in the BNSL unit cell. We optimized the unit cell configuration of the model

structure based on the lowest sum of squared residuals. The residual from each peak was weighed by a factor of q^4 to account for the asymptotic q^{-4} decrease in form factor as given by Porod's Law²³:

$$r_{hkl} = q_{hkl}^4 (I_{obs} - I_{calc}) \quad \text{Eq. 3.5}$$

This choice of residual makes the structure simulation more sensitive to the structure factor information in the weak reflections at higher q , which otherwise would barely contribute to the fit. Comparison of simulated and experimental scattering intensities allowed us to precisely determine the location of the PbSe NCs in the unit cell. The structure of the confined hexamer NCs is an octahedron with side lengths of 4.7 nm and a tip-to-tip distance of 6.6 nm. The tips of the octahedron are oriented towards the center of the faces of the cube formed by the iron oxide particles. Importantly, we found that face-to-face spacing between quasi-spherical PbSe NCs is only 0.5 nm, which is significantly less than the interparticle spacings previously reported in pure PbSe NC superlattices²⁴. The tight interparticle spacing in the center hexamer introduces an interesting question: *What is the molecular configuration of the ca. 1.8 nm long oleic acid ligand in the confined cavity of the PbS hexamer?* To obtain a deeper understanding of the molecular configuration of the ligands in the center hexamer, we turn to Molecular Dynamics simulations detailed below.

3.3 Molecular Dynamics Simulations

MD simulations provide insight into the disposition of the oleic acid ligands and the extent of ligand coverage which are difficult to probe experimentally. We used a coarse-grained model to represent the intramolecular potentials; this model treats CH_x

groups in the ligands as united atoms (UA), *i.e.*, as single “beads” on the oleic acid backbone. Kaushik *et al.*¹⁴ studied the self-assembly of PbSe nanocrystals with similar ligands, adopting the model developed by Paul *et al.*²⁵ for the coarse-graining to avoid spurious ligand aggregation effects. We have adopted the same model and parameters for our study. The intermolecular interactions between NCs, ligands and NC-ligand pairs were modeled by (12-6) Lennard-Jones potential between UAs; Lorentz-Berthelot mixing rules were applied to describe the interaction between dissimilar UAs.

Consistent with TEM images, we modeled the Fe₂O₃ NCs as simple spheres. The detailed shape of the PbSe NCs in the hexamer is interesting and merits further discussion. Using the detailed experimental structure parameters as inputs to the model, we can infer the shape of the PbSe NCs to be a truncated octahedron. Truncated-cube and cuboctahedra shapes on the other hand can be ruled out since these polyhedral cannot be arranged, without overlap, into the hexamer with interparticle spacings as determined from our experimental data. Detailed aspects of the MD model are provided in the supporting information.

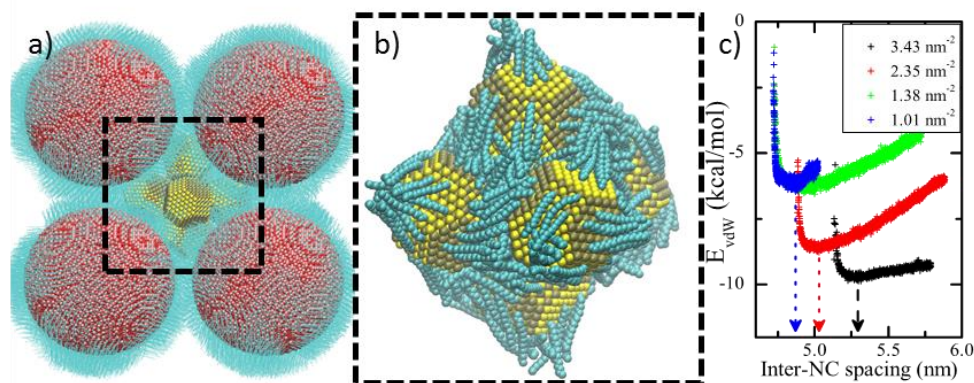


Figure 3.2: Molecular Dynamics snapshots of the system (a) BNSL formed by Fe_2O_3 spheres (red) and six PbSe NC (yellow) that define the hexamer. (b) Snapshot of the NC orientation and molecular configuration of ligands in a hexamer with a surface ligand density of 1.1 nm^{-2} . The coarse-grained UA ligands (turquoise) in the inner cavity are largely interdigitated. Atoms are shown as van der Waals spheres. (c) van der Waals potential energy as a function of inter-NC distance illustrates the relationship between equilibrium spacing and ligand coverage.

MD simulations provide insight into an aspect of BNSL assemblies that is experimentally unavailable and is, to the best of our knowledge, previously unexplored, namely, how oleic acid ligands adapt to the inhomogeneous local environment of a BNSL. The structure of the hexamer contains two types of cavities between PbSe NCs into which ligands can expand: one *interior* cavity in the center of the hexamer and eight *exterior* cavities between the PbSe NCs and the surrounding Fe_2O_3 . The ligands are largely interdigitated in the inner cavity; however, those in the outer cavities are projected towards the Fe_2O_3 NCs. To unravel the preferred orientation of NCs covered with oleic acid ligands in the hexamer, we applied steered molecular dynamics (SMD) on six NCs displaced from a common point along six axes. We have considered multiple

initial orientations to allow NCs to orient differently and hence remove bias in the results from our initial guess.

We systematically varied the PbSe NC ligand coverage to create a model of the hexamer with inter-NC separation consistent with the experimentally determined spacing. The van der Waals energy plot in Figure 3.2c shows the correlation between interparticle spacing and ligand coverage; this relationship implies that the PbSe NC surface ligand coverage density in the experimental system is slightly less than 1 nm^{-2} . The results indicate that the ligands in a PbSe hexamer can adapt to an interparticle spacing closer than has been observed in single component assemblies when there is additional free space in the assembly into which the ligands can expand. Moreover, these simulations show that the depth of the potential energy well for the central hexamer correlates directly to the ligand coverage; this trend suggests that NC rearrangement in the hexamer with sparse ligand coverage requires less energy compared to rearrangements of NCs in conventional assemblies with denser ligand coverage.

3.4 Structural Transformation of the PbS Hexamer and the BNSL During Thermal Annealing

Experimental and computational insights into the structure of the hexamer introduce the interesting prospect of controllably fusing the six particles into a single fused NC cluster. The structural analysis detailed above illustrates that the BNSL effectively confines a single hexamer unit cell of PbSe NCs in a periodic manner. This confinement opens several possibilities to process the hexamer and transform the

particles-in-a-box to novel clusters with programmable structures. The conventional approach to form connections between colloidal NCs involves chemical treatments such as ligand removal or exchange^{15, 26, 27}; however, efficient mass transport of ligands both into and out of the BNSL presents a significant challenge. Moreover, chemical ligand treatments would not be specific to the hexamer since the treatment would displace ligands from the hexamer as well as from the confining Fe₂O₃ NC framework. Thermal annealing on the other hand presents an opportunity to mitigate the transport limitation as well as selective treatment of one of the components of the binary lattice. The BNSLs contain components with both high (Fe₂O₃) and low (PbSe) thermal stability. The higher melting point of the metal-oxide NCs therefore provides a stable non-reactive framework that keeps individual hexamers separated.

Melting and sintering of NCs involves an intricate interplay of thermodynamic and kinetic aspects^{17, 28, 29} that can lead to complicated structural rearrangements.¹⁸ We hypothesized that controlling the temperature and duration of thermal annealing will allow us to decouple the thermodynamic and kinetic aspects and rationally program the resulting NC structures. Figure 3.3 illustrates three potential outcomes of structures resulting from thermal annealing of an AB₆ superlattice. The initial as-assembled superlattice structure in the upper left quadrant can be transformed by either, partial sintering inward, partial sintering outward, and complete sintering inward of the NCs.

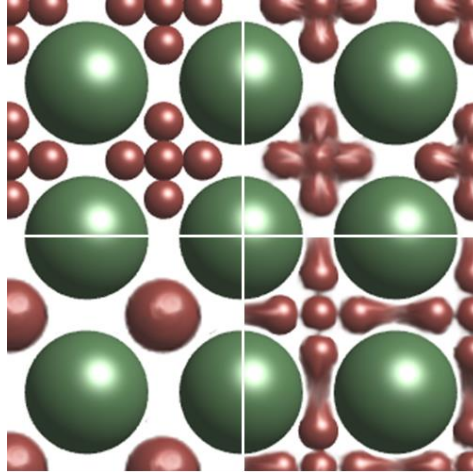


Figure 3.3: Possible outcomes of annealing the hexamer of PbSe particles (red) confined by a periodic arrangement of the Fe₂O₃ particles (green).

To understand the structural evolution of the PbSe hexamer during thermal annealing, we analyzed GISAXS patterns *in situ* while heating the sample from 30 °C to near 200 °C. Similar *in-situ* experiments previously revealed the structure evolution during annealing of a single component NC superlattice.¹⁷ An attractive aspect of studying structure transitions in an AB₆ BSNL is that we can focus on the specific fusion of a fixed number of NCs (*i.e.*, six PbSe NCs in the central hexamer). We provide a movie illustrating the evolution of the scattering patterns with temperature in the supplementary information. The *in situ* experiment reveals a gradual loss of peaks at high q -values. This trend can be attributed to disorder in the superlattice, and is quantified by the Debye-Waller factor included in our calculated GISAXS intensities. Moreover, changes in the relative intensities of the scattering peaks (*i.e.*, (201) and (211), and (103) and (113) reflections) provide an advantageous scattering fingerprint to monitor the evolution of the BSNL structure; these peaks are highlighted in Figure 3.4b. For both pairs of scattering peaks the ratio of intensities, $\frac{I_{201}}{I_{211}}$ and $\frac{I_{103}}{I_{113}}$, is initially >

1 and becomes < 1 over the course of the annealing. Since the peaks are at nearly the same q value, the change in relative intensities cannot be attributed to Debye-Waller disorder. Instead, the changing intensities indicate a change in the structure factor, and hence changes in the interior structure of the unit cell.

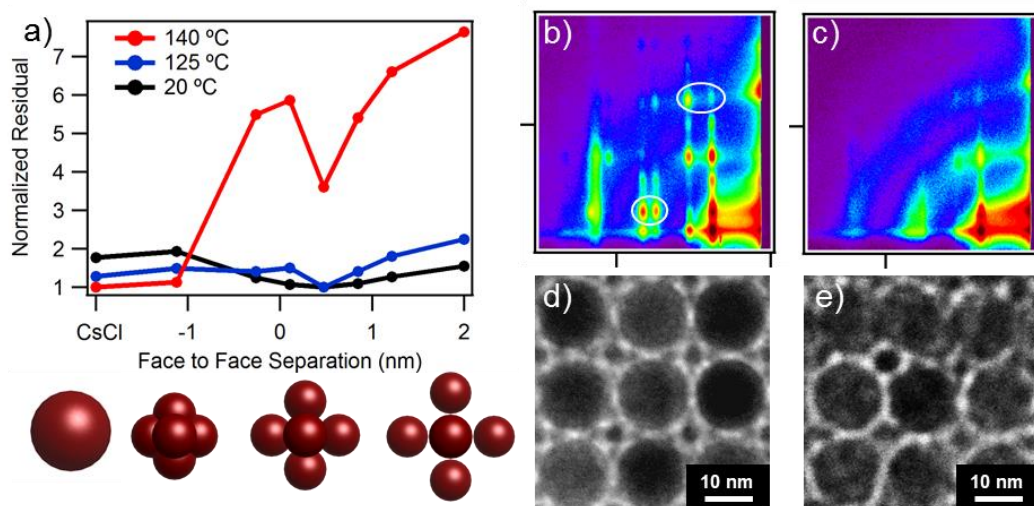


Figure 3.4: X-ray Scattering and Transmission Electron Microscopy indicate selective fusion of PbSe NCs. (a) Residuals from comparing calculated to observed scattering patterns as the annealing temperature is increased. The residuals have been normalized relative to the best-fit pattern. Below: Models of the simulated PbSe configuration for a CsCl structure, -1.2 nm, 0.5 nm, and 2 nm face to face spacing, respectively. (b, c) GISAXS patterns at 30 °C and 130 °C, respectively, white ovals indicate the scattering peaks whose relative intensities change during the annealing. Tick marks indicate 1 nm^{-1} . (d, e) TEM images of BNSL before and after annealing, showing fusion of the PbSe particles in the hexamer.

We carefully monitored the structural evolution of the PbSe hexamer throughout the *in situ* experiment, by comparing the intensities of scattering peaks at a given temperature to the simulated intensities corresponding to a range of interparticle spacings and hypothesized structural transformations. Our simulations of the scattering patterns suggest that the hexamer of PbSe NCs in the center of the initial AB_6

superlattice structure is transformed into a superstructure with a single central PbSe particle. The residuals of the scattering fits plotted in Figure 3.4a show the best fit for a hexamer with distinct particles at temperatures up to 125 °C whereas the sample annealed to 140 °C indicates a fused structure. We modeled the fused structure as either a single 7.6 nm NC or six overlapping NCs. The residual for the fit for both structures is similar so a definitive assignment of the fused structure to a single spherical particle or fused hexamer with octahedral shape is not feasible from analysis of X-ray scattering data alone. Additional high-resolution electron microscopy and tomography are required to gain deeper insights into the detailed three-dimensional structure of the fused hexamer. In the case of conventional thermal annealing, the shift from separate to fused particles occurs near a temperature of 130 °C without any apparent transition through intermediate configurations. This can be understood by considering the structure of the hexamer at the intermediate stage between separated and fused. As particles move inward, they eventually come into contact and form a neck between previously separated NCs. The particles then quickly sinter either via plastic deformation or surface diffusion of atoms to minimize the surface energy of the NCs, resulting in complete fusion of the particles.^{30,31}

The observed transition temperature is consistent with temperatures at which rotation and fusion of PbSe NCs was previously reported from *in situ* TEM experiments,³⁰ as well as the temperature for the order-disorder transition in single component PbSe NC superlattices.¹⁷ We further corroborated the results of our *in situ* experiment by annealing BNSLs assembled on TEM grids. Figure 3.4e shows that PbSe NCs have fused while remaining separate from the NCs in adjacent unit cells, indicating

that the binary assembly has effectively isolated each individual PbSe hexamer enabling controlled fusion of the particles in the box.

Beyond insights into the local structural transformation of the hexamer, *in situ* GISAXS also informs the evolution of the BNSL structure during annealing. A loss of long-range orientational ordering of the superlattice cell would be evident from a broadening of the scattering peaks into sharp rings in the 2D pattern; this trend is not observed during the thermal annealing. Instead we find that the sharp peaks indicative of long-range order become weaker and the diffuse rings corresponding to the form factor of uncorrelated NC become stronger. Furthermore, some broadening of the Bragg reflections indicates reduced average size of the superlattice grains. This can be discerned from the scattering patterns in Figure 3.4 as well as the video in the supplementary information. To clearly illustrate main trends, we azimuthally integrated the 2D scattering patterns in 1D plots analogous to powder patterns in Figure 3.5a. The resulting 1D plots reveal the transition from sharp peaks to rounded wider peak occurs first at higher q values followed by a similar transition at progressively smaller q values as the temperature is increased.

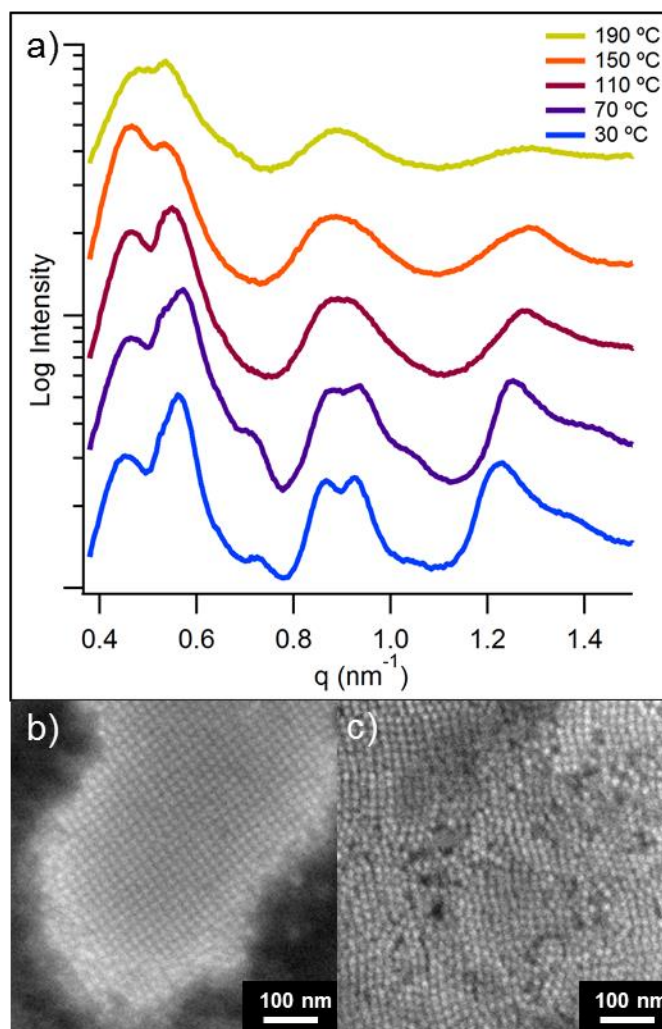


Figure 3.5: Loss of film order during thermal annealing (a) Azimuthal integrations of the scattering patterns as annealing temperature increases. (b, c) SEM images before and after annealing to 190 °C, respectively.

This structural evolution in response to thermal annealing is accounted for by the Debye-Waller factor included in the scattering simulation and fitting²¹. As the root-mean-squared displacement of particles from their average positions increases, the intensity of the structure factor is reduced and the intensity of the form factor is increased. This effect is greater at higher q values, and so higher order peaks disappear first. The calculated Debye-Waller factor contains both static and dynamic deviations

of both the PbSe and Fe₂O₃ NCs from their ideal lattice sites and we did not attempt to separate these contributions. SEM images after annealing indicate a large static disorder in Fe₂O₃ NCs – consistent with the increase in Debye-Waller factor found by fitting the scattering patterns.

The fusion of six PbSe NCs in the hexamer into one larger particle has significant implications on the structure of the BNSL. This process transforms the BSNL structure from AB₆ into an AB' (*i.e.*, CsCl, *Pm3m*) superlattice. Interestingly, based on the ratio of particle diameters, a single hard sphere of diameter 7.6 nm PbSe NC (resulting from complete fusion of the hexamer) surrounded by 13.4 nm Fe₂O₃ NCs would be more stable in the a NaCl (*i.e.*, *Fm3m*) superlattice structure with 6-fold coordination. A topotactic relation between the *Fm3m* and *Pm3m* structures is expected since the primitive cubic and face-centered cubic lattices of the Fe₂O₃ NCs are related through the primitive rhombohedron of the face-centered cubic lattice. The *Fm3m*-to-*Pm3m* transformation has been studied in atomic crystals, *e.g.*, alkali and ammonium halides³²⁻³⁴. To the best of our knowledge, these transformations have not been observed in NC superlattices. The X-ray scattering and SEM data in Figure 3.5 illustrate a disordering of the superlattice, however further work is required to better understand the binary superlattice symmetry transformation and to decisively delineate this transformation from other changes such as desorption and evaporation of the ligands and fusion of neighboring NCs.

3.5 Laser Annealing of BNSLs

Thermal annealing experiments hint towards the existence of an intermediate state involving partial fusion of the PbSe NC that is not observed by GISAXS. To decouple the kinetic and thermodynamic aspects of particle fusion, we used Laser Spike Annealing (LSA) to reduce the characteristic time scale of heating to 1 ms rather than minutes³⁵. Given the limited diffusion of the particles in the hexamer during the short-time heating pulse, we hypothesized the possibility of kinetically trapping the hexamer structure evolution in an intermediate state before it proceeds to the final state observed in the hot plate annealing experiments.

Our analysis of the GISAXS patterns of the laser annealed samples indicates that the assemblies maintain their order better compared to the *in situ* thermally annealed assemblies. Moreover, the plot of Debye-Waller factor vs annealing temperature in Figure 3.6a indicates that the laser annealed films maintain a higher degree of ordering compared to films treated at similar temperatures with conventional annealing. Importantly, our analysis of simulated and experimental scattering intensities of laser annealed BNSLs summarized in Figure 3.6c suggests that the NCs in the hexamer are only partially fused when they heated up to temperatures of 197 °C and 263 °C for short periods of time. Reducing the duration of the high-temperature pulse limits the atomic diffusion and traps the neck formation in the hexamer in a transition state. Further investigation of LSA of NC assemblies may facilitate precise control over the level of fusion occurring in a NC film, allowing for creation of ‘confined-but-connected’ NC solids through physical processing.

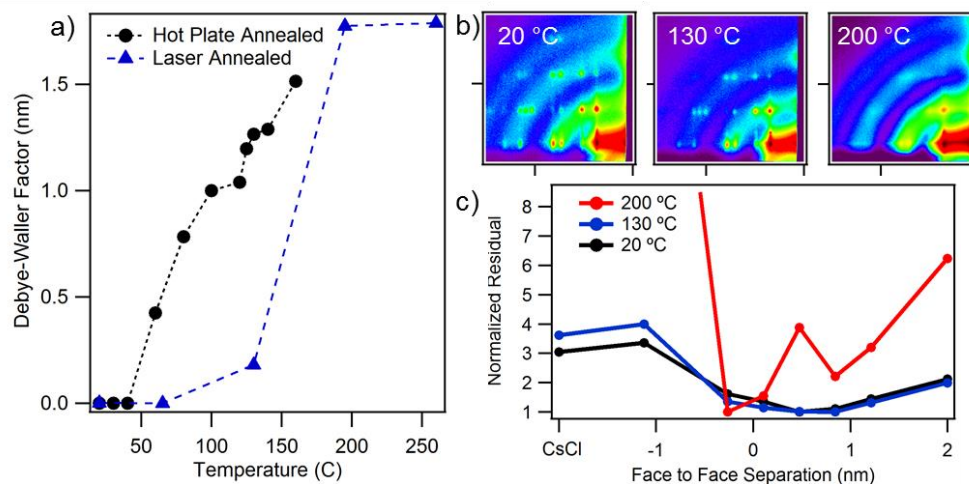


Figure 3.6: Laser Spike Annealing of BNSLs a) Debye-Waller factor from the best-fit scattering patterns. The dotted lines serve as a guide to the eye and do not represent any theoretical fit to the data. (b) GISAXS patterns for laser annealed samples showing retention of peaks at higher temperatures compared to hot plate annealing. (c) Residuals from comparison of simulated to experimental scattering intensities indicate incomplete fusion.

3.6 Conclusions

We have used the self-assembly of BNSLs to confine PbSe hexamers into a nanoreactor, enabling the study of interactions among a specifically programmable number of NCs. The periodic nature of the BNSL nanoreactor allows for analysis via GISAXS resulting in structural information averaged over as many as 10^{10} unit cells. Molecular modeling showed that the shape of the NCs had to be close to that of truncated octahedra; cube-octahedra and truncated cube shapes were shown to be incapable of forming a hexamer without fusing. Steered Molecular Dynamics simulations showed that the experimentally observed distance of 4.7 nm between NCs is only consistent with a low ligand density of about one molecule per nm^2 . The oleic acid ligands have to interdigitate strongly, in order to accommodate the closely spaced NCs. Using the enhanced thermal stability of BNSLs we observed the fusion of six

separate NCs into a single hexamer via detailed analysis of *in situ* scattering patterns. Non-equilibrium processing via LSA enables suppression of the order-disorder transition enabling higher temperature processing without disrupting the BNSL order. Both isolating particles into nanosized volumes via self-assembly of BNSLs and subsequent fast laser processing show promise to create novel designer materials that cannot be obtained by self-assembly alone.

REFERENCES

1. Treml, B. E.; Lukose, B.; Clancy, P.; Smilgies, D.-M.; Hanrath, T. *Sci. Rep.* **2014**, *4*.
2. Baxter, J.; Bian, Z.; Chen, G.; Danielson, D.; Dresselhaus, M. S.; Fedorov, A. G.; Fisher, T. S.; Jones, C. W.; Maginn, E.; Kortshagen, U.; Manthiram, A.; Nozik, A.; Rolison, D. R.; Sands, T.; Shi, L.; Sholl, D.; Wu, Y. *Energy & Environmental Science* **2009**, *2*, 559-588.
3. Milliron, D. J.; Gur, I.; Alivisatos, A. P. *MRS Bull.* **2005**, *30*, 41-44.
4. Nozik, A. J.; Beard, M. C.; Luther, J. M.; Law, M.; Ellingson, R. J.; Johnson, J. C. *Chem. Rev.* **2010**, *110*, 6873-6890.
5. Zhou, Z.-Y.; Tian, N.; Li, J.-T.; Broadwell, I.; Sun, S.-G. *Chem. Soc. Rev.* **2011**, *40*, 4167-4185.
6. Crabtree, G. W.; Sarrao, J. L. *MRS Bull.* **2012**, *37*, 1079-1088.
7. Bruce, P. G.; Scrosati, B.; Tarascon, J.-M. *Angew. Chem. Int. Ed.* **2008**, *47*, 2930-2946.
8. Vineis, C. J.; Beverly, M.; Shakouri, A.; Cruz, S. C.; Majumdar, A.; California, U. o.; DC, W.; Kanatzidis, M. G.; University, N. *Adv. Mater.* **2010**, *22*, 3970-3980.
9. Shevchenko, E. V.; Talapin, D. V.; Kotov, N. A.; O'Brien, S.; Murray, C. B. *Nature* **2006**, *439*, 55-59.
10. Dong, A.; Chen, J.; Vora, P.; Kikkawa, J.; Murray, C. *Nature* **2010**.
11. Kang, Y.; Ye, X.; Chen, J.; Qi, L.; Diaz, R. E.; Doan-Nguyen, V.; Xing, G.; Kagan, C. R.; Li, J.; Gorte, R. J.; Stach, E. A.; Murray, C. B. *J. Am. Chem. Soc.* **2013**, *135*, 1499-1505.
12. Urban, J. J.; Talapin, D. V.; Shevchenko, E. V.; Kagan, C. R.; Murray, C. B. *Nature Materials* **2007**, *6*, 115-121.
13. Ben-Simon, A.; Eshet, H.; Rabani, E. *ACS Nano* **2013**, *7*, 978-986.
14. Kaushik, A. P.; Clancy, P. *J. Comput. Chem.* **2013**, *34*, 523-532.
15. Kovalenko, M. V.; Scheele, M.; Talapin, D. V. *Science* **2009**, *324*, 1417-20.
16. Wang, Z.; Schliehe, C.; Wang, T.; Nagaoka, Y.; Cao, Y. C.; Bassett, W. A.; Wu, H.; Fan, H.; Weller, H. *J. Am. Chem. Soc.* **2011**, *133*, 14484-14487.
17. Goodfellow, B. W.; Patel, R. N.; Panthani, M. G.; Smilgies, D.; Korgel, B. A. *The Journal of Physical Chemistry C* **2011**, *115*, 6397-6404.
18. Goodfellow, B. W.; Rasch, M. R.; Hessel, C. M.; Patel, R. N.; Smilgies, D.-M.; Korgel, B. A. *Nano Lett.* **2013**, *13*, 5710-5714.
19. Smilgies, D.-M. *J. Appl. Crystallogr.* **2009**, *42*, 1030-1034.
20. Smilgies, D.; Heitsch, A.; Korgel, B. *The Journal of Physical* **2012**.
21. Heitsch, A. T.; Patel, R. N.; Goodfellow, B. W.; Smilgies, D.-M.; Korgel, B. A. *The Journal of Physical Chemistry C* **2010**, *114*, 14427-14432.
22. Glatter, O.; Kratky, O., *Small angle X-ray scattering*. Academic press London: 1982; Vol. 102.
23. Förster, S.; Timmann, A.; Konrad, M.; Schellbach, C.; Meyer, A.; Funari, S. S.; Mulvaney, P.; Knott, R. *The Journal of Physical Chemistry B* **2005**, *109*, 1347-1360.
24. Hanrath, T.; Choi, J. J.; Smilgies, D.-M. *ACS Nano* **2009**, *3*, 2975-2988.

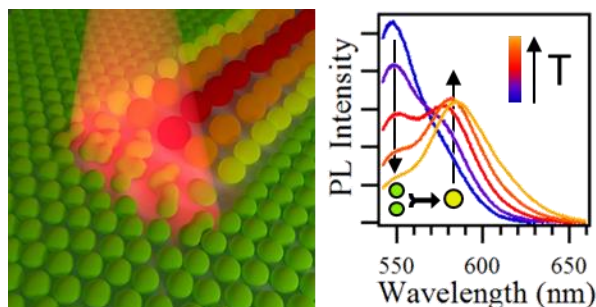
25. Paul, W.; Yoon, D. Y.; Smith, G. D. *The Journal of Chemical Physics* **1995**, 103, 1702-1709.
26. Tang, J.; Kemp, K. W.; Hoogland, S.; Jeong, K. S.; Liu, H.; Levina, L.; Furukawa, M.; Wang, X.; Debnath, R.; Cha, D.; Chou, K. W.; Fischer, A.; Amassian, A.; Asbury, J. B.; Sargent, E. H. *Nat Mater* **2011**, 10, 765-771.
27. Talapin, D. V.; Murray, C. B. *Science* **2005**, 310, 86-89.
28. Baumgardner, W.; Choi, J.; Bian, K. *ACS* **2011**.
29. Rickey, K. M.; Nian, Q.; Zhang, G.; Chen, L.; Bhat, S. V.; Wu, Y.; Cheng, G.; Ruan, X. In *Effects of rapid thermal processing and pulse-laser sintering on CdTe nanofilms for photovoltaic applications*, 2012; pp 846505-846505-11.
30. van Huis, M. A.; Kunneman, L. T.; Overgaag, K.; Xu, Q.; Pandraud, G.; Zandbergen, H. W.; Vanmaekelbergh, D. I. *Nano Lett.* **2008**, 8, 3959-3963.
31. Schapotschnikow, P.; Huis, M. A.; Zandbergen, H. W.; Vanmaekelbergh, D.; Vlugt, T. J. *Nano Lett.* **2010**, 10, 3966-3971.
32. Buerger, M. *John Wiley* **1951**, 183.
33. Kennedy, S. W.; Patterson, J. H.; Chaplin, R. P.; Mackay, A. L. *J. Solid State Chem.* **1974**, 10, 102-107.
34. Fraser, W. L.; Kennedy, S. W. *Acta Crystallographica Section B* **1972**, 28, 3101.
35. Iyengar, K.; Jung, B.; Willemann, M.; Clancy, P.; Thompson, M. O. *Appl. Phys. Lett.* **2012**, 100, -.

CHAPTER 4

μ -RAINBOW: CDSE NANOCRYSTAL PHOTOLUMINESCENCE GRADIENTS VIA LASER SPIKE ANNEALING FOR KINETIC INVESTIGATIONS AND TUNABLE DEVICE DESIGN¹

Much of the promise of nanomaterials derives from their size-dependent, and hence tunable, properties. Impressive advances have been made in the synthesis of nanoscale building with precisely tailored size, shape and composition. Significant attention is now turning towards creating thin film structures in which size-dependent properties can be spatially programmed with high fidelity. Non-equilibrium processing techniques present exciting opportunities to create nanostructured thin films with unprecedented spatial control over their optical and electronic properties. Here, we demonstrate single scan laser spike annealing (ssLSA) on CdSe nanocrystal (NC) thin films as an experimental test bed to illustrate how the size dependent photoluminescence (PL) emission can be tuned throughout the visible range and in spatially defined profiles during a single annealing step. Through control of the annealing temperature and time, we discovered that NC fusion is a kinetically limited process with a constant activation energy in over two orders of magnitude of NC growth rate. To underscore the broader technological implications of this work, we demonstrate the scalability of LSA to process large area NC films with periodically modulated PL emission, resulting in tunable emission properties of a large area film. New insights into the processing-structure-property relationships presented here offer significant advances in our fundamental understanding of kinetics of nanomaterials as well as technological implications for the production of nanomaterial films.

¹ The results presented in this chapter have been published in Ref. 1. Treml, B. E.; Jacobs, A. G.; Bell, R. T.; Thompson, M. O.; Hanrath, T. *Nano Lett.* **2015**.



4.1 Introduction

Colloidal semiconductor nanocrystals (NCs), aka quantum dots, provide versatile building blocks for emerging optoelectronic applications²⁻⁴. Based on quantum confinement effects, their absorption and emission characteristics can be rigorously controlled by adjusting the NC size. Recent advances in NC synthesis and improved understanding of the basic photophysical properties have led to remarkable advances yielding NC emitters with stable and narrow emission^{5, 6}. Among the various proposed nanocrystal technologies, their application as emitters in displays and light emitting diodes have advanced most rapidly⁷; with LED displays utilizing NC emitters are now available commercially⁸.

In parallel to advances in synthesis of precisely tailored building blocks, significant progress has also been made in assembling NCs into ordered superstructures⁹⁻¹². However, critical challenges persist in the formation of superstructures in which constituent NCs can purposefully interact due to the presence of insulating NC ligands. Several chemical and physical approaches have been developed to address this challenge, including ligand exchange¹³⁻¹⁵, thermal annealing¹⁶⁻¹⁸, and high pressure treatments¹⁹⁻²¹. An exciting, yet unexplored, opportunity of physical processing methods is the ability to apply the processing with precise spatial resolution. Successful development of this approach would provide new avenues to

create programmable properties in thin films by exploiting patterning and size-dependent properties.

In this work, we introduce the use of a spatially defined physical processing technique, single-scan laser spike annealing (ssLSA), that can be applied to create spatially modulated properties of a nanomaterial at the μm to mm length scale. We focus on CdSe NCs as a model system and show how laser annealing of CdSe NC thin films can be optimized to rigorously control the fusion of proximate NCs in the film. This approach enables unprecedented control over the spatially patterned photoluminescence (PL) emission profile. The advances presented in this paper also include fundamental insights into the activation energy and mechanisms underlying the controlled NC fusion process. Combined control over annealing time and temperature allows us to show that sintering of CdSe is a kinetically activated process with a constant activation energy for over two orders of magnitude of NC growth rate. By reducing the annealing time to sub-millisecond time scales, we are able to kinetically trap the initial stages of NC fusion and show that the NCs undergo quantized transitions similar to magic sized clusters observed in NC synthesis^{22, 23}. Moreover, the ability to precisely control the NC size and the spatial position within the film opens exciting opportunities to create thin films with tunable PL emission profiles. We take advantage of the tunable emission to produce large area films that emit light across the visible spectra with tunable CIE color coordinates. Given the prominent and growing role of size tunable properties of functional nanomaterials, the ability to produce spatially defined tunable gradients in nanomaterial properties using laser annealing has substantial promise for applications far beyond the model system studied here.

Laser annealing provides a powerful and versatile processing technique to treat nanostructured materials under conditions that would, under conventional processing conditions, lead to sintering and loss of nanostructure²⁴⁻²⁶. Specifically, laser spike annealing (LSA) is a top down process developed for the integrated circuit industry to control dopant diffusion²⁷. LSA is inherently a non-equilibrium process and has been used in other studies to provide kinetic insight on short time scales²⁸. In this work, a CO₂ laser ($\lambda=10.6\ \mu\text{m}$) was focused to a line beam ($500 \times 90\ \mu\text{m}$) which is then scanned across the sample. As illustrated in Figure 4.1a, NCs in the thin film are transparent to the incident laser beam but are indirectly heated by thermal conduction from the underlying highly doped Si substrate. This substrate acts as both a heat source during laser exposure and as a heat sink after the laser has passed, resulting in a rapid quench from high temperature²⁹. For NC films, the thermal diffusion length ($\sim 8\ \mu\text{m}$ in $250\ \mu\text{s}$, see calculation in Appendix C) is significantly larger than the average film thickness (typically 50-100 nm). This ensures that the NC film is processed at nearly isothermal conditions throughout the film thickness²⁵.

The spatial and temporal temperature profile encountered during a single scan of LSA are summarized in Figure 4.1b³⁰. The Gaussian intensity profile leads to a spatial variation in the peak annealing temperature with a typical temperature gradient of 1-2 °C/ μm . This enables us to correlate spatial characterization of a single LSA scan with temperature dependent behavior. We characterize the anneal duration by the laser dwell time, this is simply the ratio of the FWHM of the laser beam in the scan direction ($90\ \mu\text{m}$) to the laser scan velocity. The dwell time corresponds to roughly the time the sample spends within 5% of the peak temperature. In these studies, we have determined

the optimum dwell time for processing was 250 μ s to 2 ms and focus on that range in the discussion below.

Our choice of CdSe NCs as a model system for the laser annealing of NC thin films leverages the extensive knowledge base of size-dependent optical properties and rigorous synthetic control over CdSe NC size and shape^{31, 32}. Briefly, in NCs with a radius smaller than the Bohr exciton radius (\sim 6 nm for CdSe), quantum confinement effects lead to an increase in the NC energy gap roughly proportional to r^{-n} ($n\sim 1.5$)³³. In the specific case of CdSe NCs, the energy gap can be conveniently tuned across the visible spectrum from \sim 400 to 700 nm.

The as prepared CdSe NC optical properties (Figure 4.1d) exhibit an excitonic absorption peak centered at 530 nm and an emission peak at 545 nm (FWHM=30 nm). By combining the size-dependent optical properties and statistical analysis of TEM images (inset Figure 4.1d) we determined the average NC diameter to be 2.8 nm \pm 8%. The well-established size-dependent optical properties provide a convenient metric to monitor changes in the NC size; this effect has previously been exploited to monitor the evolution of NC size during synthesis as well as changes in particle size after steady state thermal annealing of NC thin films^{34, 35}.

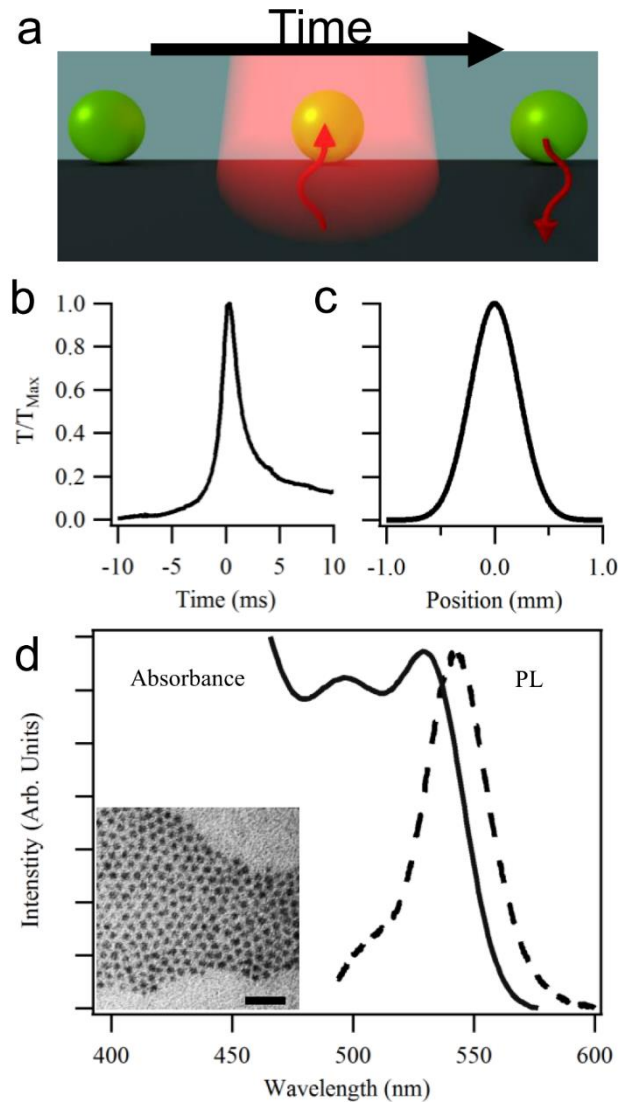


Figure 4.1: Laser annealing of CdSe NCs a) Schematic illustration of energy transport during laser spike annealing. Laser radiation is absorbed by the Si substrate, and subsequently heat is transferred into and out of the NC film by thermal conduction. b) Temporal profile of the laser anneal. c) Lateral profile of the peak annealing temperature perpendicular to the scanning direction. d) Optical absorption and PL emission of as synthesized NCs. Inset: TEM image of CdSe NCs; the scale bar is 20 nm

4.2 Characterization of Single Laser Scans

We hypothesized that the ability to create spatial temperature gradients combined with heating on μ s to ms time scales will enable the fabrication of structures

in which the fusion of proximate NCs in a thin film can be carefully controlled and spatially patterned. To test this hypothesis, we performed ssLSA across the CdSe NCs thin film and probed the evolution of the NC structure as a function of annealing temperature using a combination of optical spectroscopy and electron microscopy. Emission in the visible spectrum enables high resolution characterization of the annealed areas using a Renishaw InVia Confocal Raman microscope with a probe spot size of $\sim 2 \mu\text{m}$.

These spatial maps of the NC PL emission spectrum provide important insight into the local variation of NC size. Based on the well-known size-dependent optical properties, we can infer a change in NC size from a shift in the emission spectrum. Figure 4.2 summarizes data from ssLSA with a peak temperature of $890 \text{ }^\circ\text{C}$ and a dwell time of 2 ms. The spatial temperature profile near the peak (Figure 4.2a) correlates very well with the resulting PL emission spectra collected across the scan (Figure 4.2b). The PL map clearly shows a systematic red shift of the NC emission towards the center of the scan, where the highest temperature anneal occurs.

The observed spatial gradient in the PL emission stands in excellent agreement with the temperature gradients produced by laser annealing. The largest redshift in the emission spectra, implying the largest amount of NC fusion, occurs at the peak annealing temperature, while regions only $100 \mu\text{m}$ away, annealed at temperatures below $840 \text{ }^\circ\text{C}$, display PL unchanged from the as synthesized PL spectrum. Importantly, these results show that the PL emission from CdSe NCs can be tuned across the visible spectrum by adjusting the peak laser annealing temperature, limited only by the size of the initial NCs.

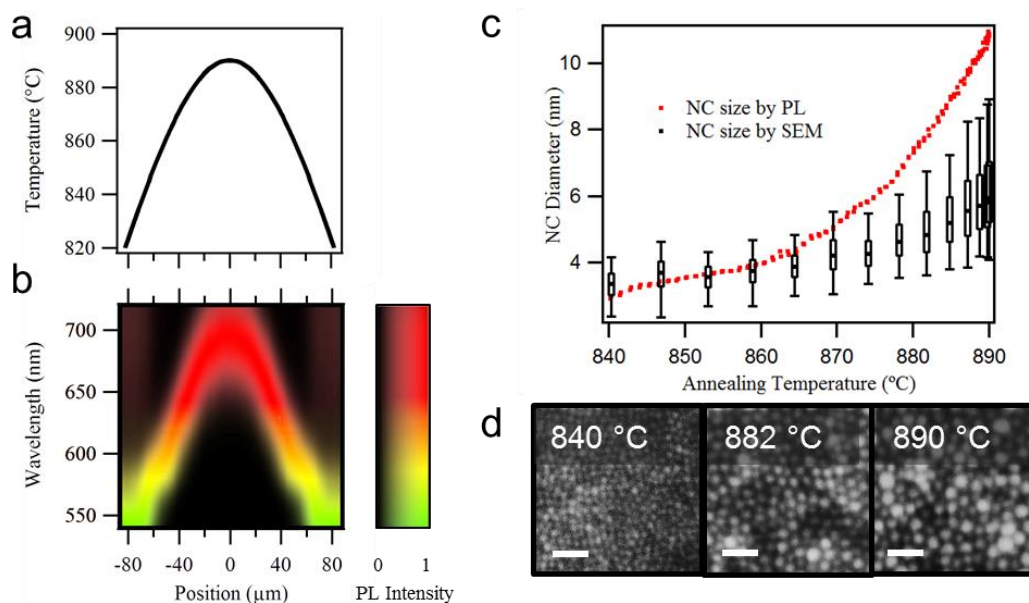


Figure 4.2: Characterization of a single laser scan a) Detailed spatial profile of the annealing temperature across an 890 °C peak scan. b) Corresponding PL spectra collected across a scan by a confocal Raman microscope. Color correlates with the wavelength while saturation indicates PL intensity relative to the maximum intensity of a spectrum. c) Comparison of NC size obtained from PL measurements and SEM for a scan with a 2 ms dwell time. Whiskers and boxes represent the 5th, 25th, 75th and 95th percentile of the measured. d) SEM images of the particle film showing increasing particle size with increased annealing temperature. The scale bars indicate 20 nm.

To confirm that the observed shift in PL emission is due to spatial variation in NC size, we examined the structure of annealed NCs using scanning electron microscopy (SEM). Figure 4.2c compares the NC diameter distribution determined from statistical analysis of SEM images (Figure 4.2d) to the NC size inferred from size-dependent PL emission spectra. We estimated the size of NC from the PL emission peak based on a polynomial fit to a set of CdSe NCs reported in previous studies (Figure C.1 in Appendix C). The side-by-side comparison of SEM and PL results reveals an interesting systematic deviation; at high temperatures, the NC diameter inferred from

the PL emission is significantly larger than the particle size distribution observed by SEM. The deviation between SEM and PL results can be attributed to two factors: First, SEM only probes the top layer of the film. While we expect near isothermal conditions throughout the film thickness, NCs at the top of the assembly are under coordinated compared to NCs in the middle of the film. With fewer neighbors, NCs in the top layer are less able to sinter during the thermal anneal. The second factor contributing to the trends evident in Figure 4.2 is that the measured PL emission do not reflect the average NC size, but instead must be understood in context of the polydisperse nature of annealed films. In NC films, Förster resonant energy transfer (FRET) from small NCs (large energy gap) to large NCs (small energy gap) is well established^{36, 37}. Consequently, PL measurements provide a measure of the largest NCs in a film rather than a measure of the average particle size.

4.3 Kinetic Analysis of Nanocrystal Fusion

To better understand how basic thermodynamic and kinetic factors impact the non-equilibrium NC fusion, we studied the combined time and temperature dependence of NC fusion. In a previous study, we developed a qualitative kinetic model to explain the change in film morphology under different laser annealing methods²⁵. Figure 4.3a shows the PL inferred NC size as a function of the peak annealing temperature for dwells from 250 μ s to 2 ms. In agreement with the qualitative kinetic model, our current work shows that both higher annealing temperatures and longer annealing times lead to increased redshift in the emission spectra, and hence increased fusion in the NC film.

The combination of a well-defined spatial temperature gradient and high spatial resolution probing of the PL emission enabled us to improve upon our earlier model and gain more detailed insights into the energetics of NC fusion. We quantified the NC growth rate as the change in NC radius (determined by our PL fitting curve) divided by the dwell time. For thermally activated NC fusion, this growth rate is expected to follow an Arrhenius relationship. Figure 4.3b shows the NC growth rate on a logarithmic scale against the inverse annealing temperature. This graph includes data from 250 μ s to 2 ms and shows consistent behavior across two orders of magnitude of NC growth rate. For clarity, data from 560 to 660 nm is shown only in 10 nm increments with the full data set shown in Figure C.3 in Appendix C. The black line in Figure 4.3b represents a fit to the Arrhenius relationship corresponding to an activation energy of 8.4 eV. Although the Arrhenius model provides a good description of the overall experimental trends, we note a systematic deviation from the trend line for small NCs with peak emission below 610 nm.

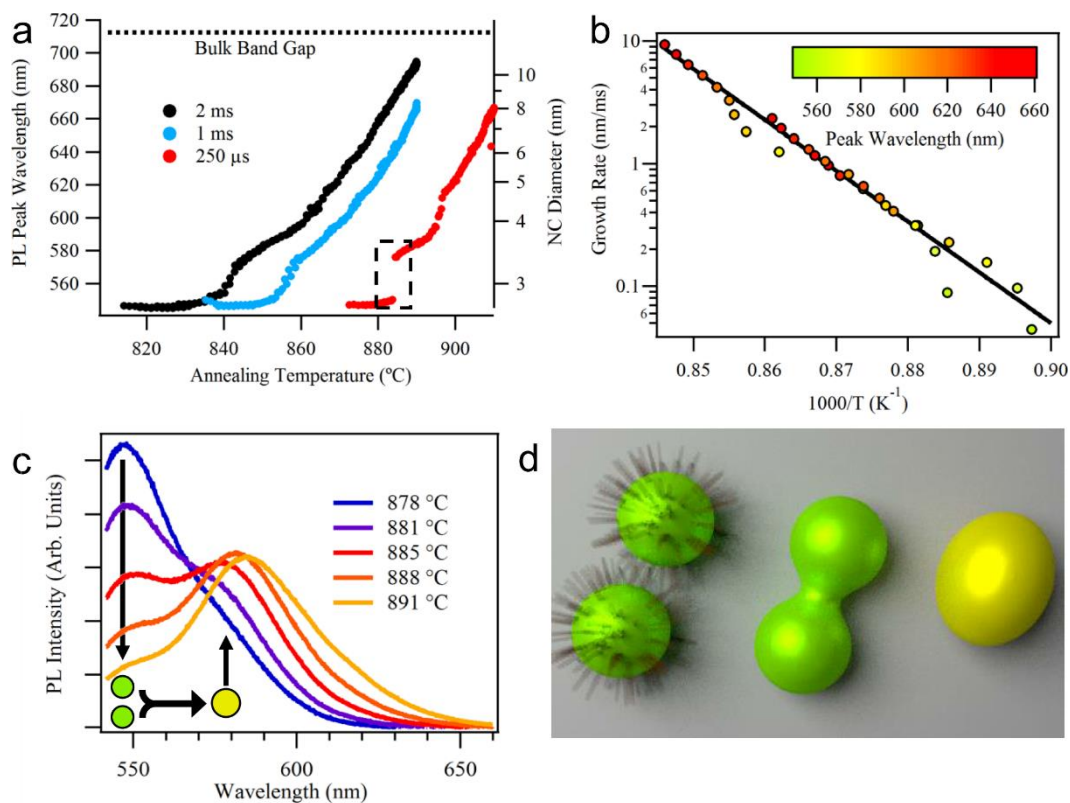


Figure 4.3: Kinetic analysis of laser annealed films a) PL peak position can be controlled by both time and temperature. The dashed box indicates the region studied in c. b) Arrhenius plot of NC growth rate indicating a constant activation energy over two orders of magnitude of NC growth rate. The black line indicates a linear fit to the data. Color indicates the peak PL wavelength of each data point. c) PL spectra showing a quantized transition during the first NC fusion event. PL spectra are normalized by the total emission. The inset shows the change in particle diameter during the monomer to dimer fusion event. d) Illustration of the three steps involved in NC fusion, ligand degradation, neck formation, and surface diffusion to form a fully fused dimer.

To understand the deviation of small NCs from the Arrhenius relationship, we examine the full PL spectra rather than just the PL peak position and consider the nature of the initial fusion events in a NC film. The evolution of PL spectra during NC fusion is most clearly revealed in a NC film annealed at 250 μs with a peak temperature of 910 $^{\circ}\text{C}$; this short annealing time enables kinetic trapping of NC populations that become

less distinct at longer annealing times. For the initial stages of NC fusion displayed in Figure 4.3c, the PL spectra show a discrete transition between two peaks at 550 nm and 580 nm. The location of these peaks correlate with CdSe NC diameters of 2.8 nm (the initial NC monomer) and 3.5 nm (a NC dimer, see Figure 4.3d). The above Arrhenius analysis is based on the assumption that PL derives from a monomodal distribution of emitters with the PL peak position as a good measure of the size of the emitters. For the multimodal emission spectra presented at short time scales and/or lower temperatures, this assumption does not hold leading to the observed systematic deviation from the Arrhenius trend. The initial NC fusion results in a change in PL peak intensity between two distinct populations rather than a continuous shift in PL peak position, resulting in erroneous NC growth rates. We provide a video showing the changing emission spectra for ssLSA with a dwell time of 250 μ s at 910 °C in the online supplementary information to clarify the transition from quantized to continuous shift in PL peak¹.

The results of both our kinetic analysis of NC growth and the observed discrete fusion events among monomer and dimer particles can be understood in context of a three-step particle fusion process suggested by previous *in situ* TEM and small angle X-ray scattering studies of NC sintering, as illustrated in Figure 4.3d. The NC fusion process involves: first, removal of the ligands that provide steric repulsion; second, the formation of bridges between NCs, which requires NC to move into contact and sometimes rotate to orient their crystallographic axis; and finally rapid fusion into a single particle via surface diffusion³⁸⁻⁴¹.

The observation of a constant activation energy over a range of NC sizes and growth rates provides evidence for the presence of a single rate-limiting process. As

ligand removal is a prerequisite for the initial NC fusion event, it cannot be the rate limiting step for growth of NCs that have already undergone fusion. Likewise, we can eliminate diffusion of surface atoms as the rate limiting step based on the discrete shift in emission spectra for small particles. If surface diffusion were rate limiting, we would expect to see emission from partially fused dimers, as observed in PbSe dimers formed in solution⁴². The emission expected from a partially fused CdSe dimer would occur at 560 nm (see calculation in Appendix C), which we do not observe. Moreover, the activation energy for self-diffusion in the bulk for Cd or Se at the temperatures studied is 1.5 eV⁴³, significantly below the activation energy we measure, even without accounting for the fact that surface diffusion faces a lower activation energy compared to bulk diffusion^{44, 45}. We therefore conclude that the formation of a neck between NCs defines the rate-limiting step for NC fusion. It is important to note that the rate limiting step itself is likely composed of multiple individual processes, such as NC rotational and translational diffusion and atomic bonding between the NCs, limiting the physical interpretation of the measured activation energy.

4.4 Tunable Emission from Nanocrystal Films

Building upon the ability to spatially tune the emission properties of NC films via ssLSA, we demonstrate the fabrication of functional CdSe NC emitter films with tunable emission profiles defined by the peak annealing temperature and spacing between anneals. This is an important advance beyond previous studies, as we tune the emission spectrum of a NC film starting from the same NC monomers as building blocks and define the film emission through processing rather than by mixing together NCs of

different sizes⁴⁶. Moreover, this approach provides unprecedented opportunity to precisely program the spatial resolution of the NC emission.

Figure 4.4a shows the emission spectra across a 3 mm wide area consisting of ssLSA scans at a peak temperature of 860 °C with a dwell time of 2 ms and a pitch of 500 μm . We deliberately limited the peak annealing temperature so that only the monomer to dimer fusion event occurred. Annealing at higher temperatures (additional NC fusion) leads to a decrease in PL intensity (Figure C4). The emission spectra of an unannealed film (**U**), the 120 μm wide stripe (**S**), and the total emission from Figure 4.4a (**T**) are shown in Figure 4.4b. Compared to the emission from the unannealed film, the total emission shows a redshift in the main emission peak as well as a tail of emission extending out to higher wavelengths due to the laser induced NC fusion. As a result of the change in the PL emission profile, the CIE coordinates of the NC film change, as shown in Figure 4.4c. In principle, any emission wavelength on the dotted line connecting **U** and **S** can be accessed by simply changing the pitch of the ssLSA, while the coordinates of **S** can be changed by controlling the peak annealing temperature. Combined with a high efficiency blue LED, these LSA NC films therefore have the potential to produce white light with tunable CIE coordinates and high color rendering index.

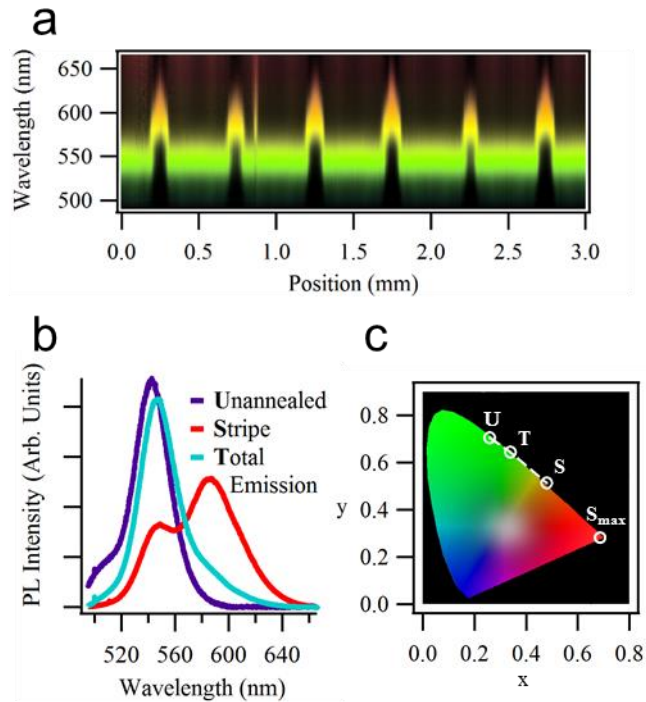


Figure 4.4: Large area tunable emission from laser annealed NC films

a) PL spectra across a 3 mm region of periodically spaced ssLSA. Spectra are normalized to the peak intensity. Color corresponds to wavelength and saturation corresponds to intensity as shown in Figure 4.2b. b) PL spectra of unannealed particles (U), a single ssLSA stripe (S), and the total emission from Figure 4.4a (T). Emission spectra are normalized such that the total integrated emission is constant. c) Location of the three emission spectra in Figure 4.4b on the CIE 1931 chromaticity diagram. By changing the pitch of ssLSA, any location along the dotted line could be achieved. S_{\max} indicates the bulk bandgap of CdSe; the physical limit of light emission for this materials system.

4.5 Conclusions

High resolution spectroscopic and microscopic characterizations coupled with the thermal gradients from single scan laser spike annealing were used to study the fusion of CdSe NC films. We show that laser-annealed NCs sinter via a kinetically limited process with a constant activation energy over two orders of magnitude of NC growth rate and identify the rate limiting step as the formation of necks between pairs

of NCs. To underscore the broader technological implications of our work, we showed how periodic modulation of the NC PL properties via laser annealing can change the CIE coordinates of the NC film emission enabling tunable film properties from a single NC feedstock. While this work represents a proof of concept using CdSe NCs, we believe that both the fundamental kinetic studies as well as periodic property manipulation for applications can be extended to a wide range of nanomaterials with size dependent properties.

REFERENCES

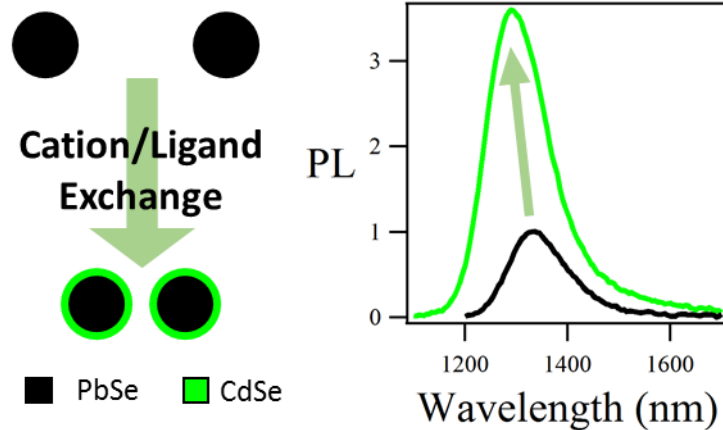
1. Treml, B. E.; Jacobs, A. G.; Bell, R. T.; Thompson, M. O.; Hanrath, T. *Nano Lett.* **2015**.
2. Sargent, E. H. *Adv. Mater.* **2008**, *20*, 3958-3964.
3. Nozik, A. J.; Beard, M. C.; Luther, J. M.; Law, M.; Ellingson, R. J.; Johnson, J. C. *Chem. Rev.* **2010**, *110*, 6873-6890.
4. Shirasaki, Y.; Supran, G. J.; Bawendi, M. G.; Bulovic, V. *Nat Photon* **2013**, *7*, 13-23.
5. Ghosh, Y.; Mangum, B. D.; Casson, J. L.; Williams, D. J.; Htoon, H.; Hollingsworth, J. A. *J. Am. Chem. Soc.* **2012**, *134*, 9634-9643.
6. Chen, O.; Zhao, J.; Chauhan, V. P.; Cui, J.; Wong, C.; Harris, D. K.; Wei, H.; Han, H.-S.; Fukumura, D.; Jain, R. K.; Bawendi, M. G. *Nat Mater* **2013**, *12*, 445-451.
7. Talapin, D. V.; Steckel, J. *MRS Bull.* **2013**, *38*, 685-691.
8. Bourzac, K. *Nature* **2013**, *493*, 283.
9. Shevchenko, E. V.; Talapin, D. V.; Kotov, N. A.; O'Brien, S.; Murray, C. B. *Nature* **2006**, *439*, 55-59.
10. Li, R.; Bian, K.; Hanrath, T.; Bassett, W. A.; Wang, Z. *J. Am. Chem. Soc.* **2014**, *136*, 12047-12055.
11. Bian, K.; Choi, J. J.; Kaushik, A.; Clancy, P.; Smilgies, D.-M.; Hanrath, T. *ACS Nano* **2011**, *5*, 2815-2823.
12. O'Brien, M. N.; Jones, M. R.; Lee, B.; Mirkin, C. A. *Nat Mater* **2015**, *14*, 833-839.
13. Dong, A.; Jiao, Y.; Milliron, D. J. *ACS Nano* **2013**, *7*, 10978-10984.
14. Lingley, Z.; Lu, S.; Madhukar, A. *Nano Lett.* **2011**, *11*, 2887-2891.
15. Kovalenko, M. V.; Scheele, M.; Talapin, D. V. *Science* **2009**, *324*, 1417-20.
16. Baik, S. J.; Kim, K.; Lim, K. S.; Jung, S.; Park, Y. C.; Han, D. G.; Lim, S.; Yoo, S.; Jeong, S. *Journal of Physical Chemistry C* **2011**, *115*, 607-612.
17. Niu, Y.-H.; Munro, A. M.; Cheng, Y. J.; Tian, Y.; Liu, M. S.; Zhao, J.; Bardecker, J. A.; Plante, J. L.; Ginger, D. S.; Jen, A. Y. *Adv. Mater.* **2007**, *19*, 3371-3376.
18. Drndić, M.; Jarosz, M. V.; Morgan, N. Y.; Kastner, M. A.; Bawendi, M. G. *J. Appl. Phys.* **2002**, *92*, 7498-7503.
19. Li, W.; Fan, H.; Li, J. *Nano Lett.* **2014**.
20. Li, B.; Wen, X.; Li, R.; Wang, Z.; Clem, P. G.; Fan, H. *Nat Commun* **2014**, *5*.
21. Wang, Z.; Schliehe, C.; Wang, T.; Nagaoka, Y.; Cao, Y. C.; Bassett, W. A.; Wu, H.; Fan, H.; Weller, H. *J. Am. Chem. Soc.* **2011**, *133*, 14484-14487.
22. Evans, C. M.; Guo, L.; Peterson, J. J.; Maccagnano-Zacher, S.; Krauss, T. D. *Nano Lett.* **2008**, *8*, 2896-2899.
23. Kudera, S.; Zanella, M.; Giannini, C.; Rizzo, A.; Li, Y.; Gigli, G.; Cingolani, R.; Ciccarella, G.; Spahl, W.; Parak, W. J. *Adv. Mater.* **2007**, *19*, 548-552.
24. Baumgardner, W. J.; Choi, J. J.; Bian, K.; Fitting Kourkoutis, L.; Smilgies, D.-M.; Thompson, M. O.; Hanrath, T. *ACS Nano* **2011**, *5*, 7010-7019.
25. Treml, B. E.; Robbins, A. B.; Whitham, K.; Smilgies, D.-M.; Thompson, M. O.; Hanrath, T. *ACS nano* **2015**, *9*, 4096-4102.

26. Lien, Y.-C.; Shieh, J.-M.; Huang, W.-H.; Tu, C.-H.; Wang, C.; Shen, C.-H.; Dai, B.-T.; Pan, C.-L.; Hu, C.; Yang, F.-L. *Appl. Phys. Lett.* **2012**, 100, 143501.
27. Shima, A.; Yun, W.; Somit, T.; Hiraiwa, A. In *Ultra-shallow junction formation by non-melt laser spike annealing for 50-nm gate CMOS*, VLSI Technology, 2004. Digest of Technical Papers. 2004 Symposium on, 15-17 June 2004, 2004; pp 174-175.
28. Jung, B.; Sha, J.; Paredes, F.; Chandhok, M.; Younkin, T. R.; Wiesner, U.; Ober, C. K.; Thompson, M. O. *ACS Nano* **2012**, 6, 5830-5836.
29. Iyengar, K.; Jung, B.; Willemann, M.; Clancy, P.; Thompson, M. O. *Appl. Phys. Lett.* **2012**, 100, -.
30. Jacobs, A. G.; Jung, B.; Jiang, J.; Ober, C. K.; Thompson, M. O. *Journal of Micro/Nanolithography, MEMS, and MOEMS* **2015**, 14, 031205.
31. Manna, L.; Scher, E. C.; Alivisatos, A. P. *J. Am. Chem. Soc.* **2000**, 122, 12700-12706.
32. Jasieniak, J.; Smith, L.; Embden, J. v.; Mulvaney, P.; Califano, M. *The Journal of Physical Chemistry C* **2009**, 113, 19468-19474.
33. Brus, L. E. *The Journal of Chemical Physics* **1984**, 80, 4403-4409.
34. Peng, X.; Wickham, J.; Alivisatos, A. P. *J. Am. Chem. Soc.* **1998**, 120, 5343-5344.
35. Farva, U.; Park, C. *Sol. Energy Mater. Sol. Cells* **2010**, 94, 303-309.
36. Kagan, C. R.; Murray, C. B.; Nirmal, M.; Bawendi, M. G. *Phys. Rev. Lett.* **1996**, 76, 1517-1520.
37. Crooker, S. A.; Hollingsworth, J. A.; Tretiak, S.; Klimov, V. I. *Phys. Rev. Lett.* **2002**, 89, 186802.
38. Chen, Y.; Palmer, R. E.; Wilcoxon, J. P. *Langmuir* **2006**, 22, 2851-2855.
39. Ingham, B.; Lim, T. H.; Dotzler, C. J.; Henning, A.; Toney, M. F.; Tilley, R. D. *Chem. Mater.* **2011**, 23, 3312-3317.
40. van Huis, M. A.; Kunneman, L. T.; Overgaag, K.; Xu, Q.; Pandraud, G.; Zandbergen, H. W.; Vanmaekelbergh, D. I. *Nano Lett.* **2008**, 8, 3959-3963.
41. Lim, T. H.; McCarthy, D.; Hendy, S. C.; Stevens, K. J.; Brown, S. A.; Tilley, R. D. *ACS Nano* **2009**, 3, 3809-3813.
42. Hughes, B. K.; Blackburn, J. L.; Kroupa, D.; Shabaev, A.; Erwin, S. C.; Efros, A. L.; Nozik, A. J.; Luther, J. M.; Beard, M. C. *J. Am. Chem. Soc.* **2014**, 136, 4670-4679.
43. Sharma, B. *CRC Handbook of Chemistry and Physics*, CRC Press, Boca Raton, FL **1998**, 1999, 12-104.
44. Mo, Y. W.; Kleiner, J.; Webb, M. B.; Lagally, M. G. *Phys. Rev. Lett.* **1991**, 66, 1998-2001.
45. Seebauer, E. G.; Allen, C. E. *Prog. Surf. Sci.* **1995**, 49, 265-330.
46. Sedat, N.; Hilmi Volkan, D. *Nanotechnology* **2007**, 18, 405702.

CHAPTER 5
SIMULTANEOUS LIGAND AND CATION EXCHANGE IN PbSe/CdSe
NANOCRYSTAL FILMS¹

Trap states formed at the surface of colloidal semiconductor nanocrystals can have deleterious impact on performance in emerging optoelectronic applications. To mitigate surface traps in nanocrystal thin films we investigated simultaneous surface passivation and ligand exchange for PbSe nanocrystal films via treatment with a cadmium acetate solution. We show that a kinetically limited surface cation exchange produces a thin $\text{Cd}_x\text{Pb}_{1-x}\text{Se}$ shell that effectively passivates the nanocrystal surface as confirmed by increased photoluminescence intensity and photoluminescence lifetime. Ligand exchange to acetate ligands is confirmed via Fourier transform infrared spectroscopy and grazing incidence small angle X-ray scattering. We studied the impact of the cadmium acetate treatment on interparticle coupling and found that the reduced interparticle spacing and limited shell thickness leads to increased Förster resonant energy transfer in nanocrystal films. Simultaneous cation/ligand exchange enables the production of heterostructured nanocrystal films with properties like Quasi-Type II nanocrystals synthesized in solution.

¹The results presented in this chapter have been published in Ref 1. Treml, B.; Yang, J.; Wise, F.; Hanrath, T. *Chem. Phys.* **2015**.



5.1 Introduction

Recent years have borne witness to tremendous progress in the fabrication of colloidal semiconductor nanocrystals (NCs) with precise control over size, shape, and composition. Availability of these materials has led to a surge of promising proof-of-concept devices that exploit their tunable optical and electronic properties²⁻⁵. An emerging consensus from the work on these devices is that sustained progress towards their technological potential requires deeper understanding and rigorous control over the surface states. Specifically in optoelectronics, surface states have been implicated as the cause for limited lifetime and mobility of carriers leading to reduced performance of devices^{6,7}.

A common method to mitigate surface states is through the synthesis of core-shell NCs. Depending upon the specific alignment between the energy levels of the core and shell, one or both carrier types can be confined to the core and thereby isolated from surface trap states.^{8,9} These structures are particularly desirable for applications where a high fluorescence quantum yield (QY) is required such as LEDs^{2, 10} and in biolabeling^{11,12}. This technique has been successful for a variety of materials systems, such as CdSe/ZnS¹³ and PbX/CdX (X=S, Se, Te)^{14,15} and has been extended to multi-shelled and alloyed shelled NCs^{16,17}. Beyond increased QY, PbSe/CdSe NCs have been shown to have impressive multiple exciton generation (MEG) capabilities due to

stabilization of high energy holes in the CdSe shell¹⁸. These NCs are currently the best performing MEG materials, surpassing PbSe nanorods¹⁹. PbS/CdS core-shell particles have also shown improved open circuit voltage (V_{oc}) in solar cells compared to core-only devices^{20, 21} as well as reduced turn on voltage and increased efficiency in IR LEDs.^{22, 23}

In parallel to the development of core-shell structures, other passivation strategies have been studied to improve the surface passivation of NCs and NC thin films. In particular, passivation methods involving inorganic or atomic species as ligands have enabled significant advances to passivate the surface while at the same time reducing interparticle spacing to enhance charge transport through the NC film.^{24, 25}. The most successful atomic ligands in PV applications have been halides (Cl, I, Br) incorporated either during synthesis or as part of a ligand exchange procedure^{24, 26}. The results of these treatments have been an increase in the efficiency of NC solar cells via increased V_{oc} , again attributed to passivation of trap states. Other atomic passivation schemes have been investigated with the same goals. Sequential treatments with ionic solutions of chalcogenide and lead that remove capping ligands and passivate surfaces have been shown to produce inorganically connected lead chalcogenide NC thin films with mobilities above $4 \text{ cm}^2/\text{Vs}$ ²⁷. Passivation of NC surfaces via atomic layer deposition also enables high mobilities in NC assemblies as well as MEG approaching solution phase yields^{28, 29}. In these completely inorganic nanocrystal arrays, carrier trapping and scattering is reduced.

Given the sensitive nature of the NC surface, minimizing the processing steps between synthesis and device operation is desirable to avoid degrading the NC surface. In this work we present a single step process that simultaneously passivates NC surfaces via limited cation exchange as well as decreases interparticle spacing via ligand exchange. Treatment of PbSe NCs with cadmium acetate (CdAc) results in increased

steady state PL intensity indicating passivation of trap states on the surface of NCs as well as increased energy transfer in NC films due to the reduction of interparticle spacing.

5.2 Surface Limited Cation Exchange

We focused our study on colloidal PbSe NCs with a diameter of 4.0 nm +/- 0.35 nm. Figure 5.1 shows the absorption spectra of the PbSe NC films before and after CdAc treatment. The excitonic peak blue shifts and broadens after a 30s soak in an ethanolic solution of CdAc. We interpret the blue shift as increased quantum confinement compared to untreated films. Previous studies have shown that cadmium can replace lead in PbX (X=S,Se,Te) NCs, consuming the originally synthesized NC and producing a CdX shell^{14, 15, 30}. TEM of particles before and after CdAc treatment show no change in size after treatment, indicating that the treatment did not etch the surface of the particle. We conclude that cation exchange has produced a PbSe/CdSe heterostructure, as has been observed via HRTEM in earlier studies³¹.

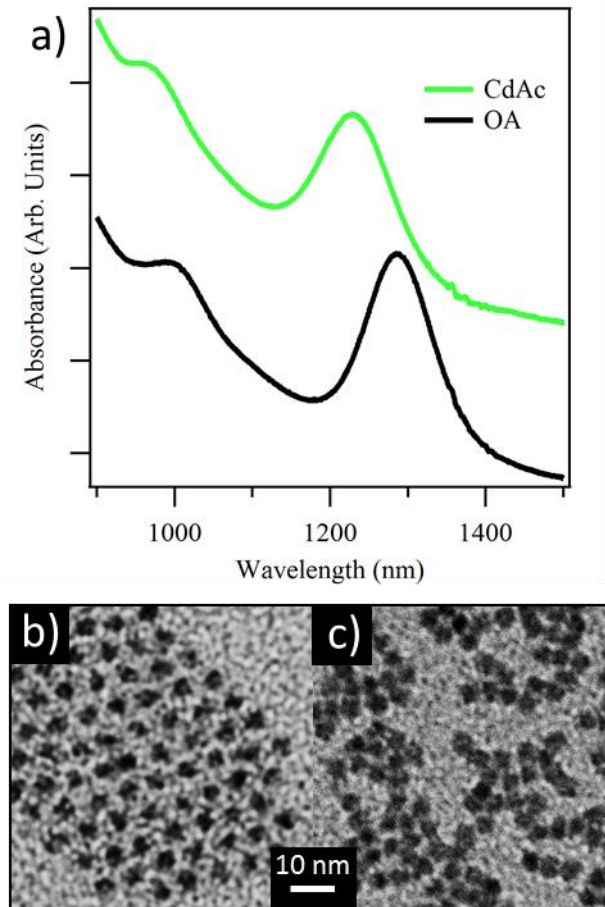


Figure 5.1: a) Optical absorption of PbSe nanocrystal films with Pb-oleate surface termination (black) and Cd-acetate surface termination (green) the blueshift in peak formation indicates increased exciton confinement due to cation exchange. b,c) TEM images of Pb-oleate and Cd-Acetate terminated NCs respectively.

To explain the blue shift of the excitonic peak we use, as a first approximation, a continuum model to represent the core-shell structure and assume uniform coverage of a CdSe layer. Previous studies of PbX/CdX core shell systems have matched PbSe core sizes observed in TEM to the empirical curve of energy *versus* size developed by Moreels *et al*³²⁻³⁵. From the change in excitonic absorption peak, this model predicts a 0.15 nm reduction in the radius of the PbSe core; this would correspond to a uniform CdSe shell of half the Pb-Se bond length. Clearly, the simple continuum model leads to a non-physical result. Instead of forming a well-defined core-shell structure, we

conclude that the cation exchange must be limited to a submonolayer during the treatment.

Moreover, a more accurate description of the PbX/CdS heterostructure must also take NC shape and faceting into account. PbSe NCs are commonly considered as stoichiometric cores, with a metal rich surface layer including Pb terminated {111} facets.^{36, 37} A model of a PbSe NC with {100} and {111} facets truncated at 2 nm from the center of the NC, shown in Figure 5.2a, has 40% of the cations on the surface. Energy dispersive X-ray spectroscopy (Figure D.1 in Appendix D) indicates that Cd makes up 23% of the cations in the CdAc treated film, in agreement with the shift in excitonic peak that indicates about half a monolayer of surface cation exchange. High-resolution TEM studies of PbX/CdX core/shell structures have shown preferential cation exchange on the {111} crystal facets³¹. Given this model of a PbSe NC, and evidence for preferential cation exchange on {111} facets in previous studies, we suggest that the submonolayer exchange may occur predominantly on the {111} facets of a NC. Figure 5.2a shows a model of a PbSe NC before and after cation exchange limited to the Pb terminated {111} facets.

To improve our understanding of the optical properties of CdAc-treated PbSe NC films, we examined the photoluminescence (PL) of NC films. The Quasi-Type II energy level alignment in PbSe/CdSe is predicted to result in delocalization of electrons throughout the heterostructure whereas holes remain confined to the PbSe core³². In light of this energy level alignment in the heterostructure, we can interpret increase in PL in PbSe/CdSe heterostructures compared to the initial PbSe system as a reduction of hole trapping at surface states due to increased confinement^{9, 18, 32, 38}. Figure 5.2b,c shows that CdAc treated 4 nm PbSe NC films exhibit increased PL and increased PL lifetime compared to untreated NC films, as shown in Figure 5.2b and 2c. The magnitude of the increase in PL (~3X increase) agrees well with the solution based

measurements performed on PbSe/CdSe core-shell particles with submonolayer thickness obtained following 19 hours of cation exchange¹⁵. This comparison confirms our interpretation of the blueshift in absorption, that CdAc treatment leads to formation of a PbSe/CdSe heterostructured film.

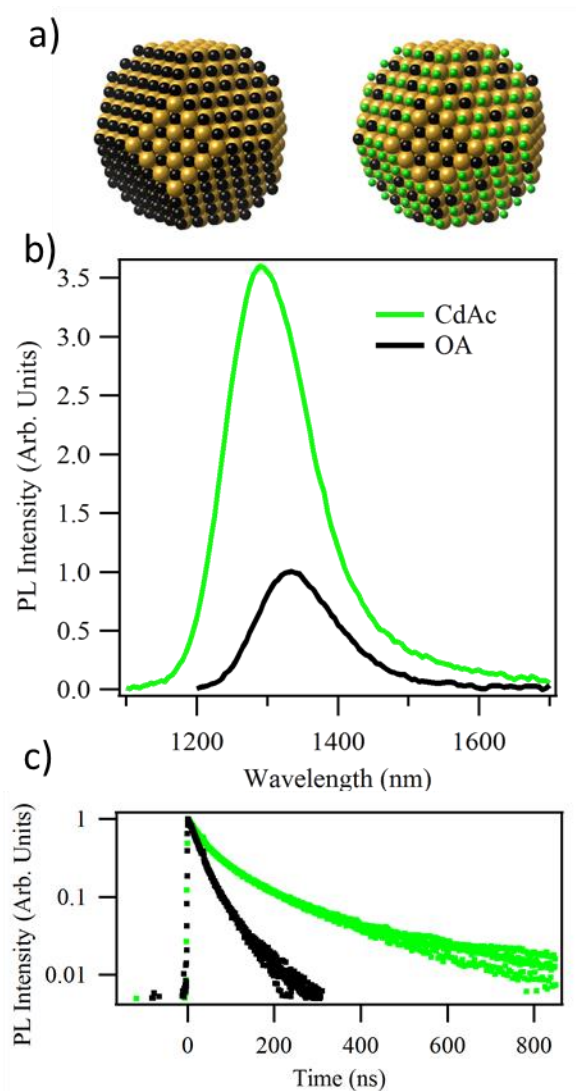


Figure 5.2: a) Atomistic models of a PbSe NC before and after submonolayer cation exchange. Lead cations are black, cadmium cations are green. b) Photoluminescence spectra of 4 nm OA passivated and CdAc passivated NC films. The blueshift and increase in PL intensity indicate surface passivation via cation exchange. c) Time resolved PL of these films measured at the peak emission wavelength showing increased lifetime following cation/ligand exchange.

5.3 Simultaneous Ligand Exchange

The significant change of the PbSe NC optical properties in response to the CdAc treatment leads to the question: *What is the fate of the oleate ligand that was initially bound to the PbSe NC surface?* In wet chemical PbSe/CdSe core-shell synthesis, Cd is supplied by Cd-oleate and so oleate and oleic acid ligands are plentiful in solution and continue to passivate the surface and provide colloidal stability to the NCs after cation exchange. In contrast, our work employs CdAc, so we hypothesized that the acetate might displace the longer chain oleate from the NC surface. FTIR absorption spectra in Figure 5.3a show a 70% reduction in the integrated intensity of C-H stretches near 2900 cm^{-1} which come predominantly from the aliphatic tail of oleate ligands, while the carboxylate stretching peaks near 1550 cm^{-1} and 1400 cm^{-1} common to both oleate and acetate are retained. The decrease, but not complete absence, of the C-H stretching peaks indicates an incomplete ligand exchange with oleate ligands still in the film after CdAc treatment. If cation exchange occurs via a Z-type ligand exchange of neutral metal carboxylate complexes, the carboxylate ligands will be exchanged simultaneously with the cations. In addition, the solvent, ethanol, has been shown to remove Z-type ligands from NC surfaces and may enhance the rate of cation/ligand exchange³⁹.

To determine how the change in ligand coverage and composition impacts interparticle spacing, we turned to grazing-incidence small-angle X-ray scattering (GISAXS) of NC thin films. GISAXS shows that the CdAc treatment significantly reduces the nearest neighbor separation of 7.1 nm in the OA passivated film to 5.5 nm in the CdAc passivated films. The surface to surface spacing after cation/ligand exchange is larger than expected for acetate passivated particles⁴⁰, which we attribute to the incomplete ligand exchange that occurs. Notably, the scattering data also show that long-range ordering is substantially preserved although an unambiguous

identification of the superlattice symmetry after cation/ligand exchange is not possible. The reduced interparticle separation measured by GISAXS is consistent with the intimate spacing between NCs evident from TEM (Figure 5.1).

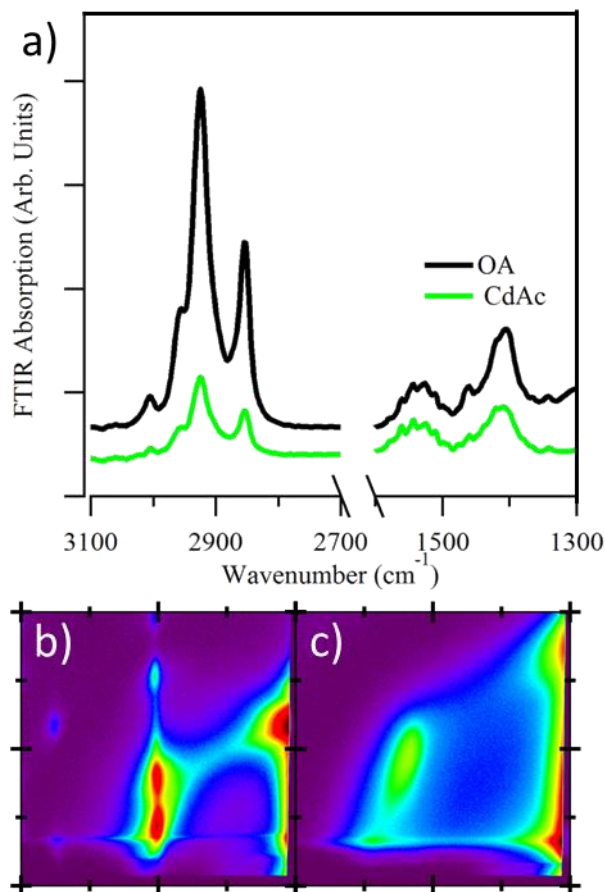


Figure 5.3: Ligands are also exchanged during CdAc treatment. a) FTIR absorption of NC assemblies shows loss of C-H stretching peaks, but retention of carboxylate binding group at the NC surface. b) As a result of the ligand exchange, NC spacing is reduced in NC films as evidenced by a shift in GISAXS to higher q values. Major ticks indicate 1 nm^{-1}

5.4 Probing Transport via Photoluminescence

Collectively, the reduced interparticle spacing (from GISAXS) and reduced surface trapping (from PL) suggests that charge transport may be improved. To investigate interparticle electronic coupling, we take advantage of the increased PL intensity of cation/ligand exchanged films to study exciton transport via steady state and

time resolved photoluminescence (TRPL). We prepared films containing large bandgap particles (1.2 eV, 2.6 nm) and small bandgap (0.95 eV, 4 nm) particles in a 100:1 ratio. The larger particles act as luminescent traps which accept excitons from the donor NCs⁴¹. The 0.25 eV (~ 10 kT) difference in energy gap between the acceptors and the surrounding matrix of smaller NC will suppress exciton transport away from the acceptor particles. Figure 5.4a shows the alignment between the conduction and valence bands of donor and acceptor particles based on the work of Jasieniak *et al*⁴².

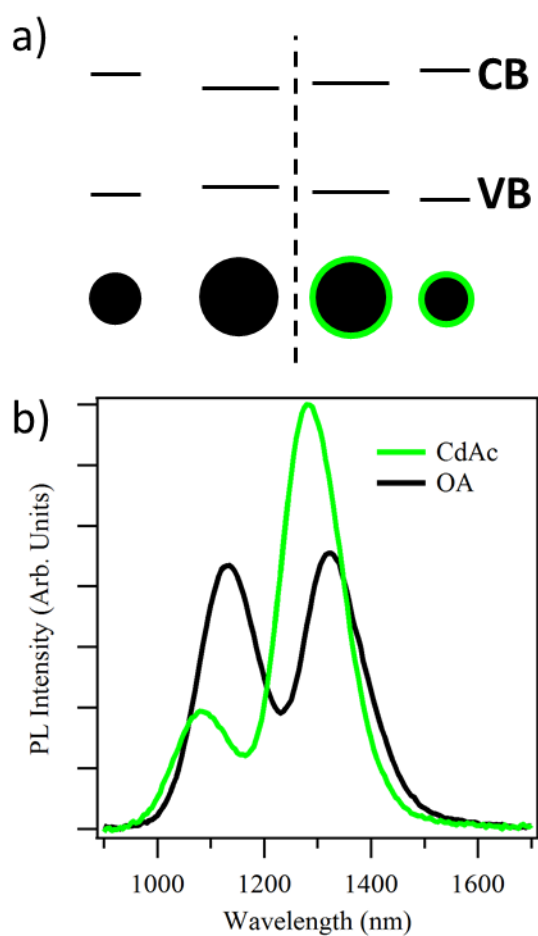


Figure 5.4: Mixed films of donor (2.6 nm) and acceptor (4 nm) particles a) Energy level alignment and particle spacing between donor and acceptors before (left) and after (right) CdAc treatment. Particle size and energy alignment match the sizes determined from TEM. b) Photoluminescence from mixed NC films showing increased acceptor emission after cation/ligand exchange. Spectra are normalized by the total PL emission.

Since the majority of excitons are generated in the donor matrix, we can monitor emission from acceptor particles as a convenient measure of the ability of carriers to diffuse in the mixed NC films. We use the model developed by Zhitmirsky *et al* in equation 5.1 to analyze the steady state emission from mixed NC films⁴¹.

$$\tau_{Film}^{-1} = \tau_D^{-1} + vN_A\sigma_A + vN_T\sigma_T \quad \text{Eq. 5.1}$$

Where τ represents the average lifetime of the film as a whole and the donor matrix respectively, v is the velocity of carriers, N is the density of acceptors or traps, and σ is the capture cross section. The first term represents radiative relaxation in the matrix, the second transport to and radiative relaxation in acceptor particles, and the third term nonradiative relaxation via traps. By normalizing to the total PL emission, we can look specifically at the radiative pathways. Figure 5.4b shows that 55% of the emission comes from acceptor particles in NC films prior to CdAc treatment. Cation/ligand exchange significantly increases the amount of recombination occurring in the acceptor particles, up to 82% of the total emission. Assuming that the capture cross section of acceptors does not change, the increase in emission from the acceptor particles must result from some combination of an increase in the radiative lifetime of NCs and increased carrier velocity after CdAc treatment.

We probed transient PL to better understand the underlying energy and charge transport mechanism responsible for the change in PL. Specifically, the transient nature of the emission from the acceptor can provide insight into the nature of electronic coupling to the surrounding donor NCs. Time resolved photoluminescence (TRPL) measurements of the acceptor emission reveal a rise in PL intensity during the first 300 ns (Figure 5.5); this is a signature of Förster resonant energy transfer (FRET) in NC assemblies⁴³⁻⁴⁵. To quantify the growth and decay of PL intensity, we fit the beginning of the TRPL traces with a biexponential containing one rising and one decaying term.

The characteristic rise time decreases from 62 ns to 15 ns following CdAc treatment; this indicates that the rate of exciton transfer is increased.

The point dipole FRET equation shown in equation 5.2 is commonly used to analyze FRET in NC assemblies and has shown success in interpreting the observed energy transfer.

$$k_{FRET} = \frac{1}{\tau_D} \left(\frac{R_o}{R} \right)^6 \quad \text{Eq. 5.2}$$

Where k_{FRET} is the energy transfer rate, τ_D is the donor lifetime, R_o is the Förster radius and R is the distance between the point dipoles. We note that the actual dependence of FRET on interparticle spacing in assemblies may deviate from the R^6 dependence of the standard expression. The Förster radius is influenced by the spectral overlap between donor emission and acceptor absorption. Although both emission and absorption spectra shift due to cation exchange, the shift is nearly the same, leading to only a 5% increase in spectral overlap after cation/ligand exchange (see Appendix D for details of the calculation). Based on the reduced interparticle spacing revealed by our GISAXS measurements (Figure 5.3b,c), the standard FRET model predicts a 4.8 fold increase in energy transfer rate following CdAc treatment; this prediction is consistent with the 4.1 fold increase in energy transfer rate found in TRPL measurements.

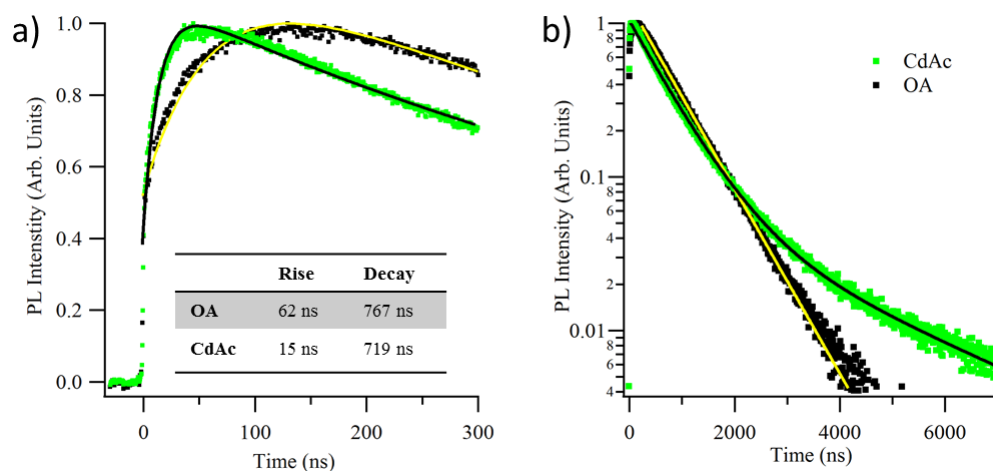


Figure 5.5: Time resolved photoluminescence of acceptors a) Acceptor particles exhibit a rising transient indicative of Förster resonant energy transfer. Inset: time constants for the rising and decaying component of a biexponential fit to the data. b) Full TRPL traces show single exponential decay before treatment, with an additional long lifetime ($\sim 3 \mu\text{s}$) after treatment

As the acceptor particles are surrounded by a matrix of higher band gap particles, exciton transport away from the acceptors should be significantly reduced. This enables direct observation of the effect of CdAc treatment on the lifetime of excitons in PbSe films independent of the increased energy transfer rates that may confound measurements of films composed of a single size of NCs, where FRET can occur even with a narrow size distribution⁴³. The transient emission of the untreated films are well fit by a single exponential decay with a time constant of 720 ns. After CdAc treatment, the initial decay remains the same but an additional long lifetime component appears with a lifetime of 2850 ns. The short lifetime component is typical of oleate passivated PbSe NCs measured in solution while the long lifetime component agrees with values measured for PbSe/CdSe core shell particles in solution^{32, 46}. The TRPL data therefore supports our assumption that transport away from acceptor NCs is significantly reduced and that these TRPL measurements represent the carrier dynamics in an isolated bright particle in the NC films.

The TRPL data merit further discussion on context of the steady state PL data shown in Figure 5.2. We note that the increased lifetime of CdAc acceptors is not sufficient to explain the ~ 3.5 fold increase in PL. The ~ 3 μs decay component only accounts for 7% of the PL decay. To describe this discrepancy, we emphasize that TRPL measurements only measure bright particles. Any dark particles (with trap states) will have an effect on the ensemble film measurements by increasing the non-radiative decay rate, but not on the TRPL measurements of isolated particles. For a single component film, equation 5.1 can be modified by removing the acceptor recombination term

$$\tau_{Film}^{-1} = \tau_{NC}^{-1} + vN_T\sigma_T \quad \text{Eq. 5.3}$$

Here τ_{Film} is obtained from Figure 5.2c, and τ_{NC} represents both radiative and nonradiative relaxation pathways in the bright NCs as measured in Figure 5.5b. The relationship in equation 3 therefore provides a convenient measure of the trap density due to dark particles under two assumptions. First, we interpret the 4.1 fold improvement in energy transfer rate as an indication of relative increase in exciton velocity due to CdAc treatment and secondly assume that the capture cross section is constant. Based on these assumptions, we find that CdAc treatment reduces the trap density by over an order of magnitude ($n_{OA}/n_{CdAc}=12$). We can therefore conclude that the CdAc treatment significantly improves the surface passivation of PbSe NCs. The combination of improved surface passivation and improved energy transfer rates make simultaneous cation and ligand exchange an attractive processing tool for optoelectronic applications. In particular, we believe LED applications may benefit from the increase in PL intensity combined with improved energy transfer rates.

5.5 Conclusions

We have shown that by exposing a PbSe NC thin film to an ethanolic solution of cadmium acetate both cation and ligand exchange occur on the surface of the NCs

simultaneously. This results in NC films that show increased PL as well as improved PL lifetime. The exchange from oleate to acetate ligands leads to reduced interparticle spacing and a corresponding 4.1 fold increase in Förster resonant energy transfer rate in NC films. Comparison of TRPL lifetime measurements of particles isolated in a higher bandgap matrix to single component films of the same particles indicates that the trap density is reduced by an order of magnitude following cation/ligand exchange. Based on observations of increased PLQY, increased PL lifetime, and increased energy transfer, we conclude that with a single processing step we have created a coupled artificial solid composed of heterostructured PbSe/CdSe NCs.

REFERENCES

1. Treml, B.; Yang, J.; Wise, F.; Hanrath, T. *Chem. Phys.* **2015**.
2. Sun, Q.; Wang, Y. A.; Li, L. S.; Wang, D.; Zhu, T.; Xu, J.; Yang, C.; Li, Y. *Nat Photon* **2007**, 1, 717-722.
3. Nozik, A. J.; Beard, M. C.; Luther, J. M.; Law, M.; Ellingson, R. J.; Johnson, J. C. *Chem. Rev.* **2010**, 110, 6873-6890.
4. Ibáñez, M.; Zamani, R.; Gorsse, S.; Fan, J.; Ortega, S.; Cadavid, D.; Morante, J. R.; Arbiol, J.; Cabot, A. *ACS nano* **2013**, 7, 2573-2586.
5. Talapin, D. V.; Murray, C. B. *Science* **2005**, 310, 86-89.
6. Thon, S. M.; Ip, A. H.; Voznyy, O.; Levina, L.; Kemp, K. W.; Carey, G. H.; Masala, S.; Sargent, E. H. **2013**.
7. Kim, D.; Kim, D.-H.; Lee, J.-H.; Grossman, J. C. *Phys. Rev. Lett.* **2013**, 110, 196802.
8. Reiss, P.; Protière, M.; Li, L. *Small* **2009**, 5, 154-168.
9. Piryatinski, A.; Ivanov, S. A.; Tretiak, S.; Klimov, V. I. *Nano Lett.* **2007**, 7, 108-115.
10. Nizamoglu, S.; Ozel, T.; Sari, E.; Demir, H. V. *Nanotechnology* **2007**, 18, 065709.
11. Bruchez, M.; Moronne, M.; Gin, P.; Weiss, S.; Alivisatos, A. P. *Science* **1998**, 281, 2013-2016.
12. Medintz, I. L.; Uyeda, H. T.; Goldman, E. R.; Mattoussi, H. *Nat Mater* **2005**, 4, 435-446.
13. Hines, M. A.; Guyot-Sionnest, P. *The Journal of Physical Chemistry* **1996**, 100, 468-471.
14. Neo, M. S.; Venkatram, N.; Li, G. S.; Chin, W. S.; Ji, W. *The Journal of Physical Chemistry C* **2010**, 114, 18037-18044.
15. Pietryga, J. M.; Werder, D. J.; Williams, D. J.; Casson, J. L.; Schaller, R. D.; Klimov, V. I.; Hollingsworth, J. A. *J. Am. Chem. Soc.* **2008**, 130, 4879-4885.
16. Xie, R.; Kolb, U.; Li, J.; Basché, T.; Mews, A. *J. Am. Chem. Soc.* **2005**, 127, 7480-7488.
17. Bae, W. K.; Char, K.; Hur, H.; Lee, S. *Chem. Mater.* **2008**, 20, 531-539.
18. Cirloganu, C. M.; Padilha, L. A.; Lin, Q.; Makarov, N. S.; Velizhanin, K. A.; Luo, H.; Robel, I.; Pietryga, J. M.; Klimov, V. I. *Nat Commun* **2014**, 5.
19. Cunningham, P. D.; Boercker, J. E.; Foos, E. E.; Lumb, M. P.; Smith, A. R.; Tischler, J. G.; Melinger, J. S. *Nano Lett.* **2011**, 11, 3476-3481.
20. Neo, D. C. J.; Cheng, C.; Stranks, S. D.; Fairclough, S. M.; Kim, J. S.; Kirkland, A. I.; Smith, J. M.; Snaith, H. J.; Assender, H. E.; Watt, A. A. R. *Chem. Mater.* **2014**, 26, 4004-4013.
21. Speirs, M.; Balazs, D.; Fang, H.-H.; Lai, L.-H.; Protesescu, L.; Kovalenko, M.; Loi, M. *Journal of Materials Chemistry A* **2015**, 3, 1450-1457.
22. Supran, G. J.; Song, K. W.; Hwang, G. W.; Correa, R. E.; Scherer, J.; Dauler, E. A.; Shirasaki, Y.; Bawendi, M. G.; Bulović, V. *Adv. Mater.* **2015**, n/a-n/a.
23. Sanchez, R. S.; Binetti, E.; Torre, J. A.; Garcia-Belmonte, G.; Striccoli, M.; Mora-Sero, I. *Nanoscale* **2014**, 6, 8551-8555.

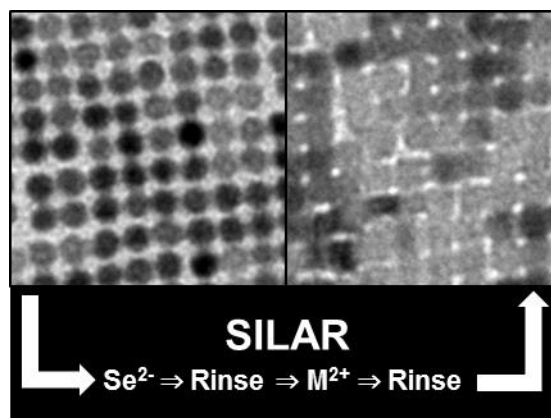
24. Tang, J.; Kemp, K. W.; Hoogland, S.; Jeong, K. S.; Liu, H.; Levina, L.; Furukawa, M.; Wang, X.; Debnath, R.; Cha, D.; Chou, K. W.; Fischer, A.; Amassian, A.; Asbury, J. B.; Sargent, E. H. *Nat Mater* **2011**, 10, 765-771.
25. Kovalenko, M. V.; Scheele, M.; Talapin, D. V. *Science* **2009**, 324, 1417-20.
26. Ning, Z.; Ren, Y.; Hoogland, S.; Voznyy, O.; Levina, L.; Stadler, P.; Lan, X.; Zhitomirsky, D.; Sargent, E. H. *Adv. Mater.* **2012**, 24, 6295-6299.
27. Oh, S. J.; Berry, N. E.; Choi, J.-H.; Gauding, E. A.; Lin, H.; Paik, T.; Diroll, B. T.; Muramoto, S.; Murray, C. B.; Kagan, C. R. *Nano Letters* **2014**, 14, 1559-1566.
28. Liu, Y.; Tolentino, J.; Gibbs, M.; Ihly, R.; Perkins, C. L.; Liu, Y.; Crawford, N.; Hemminger, J. C.; Law, M. *Nano Lett.* **2013**, 13, 1578-1587.
29. ten Cate, S.; Liu, Y.; Suchand Sandeep, C. S.; Kinge, S.; Houtepen, A. J.; Savenije, T. J.; Schins, J. M.; Law, M.; Siebbeles, L. D. A. *The Journal of Physical Chemistry Letters* **2013**, 4, 1766-1770.
30. Lambert, K.; Geyter, B. D.; Moreels, I.; Hens, Z. *Chem. Mater.* **2009**, 21, 778-780.
31. Casavola, M.; van Huis, M. A.; Bals, S.; Lambert, K.; Hens, Z.; Vanmaekelbergh, D. *Chem. Mater.* **2012**, 24, 294-302.
32. De Geyter, B.; Justo, Y.; Moreels, I.; Lambert, K.; Smet, P. F.; Van Thourhout, D.; Houtepen, A. J.; Grodzinska, D.; de Mello Donega, C.; Meijerink, A.; Vanmaekelbergh, D.; Hens, Z. *ACS Nano* **2010**, 5, 58-66.
33. Moreels, I.; Lambert, K.; De Muynck, D.; Vanhaecke, F.; Poelman, D.; Martins, J. C.; Allan, G.; Hens, Z. *Chem. Mater.* **2007**, 19, 6101-6106.
34. De Geyter, B.; Hens, Z. *Appl. Phys. Lett.* **2010**, 97, -.
35. Justo, Y.; Geiregat, P.; Hoecke, K. V.; Vanhaecke, F.; De Mello Donega, C.; Hens, Z. *The Journal of Physical Chemistry C* **2013**, 117, 20171-20177.
36. Dai, Q.; Wang, Y.; Li, X.; Zhang, Y.; Pellegrino, D. J.; Zhao, M.; Zou, B.; Seo, J.; Wang, Y.; Yu, W. W. *ACS Nano* **2009**, 3, 1518-1524.
37. Moreels, I.; Fritzing, B.; Martins, J. C.; Hens, Z. *J. Am. Chem. Soc.* **2008**, 130, 15081-15086.
38. Abel, K. A.; Qiao, H.; Young, J. F.; van Veggel, F. C. J. M. *The Journal of Physical Chemistry Letters* **2010**, 1, 2334-2338.
39. Anderson, N. C.; Hendricks, M. P.; Choi, J. J.; Owen, J. S. *J. Am. Chem. Soc.* **2013**, 135, 18536-18548.
40. Zarghami, M. H.; Liu, Y.; Gibbs, M.; Gebremichael, E.; Webster, C.; Law, M. *ACS Nano* **2010**, 4, 2475-2485.
41. Zhitomirsky, D.; Voznyy, O.; Hoogland, S.; Sargent, E. H. *ACS Nano* **2013**, 7, 5282-5290.
42. Jasieniak, J.; Califano, M.; Watkins, S. E. *ACS Nano* **2011**, 5, 5888-5902.
43. Kagan, C. R.; Murray, C. B.; Bawendi, M. G. *Physical Review B* **1996**, 54, 8633-8643.
44. Kagan, C. R.; Murray, C. B.; Nirmal, M.; Bawendi, M. G. *Phys. Rev. Lett.* **1996**, 76, 1517-1520.
45. Clark, S. W.; Harbold, J. M.; Wise, F. W. *The Journal of Physical Chemistry C* **2007**, 111, 7302-7305.

46. Kigel, A.; Brumer, M.; Maikov, G.; Sashchiuk, A.; Lifshitz, E. *Superlattices Microstruct.* **2009**, 46, 272-276.

CHAPTER 6

SUCCESSIVE IONIC LAYER ABSORPTION AND REACTION FOR POST- ASSEMBLY CONTROL OVER INORGANIC BONDS IN LONG RANGE ORDERED NANOCRYSTAL FILMS

Long-range ordered, epitaxially connected, films of nanocrystals (NCs) are a self-assembled nanomaterial where quantum confinement is intermediate between that of a quantum dot and a quantum well. While a host of collective properties have been predicted for these assemblies, state of the art films are currently limited by paracrystalline disorder and incomplete formation of the epitaxial bonds during the oriented attachment growth process. In this work, we use successive ionic layer absorption and reaction (SILAR) to enlarge the NCs after assembly. SILAR growth leads to both formation of new inorganic bonds and thickening of the bonds already present in the film. As a result, electronic coupling the films is enhanced, as evidenced by increased conductance and hole mobility and a large redshift in the excitonic absorption peak following SILAR growth. The post assembly film growth detailed here presents an opportunity for repairing defects and precisely tailoring the degree of quantum confinement in these nanomaterials.



6.1 Introduction

The properties of a material can broadly be attributed to the interplay of the energy levels of the constituent atoms, the structural organization of the building blocks, and the nature of the interatomic bonding. Progress in colloidal synthesis has provided a vast library of high-quality nanocrystal (NC) “artificial atoms” with tunable properties and energy levels¹⁻³. Recent detailed investigations into the interparticle interactions that govern self-assembly has similarly expanded our understanding of processing-structure relationships in NC films to the degree that we can now produce single crystal superlattices of NCs with grain sizes over 20 μm as well as co-crystallize multiple NC components into binary and ternary assemblies⁴⁻⁷. For optoelectronic applications that seek to exploit the novel properties of semiconducting NC films, the insulating native ligands pose a critical problem, and must generally be eliminated to generate the strong electronic coupling among NCs required for carrier transport. However, ligand exchange or thermal annealing frequently lead to disordered NC films that are then limited by hopping transport⁸⁻¹³.

Recently, there have been reports of long range ordered NC assemblies formed through controlled ligand removal followed by oriented attachment¹⁴⁻¹⁶. These treatments produce epitaxial bonds between the “artificial atoms” and provide an intriguing opportunity to achieve both long range order and strong electronic coupling in a single NC assembly. Tight binding calculations of these “confined-but-connected” (CBC) films predict collective properties such as Dirac cones, topological states, and minibands^{17, 18}. However, these properties have yet to be experimentally realized. Both theoretical and experimental studies of these highly coupled systems have indicated that one of the barriers to realizing carrier delocalization in epitaxially connected, long range ordered quantum dot films is missing “bonds” that appear stochastically during the assembly and fusion process^{19, 20}. THz conductivity measurements, which probe the

transport properties at length scale that ignore broken bonds, observe electron mobilities of up to $150 \text{ cm}^2/\text{Vs}$ ²⁰. However, as the length scale of measurements is increased to $\sim 500 \text{ nm}$ and $\sim 100 \text{ }\mu\text{m}$, the measured mobility is reduced to $13 \text{ cm}^2/\text{Vs}$ and $.2 \text{ cm}^2/\text{Vs}$ as broken bonds and grain boundaries lead to increased carrier scattering.

In order to address this limiting factor, we seek to grow the NC's after the assembly and oriented attachment process, connecting NCs that did not previously have an epitaxial bond between them while also enlarging bonds between already connected NCs in order to enhance electronic coupling¹⁸. Our proposed process, sequential ionic layer absorption and reaction (SILAR), is illustrated in Figure 6.1. Low temperature, solution processing techniques are used in order to avoid ripening of the labile PbSe system^{21, 22}. SILAR has been used previously as a ligand removal procedure to tune the majority carrier type in PbSe solids, as well as to reduce carrier scattering in all inorganic NC assemblies^{23, 24}.

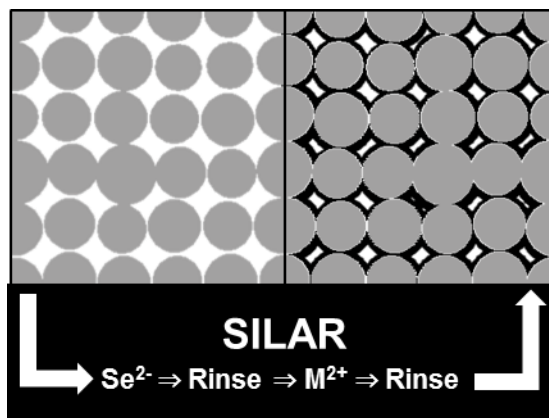


Figure 6.1: Post assembly growth of the epitaxially connected PbSe film through successive ionic layer absorption and reaction (SILAR). The process creates and strengthens inorganic bonds in the assembly.

In this work, we show that we can increase the fraction of formed bonds from 82% to 91% while also increasing the width of the inorganic bonds from 3.1 to 4.0 nm. Growth of a PbSe SILAR shell onto the CBC leads to increased electronic coupling, as

evidenced by a redshift in the excitonic peak and a systematic increase in hole mobility with increasing SILAR growth. Collectively, our structural, optical, and electronic characterization indicates that the strength of the electronic coupling between NCs in a CBC can be tuned through control of the inorganic bonds among the NCs without sacrificing the long range order of the NC assembly. We hope that the insights into structure-property relationships in CBCs explored in this work will aid future efforts to realize the novel collective properties of these nanomaterials.

The films presented in this study were fabricated following a two-step assembly and fusion process in order to produce NC films with both long range orientational and translational order. First, a monolayer of NCs was assembled in a close packed hexagonal monolayer on an ethylene glycol subphase following established procedures^{5, 25}. We triggered ligand removal and oriented attachment of the dry NC films through addition of ethylene diamine (EDA) to the subphase. EDA has been shown to preferentially remove ligands from the {100} facets of PbSe nanocrystals and promote oriented attachment²⁶⁻²⁹. By applying this chemical treatment to a monolayer of nanocrystals on a liquid interface, the particles retain enough mobility to coherently shift from the hexagonal close packed arrangement shown in Figure 6.2a to a square symmetry with a coherent NC orientation shown in Figure 6.2b while retaining long range order. Consistent with previous reports, we observed that a number of potential bridges between NCs did not form^{19, 20}.

6.2 Effect of SILAR on CBC Structure and Optical Properties

After transferring a sample to a substrate or TEM grid via Langmuir-Schafer method, NC films underwent a successive ionic layer absorption and reaction (SILAR) process. Films were dipped in ethanolic solutions of Na₂Se and M-acetate (M=Pb,Cd) with a rinse in pure ethanol between the ionic absorption and reaction steps. We

consider exposure to both the anion and cation to constitute one SILAR cycle. In contrast to ALD, which uses self-limiting reactions to produce precisely programmable film thicknesses, SILAR deposition of semiconducting thin films typically show growth rates below an atomic bond length per cycle. The growth rates also can change during SILAR growth. These results indicate that SILAR growth is a less precisely controlled film growth method³⁰. Figures 6.2c-f, showing films that have undergone 2 (Fig 2c,d) and 4 (Fig. 2e,f) SILAR cycles clearly show that SILAR leads to NC growth resulting in both the formation of new inorganic bonds as well as enlarging bonds formed during the assembly process.

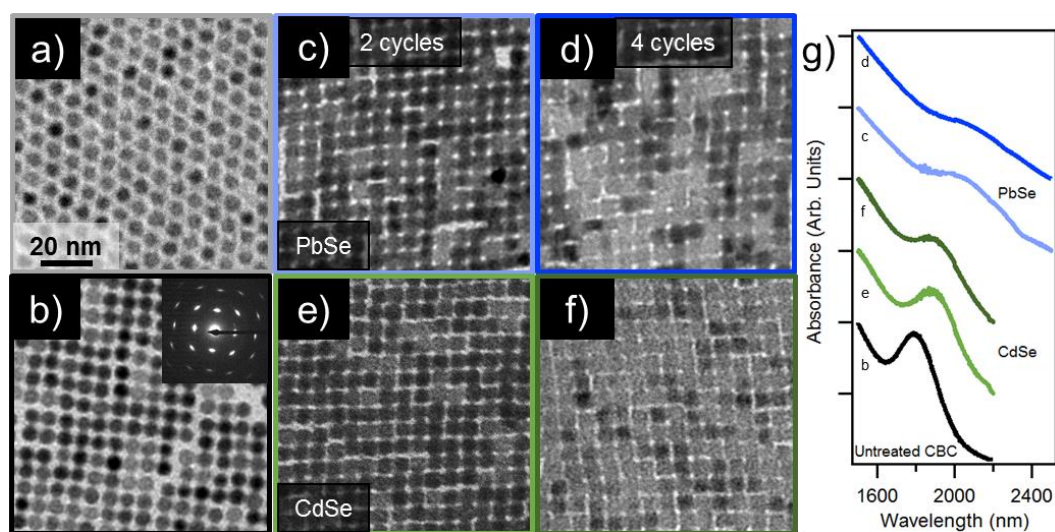


Figure 6.2: a) Monolayer of particles before ligand removal. b) As made CBC film showing epitaxial connections as well as unformed bonds. Inset: Selected area electron diffraction pattern showing coherent NC orientation across a CBC. The aperture selected a 750nm diameter region of film. c,d) CBCs after 2 and 4 cycles of PbSe SILAR respectively. e,f) CBCs after 2 and 4 cycles of CdSe SILAR respectively. g) Absorption spectra of CBC films provide insight into the effect of homo and hetero shell growth on quantum confinement. All TEM images share the same scale.

The composition of the new shell material is critically important to the resulting optical properties of the CBC films. Growth of PbSe onto PbSe NCs leads to significant redshift of the excitonic peak in the UV-vis absorption shown in Fig 6.2g, which we

interpret as decreased quantum confinement in the NC films. Due to the outward growth of the seed NCs, the film transitions continuously between the initial structure and a 2D PbSe quantum well, and this change is also observed in the absorption, which displays a broad excitonic peak typical of PbX (X=Se,S) nanosheets^{31,32}.

In order to investigate if post assembly SILAR growth could be used to form long range ordered heterostructures, we also studied growth of a CdSe shell onto the CBCs. CdX is a common shell material for PbX quantum dots that passivates surface states and has led to increased performance in both LED and PV devices³³⁻³⁵. The conventional method of producing a CdSe shell is through controlled cation exchange that consumes the original PbSe nanostructure³⁶. Instead, we grew a SILAR CdSe shell outwards. In the low resolution TEM images in Figure 6.2, we see no obvious structural differences between particles enlarged via homo (PbSe) or hetero (CdSe) shell growth. However, absorption curves for CdSe shell growth (Figure 6.2g) show that the excitonic peak does not shift as much as for PbSe growth and is only slightly broadened (FWHM of 202 nm and 220 nm for 0 and 4 cycles respectively). In PbSe/CdSe core shell particles synthesized and measured in solution, the location of the excitonic peak is completely determined by the size of the PbSe core, indicating minimal wavefunction leak into the CdSe shell³⁷. We believe that the limited redshift observed for the CdSe films may be due to an increase in the local dielectric constant of the film following SILAR growth³⁸.

6.3 Quantification of Structural Changes

Low resolution TEM indicates that post assembly SILAR modifies the structure of CBC films. In order to examine these morphological changes in more detail, we used cross correlated high angle annular dark field (HAADF) scanning transmission electron microscopy (STEM). Atomic resolution images (Figure 6.3a and 6.3b) provide

additional insight into the effect of shell formation on the CBC structure and enable quantification of the qualitative trends seen in Figure 6.2. From automated particle analysis of wide field of view images (Figure E.2 in Appendix E), we see an initial average particle size of 6.2 ± 0.3 nm with 82% of possible bonds formed and an average bond width of 3.1 ± 0.5 nm. After two cycles of CdSe SILAR, the particle diameter increased to 6.7 ± 0.4 nm with 91% of bonds formed and a bond width of 4.0 ± 0.6 nm. Particle size and bridge width statistics were determined by fitting the histograms in Figure 6.3e and 6.3f with a Gaussian function. Notably, as shown in Figure 6.3c and 6.3d, the as formed CBC had approximately equal fractions of particles with either 3 or 4 bonds formed whereas after 2 cycles of SILAR about 70% of particles have made inorganic bonds with all of their nearest neighbors.

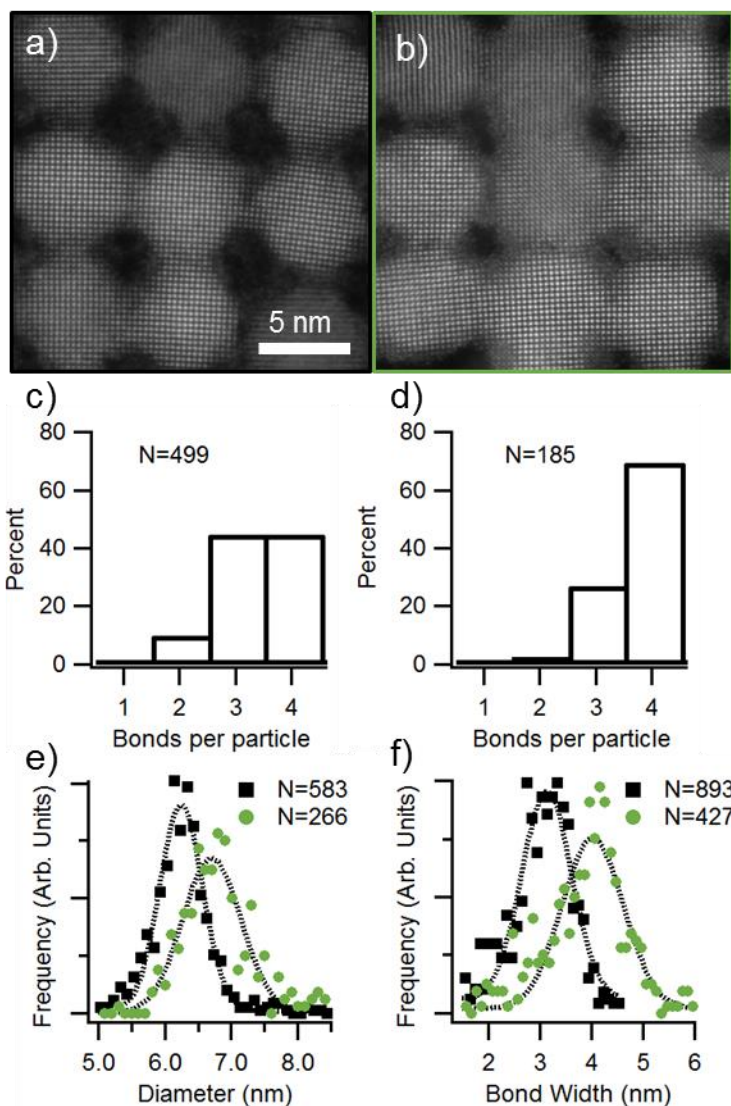


Figure 6.3: a,b) HAADF STEM images of CBCs before and after 2 cycles of CdSe SILAR respectively. The images are at the same scale. c,d) Histogram of the number of bonds per particle obtained from wide field of view images. 25% more particles have made all possible bonds following SILAR treatment. e) Particle size distribution before (black) and after (green) SILAR treatment. f) Bond width distribution before (black) and after (green) SILAR treatment. Dotted lines represent Gaussian fits to the data. The values are scaled such that the total area under each distribution is equal.

In addition to quantifying of the changes in particle and bond size after SILAR treatment, cross correlated HAADF STEM allows us to look in detail at the SILAR shells grown on individual particles. Consistent with the selected area electron diffraction pattern inset in Figure 6.2b, we see the atomic columns of the rock salt

structure oriented along the $\langle 100 \rangle$ zone axis. In contrast to the crystalline cores, the shell appears to be amorphous. The difference in contrast between the PbSe core and the shell indicates that the shell is composed of a lower Z material. As this sample has undergone CdSe SILAR, we believe the difference in contrast indicates that the amorphous shell is a Cd rich SILAR layer. We confirm this interpretation via electron energy loss spectroscopy (EELS) mapping shown in Figure 6.4. At each pixel shown, a full EELS spectrum was acquired with an energy dispersion of 0.25 eV and a zero-loss FWHM of ~ 0.8 eV. Background fitting and subtraction was performed using the linear combination of power laws method and oversampling with $\sigma=2$ pixels³⁹; and the relative Cd concentration was extracted by integrating the background subtracted spectra over the Cd-M_{4,5} edge. The resultant Cd map tracks the amorphous, lower contrast shells, indicating increased Cd content. Representative spectra, both on and off the particle shells, are in Figure E.4 in Appendix E.

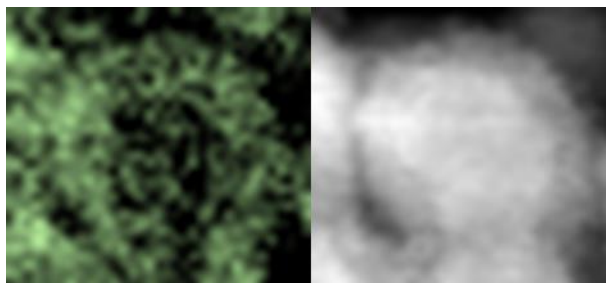


Figure 6.4: EELS mapping after SILAR. a) EELS map of the Cd-M_{4,5} edge across a NC in a CBC b) Simultaneously acquired HAADF STEM image showing Z contrast that correlates with the Cd signal.

6.4 Effect of SILAR on Transport Properties

Having shown via detailed structural analysis, at multiple length scales, that SILAR grows a shell around CBCs leading to increased particle size, bond width, and particle connectivity, we now proceed to study the effect of this treatment on the electrical properties of CBCs. Electrical characterization was carried out on a FET

device with a channel 7 μm long and 7 mm wide with a 200 nm SiO_2 gate oxide and a heavily doped Si wafer as the gate. The field effect mobility is determined from the slope of the transfer curves according to equation 6.1.

$$\frac{dI_D}{dV_G} = \frac{W}{L} C_{ox} \mu V_{SD} \quad \text{Eq. 6.1}$$

where I_D is the current measured at the drain electrode, V_G is the applied gate voltage, W is the channel width, L is the channel length, V_{SD} is the applied source drain voltage, and μ is the field effect mobility. Transfer curves and mobilities were determined at $V_{SD}=1$. Similarly, conductance was determined from the slope of the I_{sd} vs V_{sd} measurements at $V_g=0$.

CBCs made following the procedure detailed above are initially n-type as seen in Figure 6.5a. Following the first cycle of SILAR we observe a change to p-type transport as well as a large increase in conductance and carrier mobility during the first SILAR cycle. It is well established that NC stoichiometry is critically important to both the density of states in a NC as well as majority carrier type and concentration^{40, 41}. We attribute the observed high p-type doping to the addition of Se ions that are not fully passivated during the subsequent cation half cycle, this behavior is consistent with previous reports investigating Na_2S and Na_2Se for ligand exchange^{23, 42}. As a result of this doping, the states being probed through modulation of the gate voltage after SILAR treatment are not necessarily the same states probed in the initial, untreated film.

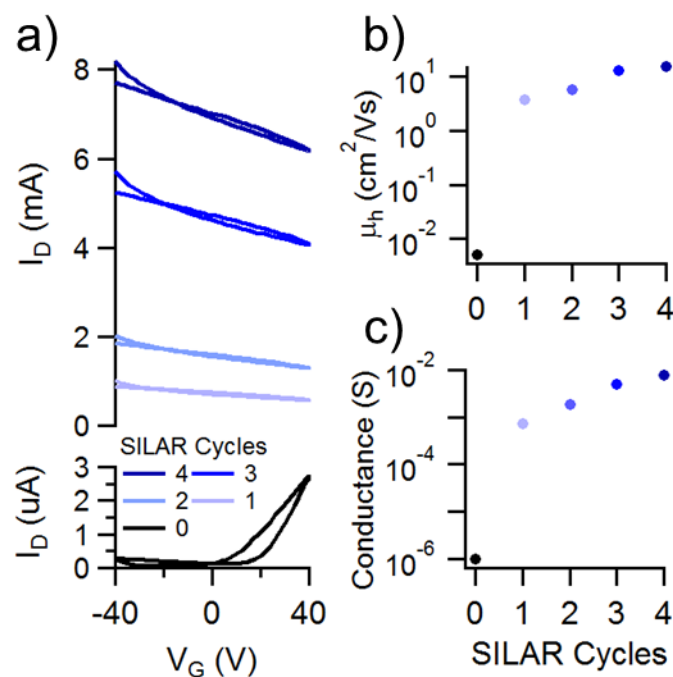


Figure 6.5: Transport during PbSe SILAR growth a) Transfer curves as the number of SILAR cycles are increased. Due to the low current before SILAR treatment, these data are shown on a magnified scale. b,c) The mobility and conductance of the CBC film respectively, during 4 cycles of SILAR.

Following the first SILAR cycle, CBC films continue to display consistent p-type behavior. We see a gradual and consistent increase in both the mobility of carriers, Figure 6.5b, as well as the conductance of the PbSe film, Figure 6.5c, as the film undergoes more SILAR cycles. We attribute the increase in hole mobility and film conductance to the effect of the formation and strengthening of the inorganic bonds during SILAR film growth on the CBC film. Recent calculations by Chen *et al* have suggested that films of epitaxially connected NCs with high carrier concentrations may undergo an insulator to metal transition⁴³. The temperature dependent transport measurements required to investigate this transition in SILAR treated CBCs are certainly of interest, but are beyond the scope of this work.

6.5 Conclusions

We have shown, through detailed microscopic characterization, that post-assembly growth of long range ordered, epitaxially connected NC films can improve the connections between NCs. The fraction of bonds formed increased from 82% to 91% while also increasing the width of the inorganic bonds from 3.1 to 4.0 nm following two cycles of SILAR. Absorption spectra indicate that the effect of post-assembly growth on the quantum confinement in this system is dependent on the composition of the SILAR shell material. As a homogenous SILAR shell is grown on an epitaxially connected NC film, both the conductance and hole mobility increase with increasing shell growth, indicating that building and strengthening the inorganic bonds leads to improved electronic coupling in this system. This work presents a route towards addressing the issue of unformed epitaxial bonds in long range ordered NC films and may aid in the realization of the exciting collective properties predicted for these nanomaterials.

REFERENCES

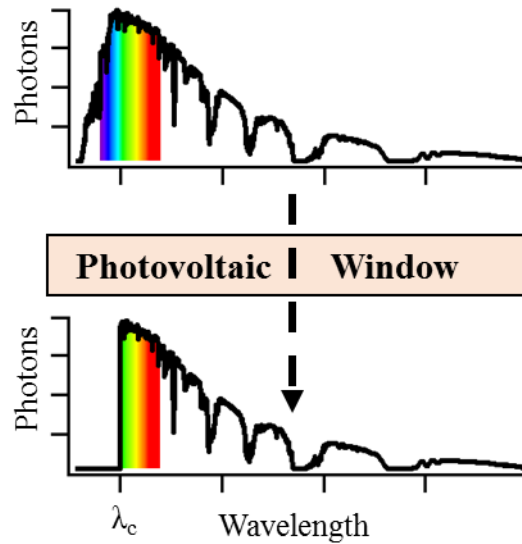
1. Kwon, S. G.; Hyeon, T. *Acc. Chem. Res.* **2008**, 41, 1696-1709.
2. Talapin, D.; Lee, J.; Kovalenko, M. *Chemical* **2010**.
3. Rossetti, R.; Hull, R.; Gibson, J. M.; Brus, L. E. *The Journal of Chemical Physics* **1985**, 82, 552.
4. Li, R.; Bian, K.; Wang, Y.; Xu, H.; Hollingsworth, J. A.; Hanrath, T.; Fang, J.; Wang, Z. *Nano Lett.* **2015**, 15, 6254-6260.
5. Dong, A.; Ye, X.; Chen, J.; Murray, C. *Nano Lett.* **2011**.
6. Dong, A.; Chen, J.; Vora, P. M.; Kikkawa, J. M.; Murray, C. B. *Nature* **2010**, 466, 474-477.
7. Shevchenko, E. V.; Talapin, D. V.; Kotov, N. A.; O'Brien, S.; Murray, C. B. *Nature* **2006**, 439, 55-59.
8. Yang, J.; Wise, F. W. *The Journal of Physical Chemistry C* **2015**, 119, 3338-3347.
9. Baik, S. J.; Kim, K.; Lim, K. S.; Jung, S.; Park, Y. C.; Han, D. G.; Lim, S.; Yoo, S.; Jeong, S. *Journal of Physical Chemistry C* **2011**, 115, 607-612.
10. Tang, J.; Kemp, K. W.; Hoogland, S.; Jeong, K. S.; Liu, H.; Levina, L.; Furukawa, M.; Wang, X.; Debnath, R.; Cha, D.; Chou, K. W.; Fischer, A.; Amassian, A.; Asbury, J. B.; Sargent, E. H. *Nat Mater* **2011**, 10, 765-771.
11. Liu, Y.; Gibbs, M.; Puthussery, J.; Gaik, S.; Ihly, R.; Hillhouse, H. W.; Law, M. *Nano Lett.* **2010**, 10, 1960-1969.
12. Wills, A. W.; Kang, M. S.; Khare, A.; Gladfelter, W. L.; Norris, D. J. *ACS Nano* **2010**, 4, 4523-4530.
13. Kovalenko, M. V.; Scheele, M.; Talapin, D. V. *Science* **2009**, 324, 1417-20.
14. Baumgardner, W. J.; Whitham, K.; Hanrath, T. *Nano Lett.* **2013**, 13, 3225-3231.
15. Evers, W. H.; Goris, B.; Bals, S.; Casavola, M.; de Graaf, J.; Roij, R. v.; Dijkstra, M.; Vanmaekelbergh, D. *Nano Lett.* **2012**, 13, 2317-2323.
16. Boneschanscher, M. P.; Evers, W. H.; Geuchies, J. J.; Altantzis, T.; Goris, B.; Rabouw, F. T.; van Rossum, S. A. P.; van der Zant, H. S. J.; Siebbeles, L. D. A.; Van Tendeloo, G.; Swart, I.; Hilhorst, J.; Petukhov, A. V.; Bals, S.; Vanmaekelbergh, D. *Science* **2014**, 344, 1377-1380.
17. Kalesaki, E.; Delerue, C.; Morais Smith, C.; Beugeling, W.; Allan, G.; Vanmaekelbergh, D. *Physical Review X* **2014**, 4, 011010.
18. Kalesaki, E.; Evers, W.; Allan, G.; Vanmaekelbergh, D.; Delerue, C. *Physical Review B* **2013**, 88, 115431.
19. Whitham, K.; Yang, J.; Savitzky, B. H.; Kourkoutis, L. F.; Wise, F.; Hanrath, T. *Nature materials* **2016**.
20. Evers, W. H.; Schins, J. M.; Aerts, M.; Kulkarni, A.; Capiod, P.; Berthe, M.; Grandidier, B.; Delerue, C.; van der Zant, H. S.; van Overbeek, C. *Nature Communications* **2015**, 6.
21. Goodfellow, B. W.; Patel, R. N.; Panthani, M. G.; Smilgies, D.; Korgel, B. A. *The Journal of Physical Chemistry C* **2011**, 115, 6397-6404.
22. van Huis, M. A.; Kunneman, L. T.; Overgaag, K.; Xu, Q.; Pandraud, G.; Zandbergen, H. W.; Vanmaekelbergh, D. *Nano Lett.* **2008**, 8, 3959-3963.

23. Oh, S. J.; Berry, N. E.; Choi, J.-H.; Gaulding, E. A.; Lin, H.; Paik, T.; Diroll, B. T.; Muramoto, S.; Murray, C. B.; Kagan, C. R. *Nano Lett.* **2014**.
24. Moroz, P.; Kholmicheva, N.; Mellott, B.; Liyanage, G.; Rijal, U.; Bastola, E.; Huband, K.; Khon, E.; McBride, K.; Zamkov, M. *ACS nano* **2013**, *7*, 6964-6977.
25. Dong, A.; Jiao, Y.; Milliron, D. J. *ACS Nano* **2013**, *7*, 10978-10984.
26. Law, M.; Luther, J.; Song, Q.; Hughes, B. *Journal of the* **2008**.
27. Kitada, S.; Kikuchi, E.; Ohno, A.; Aramaki, S.; Maenosono, S. *Solid State Commun.* **2009**, *149*, 1853-1855.
28. Anderson, N. C.; Hendricks, M. P.; Choi, J. J.; Owen, J. S. *J. Am. Chem. Soc.* **2013**, *135*, 18536-18548.
29. Sandeep, C. S.; Azpiroz, J. M.; Evers, W. H.; Boehme, S. C.; Moreels, I.; Kinge, S.; Siebbeles, L. D.; Infante, I.; Houtepen, A. J. *ACS nano* **2014**, *8*, 11499-11511.
30. Pathan, H.; Lokhande, C. *Bull. Mater. Sci.* **2004**, *27*, 85-111.
31. Bhandari, G. B.; Subedi, K.; He, Y.; Jiang, Z.; Leopold, M.; Reilly, N.; Lu, H. P.; Zayak, A. T.; Sun, L. *Chem. Mater.* **2014**, *26*, 5433-5436.
32. Aerts, M.; Bielewicz, T.; Klinke, C.; Grozema, F. C.; Houtepen, A. J.; Schins, J. M.; Siebbeles, L. D. *Nature communications* **2014**, *5*.
33. Neo, D. C. J.; Cheng, C.; Stranks, S. D.; Fairclough, S. M.; Kim, J. S.; Kirkland, A. I.; Smith, J. M.; Snaith, H. J.; Assender, H. E.; Watt, A. A. R. *Chem. Mater.* **2014**, *26*, 4004-4013.
34. Speirs, M.; Balazs, D.; Fang, H.-H.; Lai, L.-H.; Protesescu, L.; Kovalenko, M.; Loi, M. *Journal of Materials Chemistry A* **2015**, *3*, 1450-1457.
35. Supran, G. J.; Song, K. W.; Hwang, G. W.; Correa, R. E.; Scherer, J.; Dauler, E. A.; Shirasaki, Y.; Bawendi, M. G.; Bulović, V. *Adv. Mater.* **2015**, n/a-n/a.
36. Pietryga, J. M.; Werder, D. J.; Williams, D. J.; Casson, J. L.; Schaller, R. D.; Klimov, V. I.; Hollingsworth, J. A. *J. Am. Chem. Soc.* **2008**, *130*, 4879-4885.
37. De Geyter, B.; Hens, Z. *Appl. Phys. Lett.* **2010**, *97*, -.
38. Wolcott, A.; Doyeux, V.; Nelson, C. A.; Gearba, R.; Lei, K. W.; Yager, K. G.; Dolocan, A. D.; Williams, K.; Nguyen, D.; Zhu, X. Y. *The Journal of Physical Chemistry Letters* **2011**, *2*, 795-800.
39. Cueva, P.; Hovden, R.; Mundy, J. A.; Xin, H. L.; Muller, D. A. *Microsc. Microanal.* **2012**, *18*, 667-675.
40. Oh, S. J.; Berry, N. E.; Choi, J.-H.; Gaulding, E. A.; Paik, T.; Hong, S.-H.; Murray, C. B.; Kagan, C. R. *ACS nano* **2013**, *7*, 2413-2421.
41. Kim, D.; Kim, D.-H.; Lee, J.-H.; Grossman, J. C. *Phys. Rev. Lett.* **2013**, *110*, 196802.
42. Liu, Y.; Tolentino, J.; Gibbs, M.; Ihly, R.; Perkins, C. L.; Liu, Y.; Crawford, N.; Hemminger, J. C.; Law, M. *Nano Lett.* **2013**, *13*, 1578-1587.
43. Chen, T.; Reich, K. V.; Kramer, N. J.; Fu, H.; Kortshagen, U. R.; Shklovskii, B. I. *Nat Mater* **2016**, *15*, 299-303.

CHAPTER 7

**A QUANTITATIVE FRAMEWORK FOR EVALUATING
SEMITRANSSPARENT PHOTOVOLTAIC WINDOWS**

The recent surge of interest in photovoltaic (PV) technologies has led to impressive advances in PV technologies which have opened up new application spaces that were previously technologically infeasible or economically impractical for conventional crystalline Si PV. These new applications often have different requirements or restrictions that may change the critical metric used to evaluate the performance of solar cells from pure efficiency to more nuanced metrics. Optimizing the balance between power generation and natural lighting is especially important for building-integrated semitransparent PV. We present a quantitative performance evaluation framework for semitransparent photovoltaic (stPV) windows that balances the power generated by the photovoltaic absorber with the opportunity cost of lost natural lighting. We show how panchromatic natural sunlight can be allocated with spectral selectivity for the dual functionality of power generation and lighting. Using this framework, we determine that an ideal (i.e., Shockley-Queisser) spectrally selective stPV window with an optimal bandgap (2.5 eV) could produce up to 12.5 mW/cm² of power with the loss of only 6.3% of the illumination provided by the window. We hope that this framework will be used to evaluate and guide future research in stPV for building integrated applications.



7.1 Introduction

The growing focus on renewable energy technologies, in particular solar photovoltaics (PV), has led to a profound increase in PV manufacturing and installation. Concurrent with the remarkable advances in deployment of conventional PV, scientific discoveries and innovations have created an immensely fertile opportunity space for next-generation solar energy PV technologies^{1, 2}, including semi-transparent solar cells.³⁻⁹

Since stPV technologies provide the dual functionality of (i) a window (to provide lighting) and (ii) a solar cell (to provide power), their performance needs to be evaluated in a framework that fairly accounts for both functions. Whereas performance metrics for conventional PV technologies have been well established¹⁰, these metrics alone are inadequate in the case of stPV since they do not capture the value of partial transparency for lighting purposes. Future advances in stPV technologies would therefore benefit from the guidance of an analytical performance metric to evaluate the utilization of broadband solar radiation for this dual purpose.

The analytical model presented in this communication provides a quantitative framework for evaluating stPV windows by explicitly accounting for the value of both electricity generation and illumination provided by a stPV window. The model is parameterized by the threshold wavelength (λ_c). Wavelengths shorter than λ_c are absorbed and converted in the PV cell whereas longer wavelength portions of the spectrum are used for lighting. By applying this framework to an ideal spectrally selective stPV window, we find that stPV with a λ_c (i.e., bandgap) chosen to maximize the net power generation provided by the multifunctional device could produce up to 12.5 mW/cm^2 with a reduction of only 6.3% in illumination provided by the window. Additionally, we show that the value of incorporating stPV into a window increases as artificial lighting efficiencies continue to improve, making stPV windows a technology that will only become more attractive in the future. We believe this framework will be a valuable tool to guide future research into stPV windows by providing a quantitative, application specific performance metric.

7.2 Developing a Quantitative Framework for stPV

The basic concept of stPV and the underlying conversion of broadband solar radiation for dual purpose of lighting and power generation is schematically illustrated in Figure 7.1. A fraction of the sunlight incident on the external window is absorbed by the solar cell to generate power while the rest is transmitted into the building to provide illumination. To accurately assess the total impact of a stPV window, power generation and illumination must be evaluated on a common basis. In a laboratory setting PV performance is commonly characterized by an efficiency determined under illumination with the AM 1.5 reference spectrum with a standard intensity of 100 mW/cm^2 .

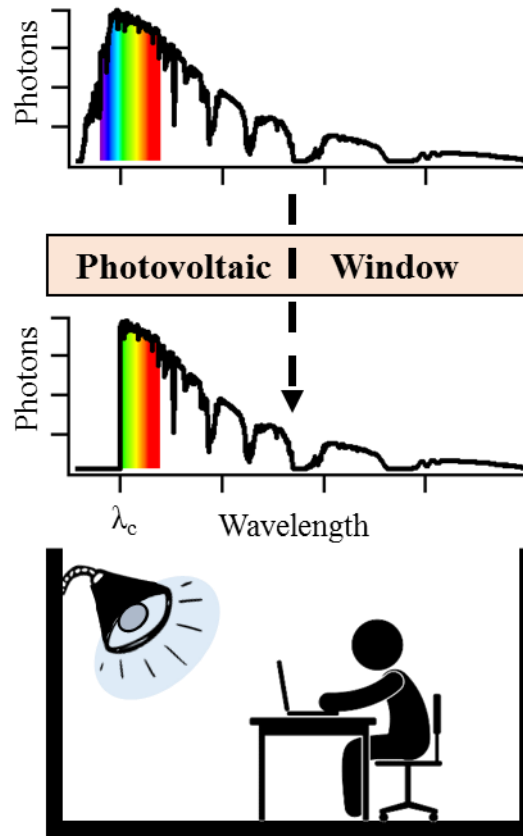


Figure 7.1: Diagram of a semitransparent photovoltaic window. The visible portion of the solar spectrum is indicated by the colored region. Lost illumination due to photovoltaic energy generation is replaced by artificial lighting.

Accounting for the *value* of the transmitted sunlight is less straightforward and merits further discussion. The illuminance provided by a given spectral distribution is calculated by:

$$\phi = 683 \int P(\lambda)V(\lambda)d\lambda \quad \text{Eq. 7.1}$$

Where ϕ is the illuminance (lm/m^2), P is the spectral power density ($\text{W}/\text{m}^2 \cdot \text{nm}$), and V is the photopic response function of the human eye¹¹. The constant factor of 683 scales the integral to account for the definition of the lumen. The spectral power density (P') of the fraction of the incident spectrum that absorbed by the PV is given by the product of the AM 1.5 spectrum (P°) and the absorption function (A) of the stPV across the

wavelength range of interest (i.e., the portion of the incident spectrum not converted by the solar cell).

$$P'(\lambda) = A(\lambda)P^\circ(\lambda) \quad \text{Eq. 7.2}$$

To put these the power generation and lighting contributions on a common scale, we consider the opportunity cost for providing artificial (i.e., make-up) lighting if absorption by the stPV reduces natural lighting provided to the room. We then assign the lost illumination due to absorbing sunlight a value equal to the energy cost of producing an equivalent amount of illumination artificially.

$$P_{eff} = \frac{\phi}{\eta} \quad \text{Eq. 7.3}$$

Where P_{eff} is the effective power cost for artificial illumination, and η is the luminous efficacy of the artificial light source. The luminous efficacy (i.e., the amount of illumination provided per unit of input power) of artificial lighting sources can vary across a wide range, from 15 lm/W for an incandescent bulb to ~350 lm/W, the theoretical upper bound for the efficacy of a white light source¹².

Once electricity generation and illumination are on a common scale, a stPV window can be evaluated by comparing the generated power and the cost of replacing the lost illumination. Condensing the two functions of a stPV window into a single number leads to a simple heuristic, *incorporation of a semitransparent PV layer into a window only makes sense if the energy benefits of the PV layer outweigh the energy cost to replace the lost illumination*. The scope of this communication focuses on power generation and illumination to provide a general framework. Beyond the general model detailed here, we note that specific stPV systems can be analyzed by including a more nuanced view of insolation, lighting use in buildings, and the effect of reduced light transmission on heating and cooling.^{13, 14}

7.3 Optimization of Spectrally Selective stPV

Many demonstrated and commercialized stPV solutions use active layers that absorb a fraction of light across the entire visible spectrum and seek to provide a neutral color PV-window^{3, 15-17}. In this work, we focus on maximizing the combined contributions from both power generation and illumination and hence suggest an alternative approach. Instead of absorbing a fraction of light across the entire breadth of the incident spectrum, stPV windows could instead leverage the spectral sensitivity of the human eye and the solar cell and selectively use portions of the spectrum where they are most effective in either lighting or power generation. In the analysis outlined below, we assume a one-to-one relationship between incident photon and generated electron-hole pair. Concepts such as hot carrier collection or multiple exciton generation can be readily incorporated by appropriate adaptations of the PV portion of the model¹⁸⁻²⁰.

The human eye does not perceive every photon as equally bright, instead the spectral sensitivity function of the human eye can be described, to a first approximation, as a Gaussian form with a peak at 555 nm. Figure 7.2a shows the visible and UV portion of the AM 1.5 spectrum as well as the relative value of a photon to the human eye and an idealized solar cell with $\lambda_c=555$ nm. The key take-away illustrated by the analysis shown in Figure 7.2a is that there exists a significant fraction of incident solar energy in the blue and UV part of the spectrum that is not highly valued by the human eye, but can instead be utilized more effectively to generate power in a solar cell with an appropriate bandgap.

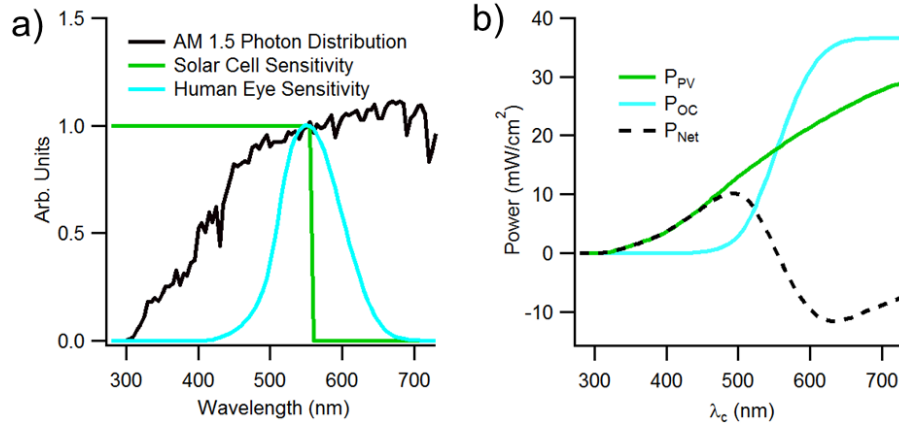


Figure 7.2: a) The AM 1.5 spectrum (black) has significant intensity that is more valuable to a solar cell (green), than to the photopic response function of human eye (blue). b) Net power generated by a stPV window as the absorption edge is varied (black) as well as the power generation of PV (green) and cost of artificially replacing lost illumination (blue) components.

The bandgap (i.e., absorption threshold energy, hc/λ_c) of the semi-transparent solar cell material therefore defines the key parameter governing the balance between power generation and lighting. We determine the optimum bandgap of a spectrally selective stPV window using the method of evaluating stPVs detailed above. The upper bound for the power generation of the solar cell is set by the detailed balance conversion efficiency limit as described by Shockley and Queisser^{10†}.

To determine the illumination provided by transmitted light as a function of the bandgap we use equations 7.1 and 7.2 and adjust P' assuming complete transmission of photons with energy below the bandgap (longer wavelengths) and complete absorption of photons with energy above the bandgap (shorter wavelengths). Figure 7.2b shows the results of these calculations using a luminous efficacy of 300 lm/W for the artificial lighting source. For a stPV cell with an bandgap of 2.5 eV ($\lambda_c = 495$ nm), the detailed balance analysis predicts a maximum power generation of 12.5 mW/cm²; such a cell would reduce the natural lighting by 6.3%. The opportunity cost associated with the

artificial ‘make up’ lighting provided at a luminous efficacy of 300 lm/W, would require $\sim 2.5 \text{ mW/cm}^2$, which renders the stPV cell with a net gain of 10 mW/cm^2 .

From equation 7.3, we can see that when the luminous efficacy of artificial lighting is reduced, the opportunity cost of lost illumination increases, reducing the net gain in power. Figure 7.3a shows the net power generation for an optimal stPV window for a range of luminous efficacies of artificial lighting system. Even for the lowest luminous efficacy artificial lighting sources in use, incandescent bulbs ($\eta=15 \text{ lm/W}$), there is a benefit to absorbing the UV and some visible photons. As the luminous efficacy of artificial lighting increases, the λ_c that maximizes the total benefit of the stPV window shifts to longer wavelengths, as shown in Figure 7.3b. Most of the change in both the magnitude and location of the maxima in P_{net} occurs at low luminous efficacies, which currently available lighting technologies have met or surpassed^{21, 22}. In addition, P_{net} has a flat maximum, staying within 90% of the peak value for PV λ_c within $\sim 20 \text{ nm}$ of the maximum. Together these results indicate that stPV windows reflect an emerging energy technology that is robust to future changes in PV technology and indoor lighting. In fact, improvements in artificial lighting will not make a previously installed stPV window obsolete, instead the stPV windows become more attractive as artificial lighting technology improves. With LED luminous efficacies projected to reach 200 lm/W by 2030, the future of stPV for building integrated applications is bright²².

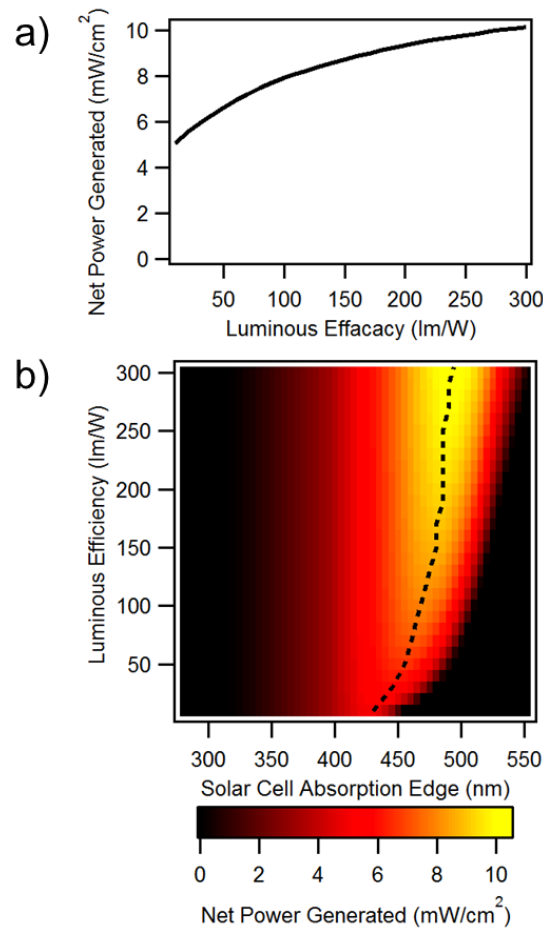


Figure 7.3: a) Maximum net power generation of an optimum stPV window as the luminous efficacy of artificial lighting is varied. b) Net power generation as both absorption edge and luminous efficacy are varied. The dotted line indicates the location of the maximum power generation.

7.4 Conclusions

We present a quantitative framework to evaluate semitransparent photovoltaic windows for building integrated applications through consideration of dual functionality of stPV windows to provide energy and lighting. Using a detailed balance approach to provide an estimate for the PV performance, we determined the optimal bandgap for a spectrally selective stPV window to be 2.5 eV when the luminous efficacy of artificial lighting is high (>100 lm/W). At this optimal bandgap, power generation of up to 12.5

mW/cm² is possible with only a 6.4% reduction in illumination. We also determine that the added benefit of stPV increases with advances in artificial lighting technology. We believe these results will provide guidance and inspiration for future work on building integrated stPV.

Footnotes

† The AM 1.5 spectrum used to characterize solar cells represents the power incident on a PV panel under a well-defined set of standard conditions. In practice, the intensity of sunlight varies with predictable factors such as latitude, time of year, and time of day as well as unpredictable factors like local weather conditions. Studies of installed stPV indicate unsurprisingly that stPV is subject to these same variations¹⁷. An additional consideration for stPV windows is orientation, stPV installed vertically or horizontally, as windows or skylights respectively, will have a reduced photon flux compared to the AM 1.5 spectra. While all of these effects will reduce the power generation and illumination provided by a stPV window, it will not affect the critical question of whether incorporation of stPV into windows is a net benefit to a building, as reduced photon flux will affect lighting and power generation equally. To describe an upper bound for power generation, the calculations use the AM 1.5 spectrum without accounting for any factors that would reduce the photon flux.

‡ Selective absorption of the UV and blue photons would give the transmitted light and stPV window an orange hue (CIE 1931 $x=.44$ $y=.52$ $z=.036$). The positive or negative aesthetic value of colored windows is beyond the scope of this communication. However, we note that artificial lighting with a higher correlated color temperature, appearing more blue-white, could be used to offset the loss of blue photons and

reproduce a more natural lighting environment. This has the added advantage of high CCT sources being more efficient as there is less lost energy to IR emissions.

REFERENCES

1. Jean, J.; Brown, P. R.; Jaffe, R. L.; Buonassisi, T.; Bulović, V. *Energy & Environmental Science* **2015**, 8, 1200-1219.
2. Zheng, C.; Kammen, D. M. *Energy Policy* **2014**, 67, 159-169.
3. Quiroz, C. O. R.; Levchuk, I.; Bronnbauer, C.; Salvador, M.; Forberich, K.; Heumüller, T.; Hou, Y.; Schweizer, P.; Spiecker, E.; Brabec, C. J. *Journal of Materials Chemistry A* **2015**, 3, 24071-24081.
4. Guo, F.; Kubis, P.; Przybilla, T.; Spiecker, E.; Hollmann, A.; Langner, S.; Forberich, K.; Brabec, C. J. *Advanced Energy Materials* **2015**.
5. Guo, F.; Ameri, T.; Forberich, K.; Brabec, C. J. *Polym. Int.* **2013**, 62, 1408-1412.
6. Yang, Y.; O'Brien, P. G.; Ozin, G. A.; Kherani, N. P. *Appl. Phys. Lett.* **2013**, 103, 221109.
7. Betancur, R.; Romero-Gomez, P.; Martinez-Otero, A.; Elias, X.; Maymo, M.; Martorell, J. *Nat Photon* **2013**, 7, 995-1000.
8. Chen, C.-C.; Dou, L.; Zhu, R.; Chung, C.-H.; Song, T.-B.; Zheng, Y. B.; Hawks, S.; Li, G.; Weiss, P. S.; Yang, Y. *ACS Nano* **2012**, 6, 7185-7190.
9. Lunt, R. R. *Appl. Phys. Lett.* **2012**, 101, 043902.
10. Shockley, W.; Queisser, H. J. *J. Appl. Phys.* **1961**, 32, 510-519.
11. Boyce, P. R., *Human factors in lighting*. Crc Press: 2014.
12. Murphy Jr, T. W. *J. Appl. Phys.* **2012**, 111, 104909.
13. Nabil, A.; Mardaljevic, J. *Lighting Research and Technology* **2005**, 37, 41-57.
14. Chae, Y. T.; Kim, J.; Park, H.; Shin, B. *Applied Energy* **2014**, 129, 217-227.
15. Czolk, J.; Puetz, A.; Kutsarov, D.; Reinhard, M.; Lemmer, U.; Colsmann, A. *Advanced Energy Materials* **2013**, 3, 386-390.
16. Chen, K.-S.; Salinas, J.-F.; Yip, H.-L.; Huo, L.; Hou, J.; Jen, A. K.-Y. *Energy & Environmental Science* **2012**, 5, 9551-9557.
17. Yoon, J.-H.; Song, J.; Lee, S.-J. *Solar Energy* **2011**, 85, 723-733.
18. Nozik, A. J.; Beard, M. C.; Luther, J. M.; Law, M.; Ellingson, R. J.; Johnson, J. C. *Chem. Rev.* **2010**, 110, 6873-6890.
19. Moore, D. T.; Gaskey, B.; Robbins, A.; Hanrath, T. *J. Appl. Phys.* **2014**, 115, 054313.
20. Nozik, A. *Physica E: Low-dimensional Systems and Nanostructures* **2002**, 14, 115-120.
21. Bergesen, J. D.; Tähkämö, L.; Gibon, T.; Suh, S. *Journal of Industrial Ecology* **2015**,
22. Bardsley, N.; Bland, S.; Pattison, L.; Pattison, M.; Stober, K.; Welsh, F.; Yamada, M. *Energy Efficiency & Renewable Energy* **2014**.

CHAPTER 8

FUTURE WORK AND CONCLUSIONS

As detailed in the previous chapters, nanocrystal thin films are a rich and exciting class of nanomaterials. The ability to tune the composition and structure of NC films across over 7 orders of magnitude in length scale with 3 different levels of control is a powerful tool for creating materials with properties by design.

My work has presented a detailed study of several interesting processing methods for tuning the properties of NC films that combine control over the 3^o structure of the NC film while also impacting the NC at the 1^o (atomic) and 2^o (nanocrystal) levels. Non-equilibrium thermal annealing enabled not only creating large area electronically coupled NC films with spatial control over the bandgap of the NC film, but also enabled kinetic trapping of the NC films in states of 2^o structure inaccessible via wet chemical synthesis. The simultaneous exchange of both cations and ligands in a Z type ligand exchange improves upon the conventional chemical procedure for electronically coupling NC films by improving, rather than degrading, the properties of the NCs through control of the 1^o structure of the NC surface. Post assembly SILAR enabled repair of structural defects and increased electronic coupling among NCs in long range ordered, epitaxially connected NC films. Although the quantitative framework for evaluation of stPV is purposefully materials agnostic, the tunable bandgap of NCs makes them a strong candidate for the active layer in stPV applications.

While I believe my contributions to the field of semiconductor NCs are interesting and valuable, there is still a significant amount of work to be done on these systems at all levels of structure. As I have focused on controlling the 3^o structure to make designer NC films, integration of these films into prototype devices at the 4^o level is of course of great interest. However, there are many interesting challenges still to be

addressed at the lower levels of control over NCs, from continued expansion of our synthetic abilities, to new and improved methods for controlling the structure and bonding in NC films. Below I will summarize briefly the future directions I would take if I were to start another PhD's worth of research in this field. It is my hope that some of the projects will be considered, so I will try to layout as clearly as I can the steps that might be appropriate.

8.1 Laser Annealing for White Light LEDs

The last section of Chapter 4 detailed preliminary results regarding using ssLSA to spatially tune the emission from a NC film. I think this is a project worth pursuing. However, due to considerations at the 4° level, mainly the demand that phosphors in downconverting applications have high quantum yield, the CdSe NCs studied in Chapter 4 may be a poor choice. Instead I believe a more successful course of action would be to focus on core-shell particles with high quantum yields. There are many core-shell NC systems available and in order to simplify the discussion, I will explicitly address CdSe/CdS core shell particles. I believe however that the idea should generalize to most core-shell NC systems.

Instead of controlling the NC emission through control of the 2° structure via fusion, I would focus on controlling the 1° structure of the heteronanocrystal and tune the emission wavelength via atomic diffusion between the core and the shell. In the case of the CdSe/CdS system, diffusion of S ions into the core, and Se atoms out to the shell, would change the radial composition profile in the NC. The change in composition would lead to a change in shape and depth of the confining potential felt by an exciton in the NC. While the precise effect of alloying is uncertain, the 'bulk bandgap' should increase but smoothing out of the potential well could lead to decreased quantum confinement and a decreased bandgap. In any event, I find it unlikely that

nothing will change^{1,2}. Figure 8.1 shows the hypothesized composition profile of a NC and a possible confinement potential for the system.

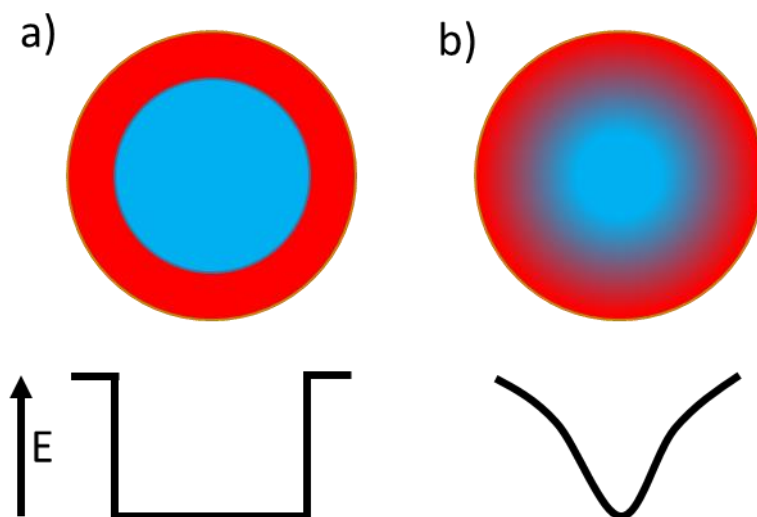


Figure 8.1: Hypothetical composition profile (top) and confinement potential (bottom) for a) discrete core-shell NC and b) alloyed core-shell NC. The effect of alloying on the NC bandgap is uncertain

An outline of the experimental steps would go something like:

- i) Master synthesis of core-shell NCs
- ii) Heat NC in a high boiling point solvent to induce diffusion at long time scales. This will provide an understanding of the effect of diffusion on the bandgap and make interpretation of the laser annealing experiments easier
- iii) Incorporate NC into a polymer that will not degrade during ssLSA
- iv) Find LSA processing conditions to produce atomic diffusion on short time scales
- v) Integrate resulting films with a high efficiency blue LED to produce white LEDs with tunable emission

Each step above would, of course, require detailed characterization of the NCs and NC/polymer composites.

8.2 Improving Confined-but-Connected Films

The long range ordered, epitaxially connected nanostructured films studied in Chapter 6 are, in my opinion, the most direct parallel of using NCs as ‘artificial atoms’ and present an exciting opportunity to produce 3^o level NC films with novel collective properties. In particular, the honeycomb structures that have been studied experimentally by Boneschanscher *et al* and theoretically by Kalesaki *et al* provide an opportunity to produce tunable, NC based analogs of graphene^{3,4}. Although current state of the art films have not exhibited these collective properties, I think improved understanding of the film assembly and improved processing methods may help to improve the quality of CBC films.

I believe that future work on CBCs should focus on two parallel paths. The first should continue to focus on the CBC films at the nm to μm scale. The goal should be to reduce and eliminate the two sources of disorder that we believe limit the current performance, unformed epitaxial bonds and paracrystalline disorder, which we believe is fundamentally related to the polydispersity of the NCs. I believe that improved control over the 2^o structure of the building blocks may be able to improve both simultaneously. If we assume a fundamental limit to the standard deviation in NC size is 1 Pb-Se bond length (.3 nm), I see two routes forward. One possibility is to move to larger particles in order to reduce the relative polydispersity of the NCs. This has the additional advantage that, as PbSe particles get larger, they change in shape to be more cubic and exhibit larger [100] facets. The more cubic particles should exhibit stronger anisotropic interactions that may either lead to the NCs assembling in a square pattern before ligand removal or else make the transition from hexagonal close packed to square array smoother leading to (hopefully) better ordering. In addition, larger [100] facets

should mean thicker epitaxial connections between NCs and stronger electronic coupling in the film.

The second way I see to address the issue of polydispersity is to move to magic size particles. As these particles should be identical and would eliminate both the electronic disorder and structural disorder associated with a polydisperse set of NCs. While using magic sized building blocks can potentially eliminate one source of disorder, PbSe magic size NC are not well understood and so using them as building blocks may lead to unpredictable results⁵. The magic NC clusters may exhibit unusual faceting that could drive assembly into structures beyond the hexagonal and square symmetries observed so far. In addition, the surface and ligand structure of magic size NCs are likely very sensitive to the local environment, so it is not clear what would happen to an arrangement of magic size NCs when the ligands were removed by ethylene diamine.

In parallel to work improving the quality of CBCs, I would suggest working to scale up the liquid interface assembly process. Our current film assembly takes place in a ~ 1 cm² trough. The enhanced mobility provided by the liquid interface during assembly seems to be crucial for retaining long range order during ligand exchange and removal, so finding a way to produce larger area films while still using a liquid subphase will be important. Die slot coating seems to me to be an attractive, high throughput liquid film coating method that may be worth studying in detail. Die slot coating, diagrammed in Figure 8.2, is capable of coating multiple liquid layers at one time and is well established in roll to roll processing^{6,7}. I would start just trying to assemble large area (10^2 's of cm²) films of NC to establish the processing parameters. Then, as the work on improving the structure and order of CBCs improves, the successive processing techniques could be incorporated into a large area liquid film coating process to produce large area CBCs ready for incorporation into prototype devices.

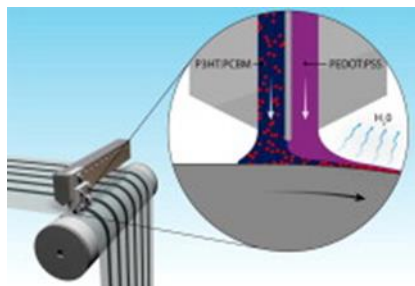


Figure 8.2: Multilayer die-slot coating. From ⁷ Copyright 2012 Elsevier

8.3 Expanding the stPV Model

In Chapter 7, I mention that the simple model presented could easily be adjusted to include more realistic lighting use, insolation data, and could consider the effect of heating and cooling in buildings. I think this would be a very worthwhile expansion of the model. The heuristic emphasized in Chapter 7 is that stPV makes sense if it decreases net power use in a building. While the simple model in Chapter 7 provides an initial estimate of the power savings and optimal stPV bandgap. I believe a more thorough and realistic calculation is likely to provide a different, and more accurate assessment of this novel application of PV, and I would be interested to see the results.

8.4 Conclusion

The future work I have detailed above is just the initial next steps that I can see from my current position at the end of my time as a graduate student. I expect that the field will continue to progress as rapidly over the next 5-10 years as it has while I have been following it closely. New NC syntheses will be developed that will allow for investigation of novel materials and heterostructures with exciting new properties. I hope that the processing methods I have detailed in this dissertation, as well as the future work that may be influenced or inspired by my work, can serve to take the new artificial atoms and use them to build designer materials that enable

many new and interesting innovations in the myriad fields of science and technology.

REFERENCES

1. Panda, S. K.; Hickey, S. G.; Waurisch, C.; Eychmüller, A. *J. Mater. Chem.* **2011**, *21*, 11550-11555.
2. Bailey, R. E.; Nie, S. *J. Am. Chem. Soc.* **2003**, *125*, 7100-7106.
3. Boneschanscher, M. P.; Evers, W. H.; Geuchies, J. J.; Altantzis, T.; Goris, B.; Rabouw, F. T.; van Rossum, S. A. P.; van der Zant, H. S. J.; Siebbeles, L. D. A.; Van Tendeloo, G.; Swart, I.; Hilhorst, J.; Petukhov, A. V.; Bals, S.; Vanmaekelbergh, D. *Science* **2014**, *344*, 1377-1380.
4. Kalesaki, E.; Delerue, C.; Morais Smith, C.; Beugeling, W.; Allan, G.; Vanmaekelbergh, D. *Physical Review X* **2014**, *4*, 011010.
5. Evans, C. M.; Guo, L.; Peterson, J. J.; Maccagnano-Zacher, S.; Krauss, T. D. *Nano Lett.* **2008**, *8*, 2896-2899.
6. Maenosono, S.; Okubo, T.; Yamaguchi, Y. *J. Nanopart. Res.* *5*, 5-15.
7. Larsen-Olsen, T. T.; Andreasen, B.; Andersen, T. R.; Böttiger, A. P.; Bundgaard, E.; Norrman, K.; Andreasen, J. W.; Jørgensen, M.; Krebs, F. C. *Sol. Energy Mater. Sol. Cells* **2012**, *97*, 22-27.

APPENDIX A

SUPPLEMENTARY INFORMATION FOR: PROCESSING-STRUCTURE- PROPERTY RELATIONSHIPS IN LASER ANNEALED PbSe NANOCRYSTAL THIN FILMS

A.1: Advice for Students

Laser annealing is a really powerful processing method that enables creation of structures at the tertiary level that you couldn't produce in other ways. However, it is really important to understand the limitations of the various lasers that you might use to do the laser annealing, as that can have a large impact on if you can translate an idea on a whiteboard to an interesting experiment. The most critical consideration is for using direct heating, either with the excimer laser, or laser spike annealing with the diode laser, is the film thickness. As was shown in the main text and is further detailed in this appendix, even the difference between a monolayer and a bilayer can be enough to significantly change the effect of laser annealing. When annealing thicker films, this may become less of an issue, because the relative difference in film thickness will be reduced. However, in thicker films the thermal generation profile in a thick film would be highly non-uniform so you may get a completely different morphology between the top and the bottom of a film, especially when using the excimer, where the ns pulse length leads to very short thermal diffusion lengths. One way to address this, that Prof. Thompson has suggested previously, is to deposit a thin layer of amorphous Si onto a substrate that is transparent to the wafer, and then deposit a NC film on top of the a-Si. If the excimer pulse comes from the back of the wafer, it will be absorbed by the Si

which will act as a ns hotplate, just like the Si substrate does in LSA. Note that this only changes where the heat is coming from and how it is transferred, it doesn't do anything to change the diffusion lengths during ns heating.

When using the CO₂, or the diode with a material that won't absorb it, your films must be made on a Si substrate. Thin electrically insulating layers like SiO₂ or SiN can be between you film and the substrate, as long as they have sufficient thermal conductivity. This requirement makes characterization of NCs after you anneal them difficult. We have discussed trying to perform laser annealing on a thin SiN layer and then breaking it off to form a TEM grid, but it has never gone anywhere.

It should be noted, that in order to ensure film uniformity over large areas, laser scans are overlapped. As a result, the thermal history of a film annealed using large area LSA, rather than ssLSA is significantly more complicated than the simple Gaussian cartoon used to describe the method in this work. This is especially important if you were to try to take a laser annealing process you observed in a single scan method and try to reproduce it over a large area film. One way to get an idea about the effect of multiple annealing steps is to anneal two single stripes perpendicular to each other. This produces a ton of data about the effect of multiple annealing steps of various temperatures, and can be difficult to interpret.

A.2 Materials and Methods

Materials: Lead oxide (99.99%) selenium (99.999%, powder), trioctylphosphine (90%, technical grade), oleic acid (OA 70%, technical grade), 1-octadecene (ODE 90%)

diphenylphosphine (98%), were all purchased from Sigma Aldrich and used without further purification.

Nanocrystal Synthesis: PbSe NCs were synthesized using a procedure adapted from Yu *et al*[1]. In a typical synthesis 0.88 g PbO was mixed with 10.8 g of 1-octadecene and 2.76 g oleic acid in a three- neck flask under nitrogen flow and heated to 150°C for 1 hour until all of the PbO had dissolved. 90 μ l diphenylphosphine was mixed with 12 ml of 1 M selenium in trioctylphosphine and quickly injected into the three-neck flask. Injection temperature and growth time can be adjusted to control the final particle size. The NCs were isolated from the reaction product by washing three times using hexane/ethanol as the solvent/antisolvent pair.

Sample Fabrication: Monolayer and sub-monolayer samples for SEM characterization were fabricated by drag coating a 10 mg/ml solution of PbSe NCs in hexane across a Si substrate. Thicker films used for GISAXS and FTIR absorption measurements were dropcast from a 10 mg/ml solution of PbSe NCs in a 9:1 hexane:octane solvent.

Laser Annealing: Excimer annealing was performed using a 308 nm Lambda Physik LPX205i XeCl excimer laser with a 30 ns pulse at full width half max, and a maximum pulse energy of 500 mJ. The beam is homogenized to 3.2×3.2 mm² square with fluences up to 1.5 J/cm². Laser Spike Annealing was performed by scanning a continuous wave CO₂ laser ($\lambda=10.6$ μ m) across a sample. The laser was focused to a beam with a Gaussian full width half maximum (FWHM) of 100 μ m in the direction of a scan and 500 μ m in the lateral direction. Scans were performed at a velocity of 200 mm/s corresponding to a dwell time of 500 μ s. Scans overlapped with a portion of the previous scan to ensure film uniformity.

Characterization: Scanning Electron Microscopy was performed on a LEO 1550 FESEM. FTIR spectroscopy was performed with a Bruker Hyperion 2000 in ATR mode. GISAXS was performed at the D1 beam line of the Cornell High Energy Synchrotron Source (CHESS) using monochromatic radiation of wavelength 1.161 Å and a bandwidth $\Delta\lambda/\lambda=1.5\%$. The X-ray beam was produced by a hardbent dipole magnet of the Cornell storage ring and monochromatized with Mo:B₄C synthetic multilayers with a period of 30 Å. GISAXS images were collected by a MedOptics fiber coupled CCD camera with a pixel size of 46.9 μm by 46.9 μm and a total of 1024 by 1024 pixels with 14 bit dynamical range per pixel. The sample to detector distance was 930 mm, as calibrated by a silver behenate powder standard. Images were dark current corrected, distortion corrected, and flat field corrected by the acquisition software. The incident angle of the X-ray beam was 0.25°. Scattering images were calibrated using the Fit2D software[2].

A.3 Lower Magnification SEM Images of Annealed Films

In addition to the nanocrystal fusion that occurs, laser annealing affects the films at a longer length scale, introducing nanoscopic cracks in the monolayer films. As discussed in the main text bilayers have a significantly different morphology compared to monolayers in PLA films, while LSA films show uniform morphology independent of film thickness.

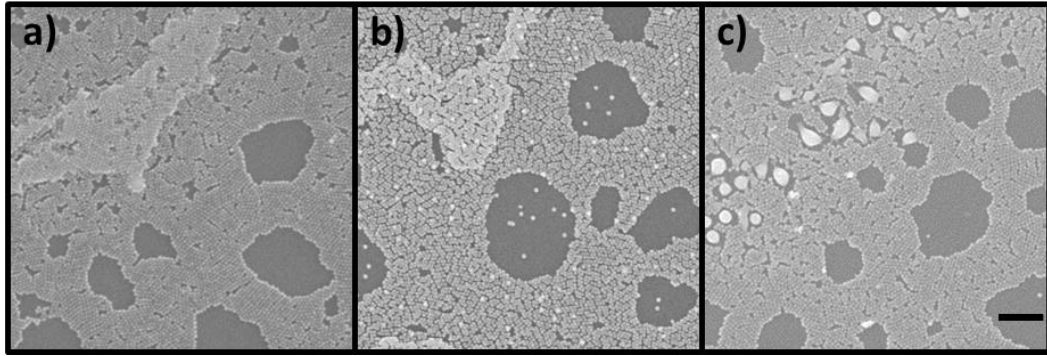


Figure A.1: Scanning electron micrographs of a) unannealed b) Laser Spike Annealed at 440 °C and c) Pulsed Laser Annealed at 90 mJ/cm² NC films. The black scale bar is 200 nm and applies to all micrographs.

A.4 Details of the PLA Thermal Transport Model

Using the imaginary part of the refractive index of a PbSe NCs film measured by Law *et al.* ($k=1.52$)[3] we calculate the absorption coefficient: $\alpha = \frac{4\pi k}{\lambda}$ for the NCs and determine the portion of the energy in a laser pulse absorbed by the NCs in a monolayer or bilayer. A single 12 nm NC absorbs 52.5% of the incident light, so the top NC or a single NC absorbs a Fluence $F= 47.25 \text{ mJ/cm}^2$ and the bottom NC in a bilayer absorbs $F= 22.5 \text{ mJ/cm}^2$ of the 90 mJ/cm^2 pulse under consideration. In the model, NCs are heated at a constant rate corresponding to an even distribution of the absorbed energy over the 30 ns laser pulse giving a monolayer power input of $I=1.58 \cdot 10^{10} \text{ W/m}^2$. We obtain the thermal resistance of the NC using the thickness and thermal conductivities of both PbSe and Pb-Oleate (12 nm, $2 \text{ W m}^{-1} \text{ K}^{-1}$ and 1.8 nm, $.13 \text{ W m}^{-1} \text{ K}^{-1}$ respectively) as well as the interfacial thermal conductance of $1.4 \cdot 10^8 \text{ W m}^{-2} \text{ K}^{-1}$ at a NC/ligand interface found in Ong *et al.*[4] The total resistance is then:

$$\rho_{th} = \frac{12 \cdot 10^{-9}}{2} + \frac{1.8 \cdot 10^{-9}}{.13} + \frac{1}{1.4 \cdot 10^8} = 2.70 \cdot 10^{-8} \frac{m^2 K}{W}$$

Giving a temperature difference of 426 °C.

In the COMSOL model only conduction is considered, and the PbSe NCs are modeled as cubes for simplicity and input power is distributed uniformly in the nanocrystals. Materials constants used in the simulation are in Table S1. Due to the reduced mean free path of phonons in NCs, the thermal conductivity of the PbSe core is likely lower than the bulk value. In addition, removal of ligands during the heating process is not considered in this model. Recent work has shown that the interfacial thermal conductance decreases with decreasing ligand density on the surface of a NCs.[5] Taken together, these simplifications indicate that the simulation overestimates the rate of thermal transport in the NC film and that the temperatures that result from the simulation represent a lower bound on the temperatures that the NCs may experience.

Table A.1: Material constants used in COMSOL model of NC annealing

Material	Thermal Conductivity [W m ⁻¹ K ⁻¹]	Density [g cm ⁻³]	Heat Capacity [J g ⁻¹ K ⁻¹]
PbSe	2	8.27	.18
Oleic Acid	.13	.895	2.043
Silicon	130	2.33	.7

A.5 Detailed Relationship Between LSA temperature and NC Film Morphology

We examine the processing window of opportunity for confined-but-connected nanostructures in detail to study the degree to which connectedness among NCs can be tuned. Figure A.2 shows the processing-structure relationship of the NC film over a

narrow range of annealing temperatures. With increasing annealing temperature, l_d increases leading to more fusion among the particles. The ability to precisely control physical connections among QDs in an assembly provides opportunities to tune the “bonding” among designer atoms in a designer solid, and expand designer solids beyond simple atomic analogs.

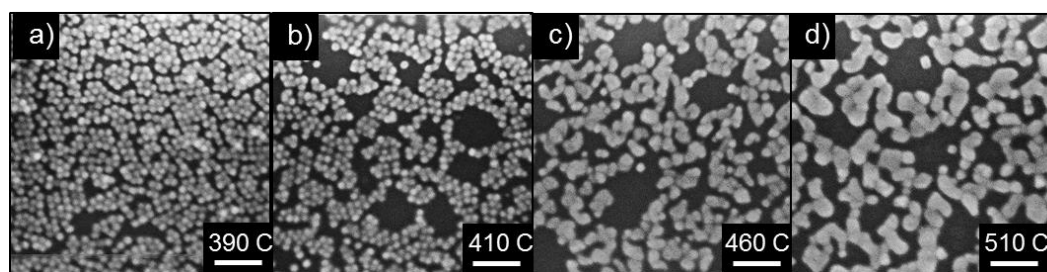


Figure A.2: Tunable film morphology across a range of temperatures. All white scale bars are 100 nm.

A.6 Electrical Conductivity Measurements

We characterized the electrical conductivity after annealing a NC film deposited on a prefabricated electrode structure. We use highly doped silicon with a thermal oxide layer and define thermally evaporated gold electrodes with channel length 16 μm and width 3 mm. Within the channel, the NCs are deposited via drag coating, parallel with the channel. This results in 3 to 5 particle layers. While the contacts reflect the laser radiation, annealing is done perpendicular to the channel width so that the beam is blocked briefly as it sweeps the sample.

To obtain measureable conductance before annealing, we performed a ligand exchange to ethanedithiol (EDT). Conductivity measurements before and after annealing show a 300 fold increase in conductivity (Figure A.3). SEM images of the

NC film before and after annealing show no agglomeration of nanocrystals which suggests that the enhanced transport is due to improved interparticle coupling while the discrete character of individual NCs is preserved.

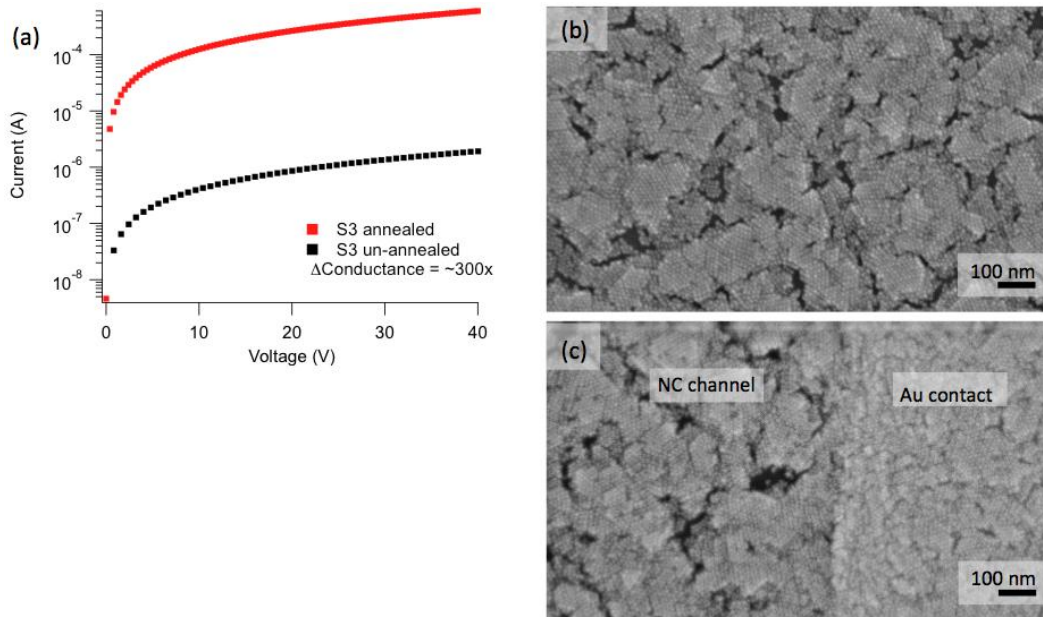


Figure A.3: Electrical conductivity of NC film annealed with the CO₂ laser at 400 °C. (a) 300 fold improvement in electrical conductivity (b,c) SEM images before and after annealing show no agglomeration of NCs in response to annealing.

REFERENCES

- [1] W. W. Yu *et al.*, Chem. Mater. **16**, 3318 (2004).
- [2] A. Hammersley, European Synchrotron Radiation Facility Internal Report ESRF97HA02T (1997).
- [3] M. Law *et al.*, Nano Lett. **8**, 3904 (2008).
- [4] W. Ong *et al.*, Nature Materials **12**, 410 (2013).
- [5] W.-L. Ong *et al.*, The Journal of Physical Chemistry C **118**, 7288 (2014).

APPENDIX B

SUPPLEMENTARY INFORMATION: CONNECTING THE PARTICLES IN THE BOX - CONTROLLED FUSION OF HEXAMER NANOCRYSTAL CLUSTERS WITHIN AN AB₆ BINARY NANOCRYSTAL SUPERLATTICE

B.1 Advice for Students

Assembling a BNSL is black magic. There are many conditions that need to be met for a BNSL to form, the relative sizes of the NCs and relative concentration of NCs need to be correct, and the assembly needs to dry slowly. However, taking care of all of these things is not enough to ensure that a BNSL will form. Other things that are not easy to measure, such as residual ligand concentration can also have an effect on the assembly process and may be critical to getting BNSLs to assemble. In the end, producing a BNSL is really down to trial and error and finding the set of conditions that works for the pair of NCs you are trying to assemble. I found it very helpful to create a spreadsheet that tracked the nominal particle ratio, solvents used, and other details to try to zone in on a set of good conditions. Once you have a good set of conditions for producing BNSLs, it is pretty repeatable.

If I were to repeat this project right now, I would not calculate the GISAXS scattering “by hand” as is done in this work. A couple of months after this paper was published, a whole host of tools for calculating GISAXS scattering came out, including BornAgain and IsGISAXS. These are much more convenient and produce an entire simulated scattering pattern, rather than just the peak intensities like my method does. A good example of what BornAgain can do can be seen in the SI of Kevin Whitham’s CBC transport paper¹.

B.2 Materials and Methods

Materials

Lead oxide (99.99%) selenium (99.999%, powder), trioctylphosphine (90%, technical grade), oleic acid (OA 70%, technical grade), 1-octadecene (ODE 90%) diphenylphosphine (98%), Iron Pentacarbonyl (99.99%), trioctylamine (98%), trimethylamine N-oxide (98%), toluene (%) and tetrachloroethylene (99%) were all purchased from Sigma Aldrich and used without further purification.

NC Synthesis

PbSe NCs were synthesized using a procedure adapted from Yu *et al*². In a typical synthesis 0.88 g PbO was mixed with 10.8 g of 1-octadecene and 2.76 g oleic acid in a three-neck flask under nitrogen flow and heated to 150°C for 1 hour until all of the PbO had dissolved. 90 µl diphenylphosphine was mixed with 12 ml of 1 M selenium in trioctylphosphine and quickly injected into the three-neck flask. The mixture was heated back up to 135°C and allowed to grow for 3 minutes until it was quenched. The NCs were isolated from the reaction product by washing three times using hexane/ethanol as the solvent/antisolvent pair.

Fe₂O₃ NCs were synthesized using a procedure adapted from Hyeon *et al*³. In a typical synthesis 0.65 g oleic acid was mixed with 10 ml of trioctylamine and heated under vacuum at 250 °C for 1 hour. 0.2 ml of iron pentacarbonyl was injected into the solution and allowed to react for 20 minutes at 250 °C before being heated to 320 °C for an hour in order to form monodisperse iron NCs. The reaction was then cooled to room temperature without quenching and 0.17 g trimethylamine N-oxide was added to the reaction mixture and subsequently heated to 130 °C for 1 hour to oxidize the NCs. The NCs were isolated from the reaction product by washing, as described above.

Sample Characterization

Transmission Electron Microscopy was performed on a FEI Tecnai T12 operating at 120 kV. Scanning Electron Microscopy was performed on a LEO 1550 FESEM. Optical Microscopy was performed with an Olympus BH-2 operating in bright field mode. All images were acquired digitally.

GISAXS was performed at the D1 beam line of the Cornell High Energy Synchrotron Source (CHESS) using monochromatic radiation of wavelength 1.161 Å and a bandwidth $\Delta\lambda/\lambda=1.5\%$. The X-ray beam was produced by a hardbent dipole magnet of the Cornell storage ring and monochromatized with Mo:B₄C synthetic multilayers with a period of 30 Å. GISAXS images were collected by a MedOptics fiber coupled CCD camera with a pixel size of 46.9 μm by 46.9 μm and a total of 1024 by 1024 pixels with 14 bit dynamical range per pixel. The sample to detector distance was 930 mm, as calibrated by a silver behenate powder standard. Images were dark current corrected, distortion corrected, and flat field corrected by the acquisition software. The incident angle of the X-ray beam was between .2° and .4°, with most data shown collected at .25°. Scattering images were calibrated and integrated using the Fit2D software⁴. GISAXS peaks were indexed using our in-house software⁵.

Assembly of Binary NC Superlattices

Superlattices were assembled via controlled evaporation of a solution of half toluene half tetrachlorethylene containing both Fe₂O₃ and PbSe NCs. The concentration of NCs in the solution was 1 mg/ml. Appropriate amounts of NCs were added to target a 6:1 PbSe: Fe₂O₃ ratio. Particle concentrations were estimated following the procedure outlined in Smith et al⁶. A substrate, either a TEM grid or cleaned Si wafer fragment, and a volume of solution sufficient to cover the substrate was tilted at a 45° angle and placed in a vacuum oven at 50 °C and 30 kPa and left to dry overnight.

Sample Annealing

In situ annealing was performed by placing a GISAXS sample onto a heating stage custom built at the D1 station at CHESS. The stage was heated by two heating cartridges, inserted into holes in the aluminum stage. The heating cartridges were connected to a variac to control the power input, and the temperature was monitored by a thermocouple placed between the heating cartridges. GISAXS samples were heated from 30 °C to 200 °C at a rate of 2 °C/min.

Laser Spike Annealing was performed by scanning a continuous wave CO₂ laser ($\lambda=10.6 \mu\text{m}$) across a sample. The radiation is absorbed by the highly doped Si substrate, which conductively heats the BNSL film. The laser was focused to a beam with a Gaussian full width half maximum (FWHM) of 100 μm in the direction of a scan and 500 μm in the lateral direction. Scans were performed at a velocity of 100 mm/s corresponding to a dwell time of 1 ms. Scans overlapped with a portion of the previous scan to ensure film uniformity.

B.3 Single Component vs Binary Superlattices

The samples used for *in situ* GISAXS and laser spike annealing were prepared on silicon substrates. SEM characterization of these samples serves as a complementary characterization technique that allows us to confirm that the scattering patterns observed come from BNSLs and not single component assemblies. As only the Fe₂O₃ particles could be resolved in SEM, we distinguish between single component and binary assemblies based on EDX indicating the presence of both Pb and Se in the assembly as well as the square packing of the Fe₂O₃ nanoparticles on the surface of the superlattices. Fe₂O₃ single component assemblies pack in a FCC assembly with the superlattice's 111 plane parallel to the substrate, whereas BNSLs pack in simple cubic arrangement with the 100 plane parallel to the substrate. GISAXS patterns confirm the observations from the SEM images and show unique

scattering patterns for each assembly. A side to side comparison between assembled BNSLs and Fe_2O_3 single component superlattices is shown in Figure B.1.

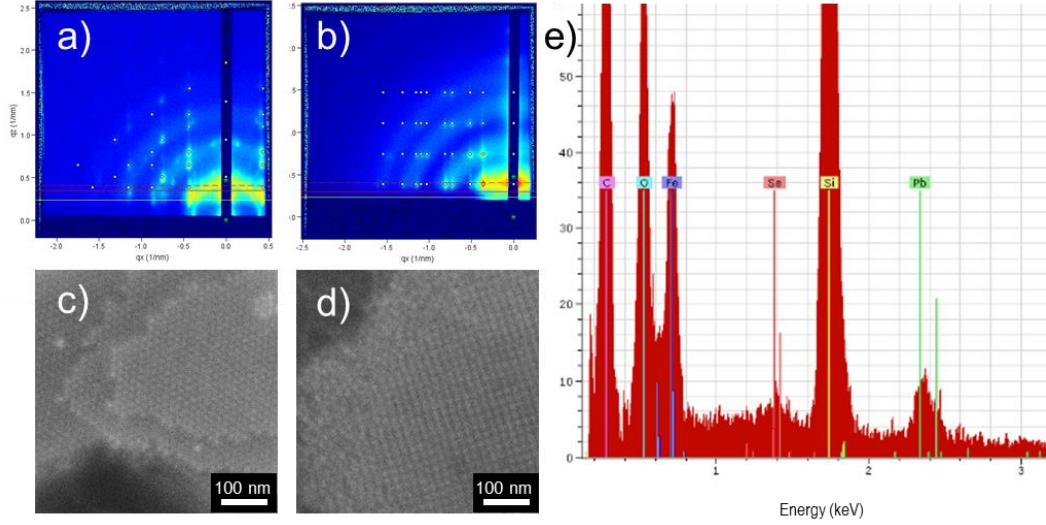


Figure B.1: a) GISAXS pattern from an Fe_2O_3 assembly. Diamonds indicate the locations of peaks corresponding to an FCC structure. b) GISAXS of a BNSL. Diamonds indicate the locations of peaks corresponding to a simple cubic structure. c,d) SEM images of single component and binary assemblies respectively. d) EDX spectra from a BNSL.

B.4 Molecular Dynamics Simulations

The simulations were carried out using Sandia National Laboratory's LAMMPS software package⁷. We have used a united atom approach following Paul *et al*⁸. The potentials for the bonded interactions are given by

$$E_{bond} = K_2(r - r_0)^2 + K_3(r - r_0)^3 + K_4(r - r_0)^4$$

$$E_{ang} = K [\cos(\theta) - \cos(\theta_0)]^2$$

$$E_{dih} = \frac{1}{2}K_1[1 + \cos(\Phi)] + \frac{1}{2}K_1[1 + \cos(2\Phi)] + \frac{1}{2}K_1[1 + \cos(3\Phi)] \\ + \frac{1}{2}K_1[1 + \cos(4\Phi)]$$

Non-bonded interactions are defined using Lennard-Jones potential:

$$E_{vdwl} = 4\varepsilon \left[\left(\frac{\sigma}{r} \right)^{12} - \left(\frac{\sigma}{r} \right)^6 \right]$$

The parameters are:

Bond	R0 [Å]	K2 [kcal/mol/Å ²]	K3 [kcal/mol/Å ³]	K4 [kcal/mol/Å ⁴]
CH ₂ – CH ₂	2.242	136.686	-522.8240	1036.9342
CH ₂ – CH ₃	2.242	136.686	-522.8240	1036.9342
Angle	K [kcal/mol]	θ ₀ (rad)		
CH ₂ -CH ₂ -CH ₂	60	110		
CH ₂ -CH ₂ -CH ₃	60	110		
Dihedral	K1 [kcal/mol]	K2 [kcal/mol]	K3 [kcal/mol]	K4 [kcal/mol]
CH ₂ -CH ₂ -CH ₂ -CH ₂	1.6	-0.867	3.24	0.0
CH ₂ -CH ₂ -CH ₂ -CH ₃	1.6	-0.867	3.24	0.0

Non-bonded interactions	σ (Å)	ε (kcal/mol)
Pb - Pb	3.29	0.0596
Se - Se	4.36	0.0899
Pb - Se	3.775	0.0732
CH ₂ – CH ₂	4.009	0.09344
CH ₃ – CH ₃	4.009	0.22644
CH ₂ – CH ₃	4.009	0.14546
CH ₂ - Pb	3.649	0.0746
CH ₃ - Pb	3.649	0.1161
CH ₂ - Se	4.185	0.0916
CH ₃ - Se	4.185	0.1427

The LJ parameters for the description of core-core, core-ligand and ligand-ligand interactions are taken from Vlught *et al*⁹. We thermalized the system in the constant-temperature, canonical, ensemble at 300 K for 2 ns in steps of 2 fs.

Steered Molecular Dynamics (SMD)

External forces were applied to direct the NCs towards this common point by tethering them to it. The NCs were moved with a relatively slow constant velocity of

2.5×10^{-6} Å/fs and were allowed to rotate along any axis as demanded by the interactions with approaching neighbor NCs and the ligands covering the facets.

We have considered the impact of the relative orientation of the NCs by considering a number of different initial configurations. The initial configurations differ by the orientation of the facets, i.e., if square or hexagonal facets are oriented towards the geometrical center of the hexamer and by the orientation with respect to other NCs. The energies and inter-NC distances of each case differ within 1.5 kcal/mol per ligand and 1 Å (i.e., 2%), respectively.

We have also found out that MD with no applied force can achieve hexameric configuration too. Constant temperature (300 K) simulations for 6 ns for the representative case in which the ligand density is 1.01 nm^{-2} shows the formation of hexamer with inter-NC distance offset only by 2 Å from the SMD minimum geometry. Still the SMD minimum geometry is slightly favored by energy (about 1 kcal/mol) and is identical to the experimental determination.

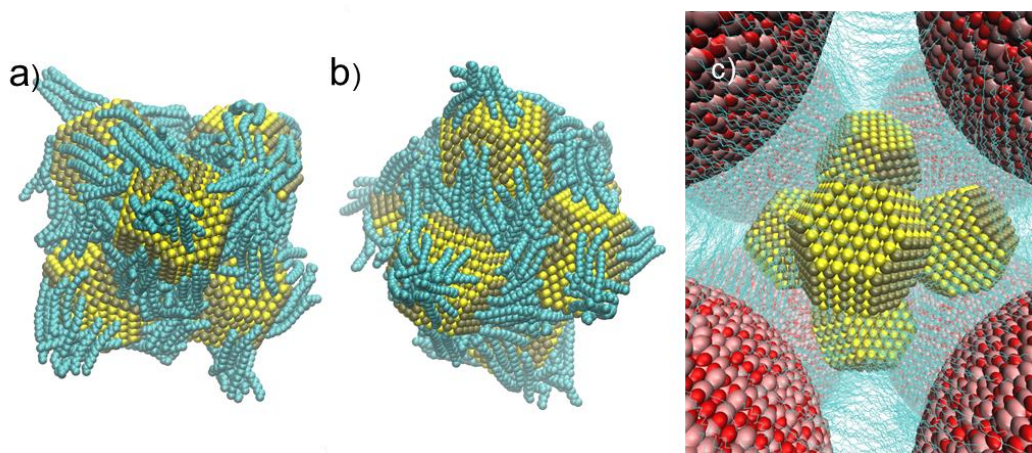


Figure B.2: a,b) additional MD snapshots of the simulated BCH with ligand coverage 1.1 nm^{-2} . c) Snapshot of the BCH in the center of the Fe_2O_3 simple cubic assembly.

B.5 Rearrangement of Nanocrystals After Annealing

The fusion of the BCH increases the available free space inside of the BNSL unit cell. Thermodynamic analyses of BNSL assembly frequently invoke maximizing particle packing density as a driving force for assembly. In this case, treating the fused BCH as a sphere, the configuration of Fe_2O_3 nanocrystals around the BCH that maximizes the packing density is one where the BCH is six-fold coordinated rather than the eightfold coordination that occurs in a CsCl-like structure. The decrease in available free space can be seen in Figure B.4 comparing models of eightfold and six-fold coordinated PbSe and Fe_2O_3 nanocrystals. If the thermal energy provided by annealing enables the nanocrystals to shift towards the preferred local configuration, the long range ordering of the superlattices would be interrupted.

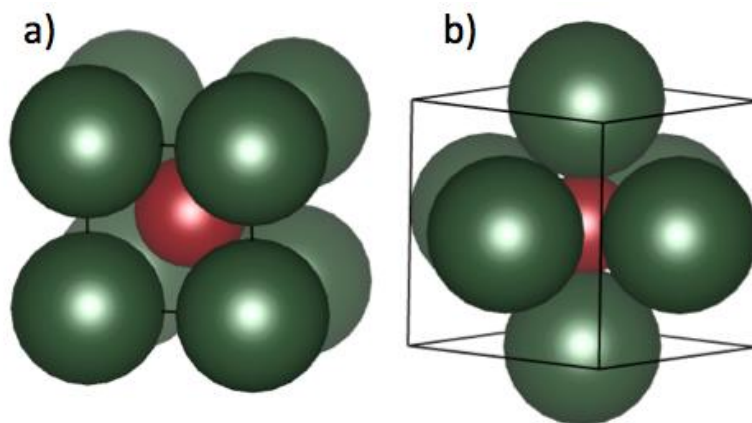


Figure B.3: Projections of a spherical approximation of the fused BCH (red) in a) eight-fold coordination and b) six-fold coordination by Fe_2O_3 nanocrystals (green).

REFERENCES

1. Whitham, K.; Yang, J.; Savitzky, B. H.; Kourkoutis, L. F.; Wise, F.; Hanrath, T. *Nature materials* **2016**.
2. Yu, W. W.; Falkner, J. C.; Shih, B. S.; Colvin, V. L. *Chem. Mater.* **2004**, 16, 3318-3322.
3. Hyeon, T.; Lee, S. S.; Park, J.; Chung, Y.; Na, H. B. *J. Am. Chem. Soc.* **2001**, 123, 12798-12801.
4. Hammersley, A. *European Synchrotron Radiation Facility Internal Report ESRF97HA02T* **1997**.
5. Smilgies, D.-M.; Blasini, D. R. *J. Appl. Crystallogr.* **2007**, 40, 716-718.
6. Smith, D. K.; Goodfellow, B.; Smilgies, D.; Korgel, B. A. *J. Am. Chem. Soc.* **2009**, 131, 3281-3290.
7. Plimpton, S. *J. Comput. Phys.* **1995**, 117, 1-19.
8. Paul, W.; Yoon, D. Y.; Smith, G. D. *The Journal of chemical physics* **1995**, 103, 1702-1709.
9. Schapotschnikow, P.; Huis, M. A.; Zandbergen, H. W.; Vanmaekelbergh, D.; Vlugt, T. J. *Nano Lett.* **2010**, 10, 3966-3971.

APPENDIX C

SUPPLEMENTARY INFORMATION: μ -RAINBOW: CdSe NANOCRYSTAL PHOTOLUMINESCENCE GRADIENTS VIA LASER SPIKE ANNEALING FOR KINETIC INVESTIGATIONS AND TUNABLE DEVICE DESIGN

C.1 Advice to Students

Prof. Thompson's CO₂ laser is really cool and fun to do experiments with. Thanks to Bob Bell's and Alan Jacobs' hard work characterizing the laser and developing the single scan LSA experimental method, we can get a ton of information from a single laser scan. My general experimental procedure when doing ssLSA on a new film was to make a large sample and anneal it for several dwell times at peak temperatures that I thought were likely to completely decompose the film, 1000 °C is a good starting point.

Then, after the experiment you can look at the width of the region that has been blown off of the substrate to get a rough idea of how high a temperature your film can withstand. Alan Jacobs has put together some very useful Genplot macros that will convert the full width of a region to the temperature at that point. I would then run a second set of experiments with the peak temperature set to what you think the decomposition temperature is for each dwell time of interest. Then, you can go on and do the high resolution spatial characterization to take advantage of the laser annealed stripes. One last note, be sure to calculate the thermal diffusion length for whatever film it is you plan to anneal at the dwell times you are interested in.

C.2 Materials and Methods.

Materials

Cadmium oxide (CdO_2), trioctylphosphine oxide (TOPO), octadecylphosphonic acid (ODPA), ethanol, hexane, toluene, and selenium powder were purchased from Sigma Aldrich. Trioctylphosphine (TOP) was purchased from Strem Chemicals. All chemicals were used without further purification.

NC synthesis and thin film preparation

CdSe NC synthesis followed a previously published procedure from Carbone *et al*¹. For the NC absorbing at 535 nm studied in the main text, 60 mg of CdO, 280 mg ODPA, and 3 g TOPO were added to a three neck flask. The solution was degassed under vacuum at 150 °C for an hour. The solution was heated above 300 °C under nitrogen and 1.5g of TOP was injected into the flask. Finally the solution was heated to the injection temperature of 380 °C and 450 ul of 1.7 M TOP:Se, from a stock solution made in a nitrogen glovebox, was injected. The reaction solution was immediately removed from heat. When the solution cooled to 160 °C, it was quenched by injecting 10 ml of toluene. The particles were washed 3 times using ethanol/hexane as the solvent/antisolvent pair and stored in a nitrogen glovebox until used.

NC films for laser annealing were produced by spincoating a 20 mg/ml solution of particles in hexane at 2000 rpm for 30s. Substrates were cleaned via sonication in acetone and isopropanol for 5 min each followed by 10 min of UV ozone treatment.

Characterization

Absorption measurements were performed using a Cary 5000 UV-vis spectrometer. Photoluminescence mapping was performed using a Renishaw InVia confocal Raman microscope. The NCs were excited by a 488 nm laser with a maximum power of 5 mW. Scanning electron microscopy was performed using a LEO 1550 FESEM with a working distance of 3 mm and an accelerating voltage of 5 kV.

Laser annealing

In laser spike annealing (LSA), a continuous wave CO₂ laser ($\lambda=10.6 \mu\text{m}$) focused to 2D Gaussian line beam ($\sim 80 \mu\text{m}$ by $500 \mu\text{m}$) that is scanned across the sample. The infrared laser is absorbed by a highly doped ($.01\text{-}.02 \Omega\text{-cm}$) silicon substrate, which conducts heat into the NC film. Scanning the laser beam across the sample leads to rapid heating as the laser approaches, followed by rapid cooling into the substrate after the laser passes. The duration of the heating, termed the dwell time, is defined as the ratio of the short axis FWHM to the scanning velocity. Dwells from $250 \mu\text{s}$ to 2ms were used in this work. The spatial and temporal temperature profiles were determined using thin film thermistors calibrated to gold and silicon melt temperatures.²

C.3 Photoluminescence Sizing Curve

In order to relate the PL emission wavelength to the diameter of laser annealed NCs, we aggregated reports of PL emission from CdSe NCs synthesized under similar reaction conditions. The data is presented in Table S1. We use a third order polynomial fit to the data in order to generate the empirical PL sizing curve which is used throughout the work.

PL Peak	NC Size	Reference
675	8.7	3
590	3.4	4
502	2.1	5
504	2.1	5
530	2.4	5
539	2.6	5
546	2.7	5
554	2.9	5
561	3.1	5
571	3.3	5
574	3.4	5
579	3.5	5
593	3.6	5
608	4.3	5
611	4.4	5
614	4.6	5
617	4.7	5
620	4.8	5
555	2.9	6
533	2.7	7
630	5.5	8

627	5.5	9
515	2.5	10
584	3.5	10
637	6	10
570	3.2	11
620	5	12

Table C.1: CdSe NC PL and diameter data from a survey of the literature and used to generate a PL sizing curve for CdSe NCs.

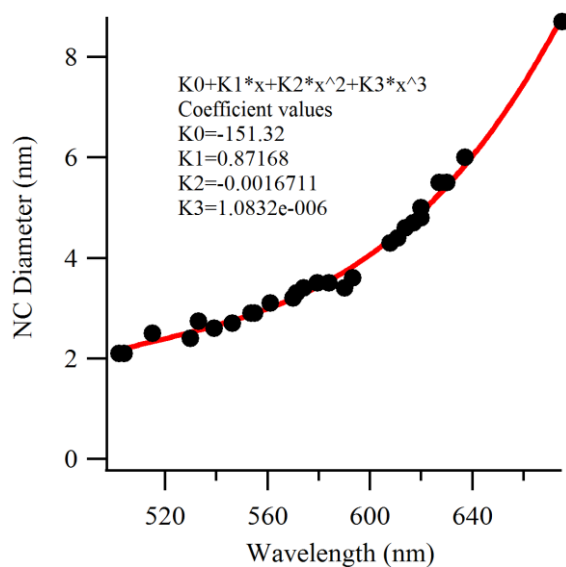


Figure C.1: Aggregated Photoluminescence peak position and NC diameter data used to generate an empirical PL based NC sizing curve.

C.4 Laser Stripe Annealing of Larger CdSe NCs

We performed laser stripe annealing on 4.1 nm CdSe particles in order to confirm that the NC sintering behavior discussed in the main text is typical for CdSe

NCs. Annealing a film with a dwell time of 2 ms and a peak temperature of 890C, matching the conditions of Figure 2 in the text, results in gradients in PL emission that show the same features as the 2.8 nm particles.

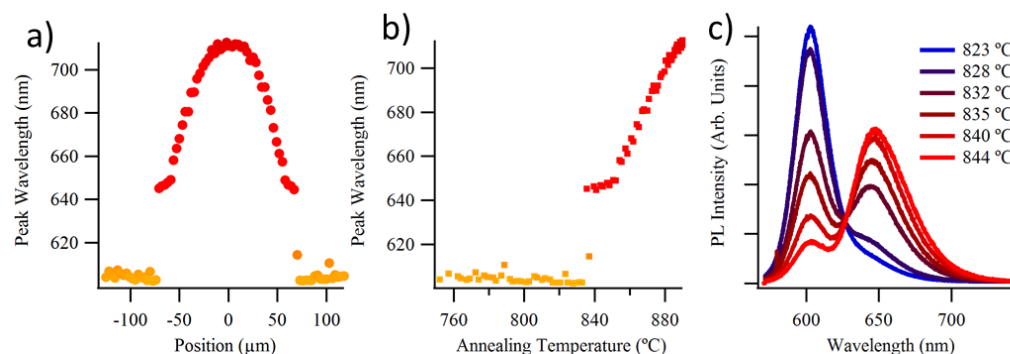


Figure C.2: a) Peak PL wavelength across a laser annealed stripe. b) Peak PL wavelength as a function of annealing temperature. c) Full PL spectra show a quantized transition between two NC populations as discussed in the main text.

C.5 Calculation of Thermal Diffusion Length

In order to confirm that the entire NC film experiences the same time-temperature profile, we estimate the thermal diffusion length following the work of Ong *et al*¹³. The thermal diffusivity, α , can be calculated using equation C.1.

$$\alpha = \frac{k}{(\rho c_p)_{avg}} \quad \text{Eq. C.1}$$

Where k is the thermal conductivity, measured by Ong to be 0.15 W/mK for ~3 nm CdSe NCs, and (ρc_p) is averaged based on the volume fraction of CdSe NCs in a film. Based on observed interparticle spacing of 4.5 nm in TEM and SEM we estimate that the NC occupy 15% of the volume of the film, assuming a random close packed film,

with the remaining space occupied by ODPa and TOPO molecules. This produces an average volumetric heat capacity, (ρc_p) of $2 \cdot 10^6 \text{ J/m}^3\text{K}$. The resulting thermal diffusivity is $7 \cdot 10^{-4} \text{ cm}^2/\text{s}$. For a characteristic heating time of $100 \mu\text{s}$ ($\sim 1\%$ of the dwell time), the thermal diffusion length is substantially greater than the $\sim 100 \text{ nm}$ film thickness. Indeed, the characteristic heating time for the 100 nm thin film is only 35 ns .

Complete data set for kinetic analysis of NC fusion

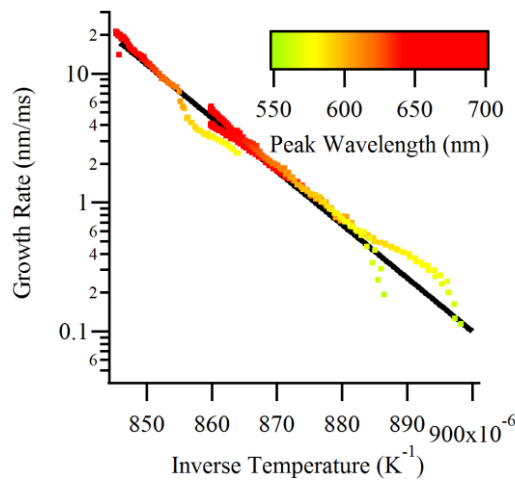


Figure C.3: A plot of NC growth rate against inverse peak annealing temperature containing all of the data points shown in Figure 3a.

C.6 Calculation of Emission Position for a Partially Fused Dimer

The expected PL emission for a partially fused dimer particle was calculated using the framework developed by Huges *et al*¹⁴ using values calculated by Shabaev *et al*.¹⁵ The change in ground state energy level, E_0 , due to overlap of the wavefunctions of a partially fused dimer is calculated using equation C.2.

$$\Delta E = 2t_m(U_0, a) \left[1 + \frac{m(U_0 - E_0)a^2}{h^2} \right] \quad \text{Eq. C.2}$$

Where t_m is the overlap integral between two CdSe QDs in contact with each other, a is the NC radius, m is the free electron mass, U_o is the confining potential, taken to be 1 eV, d is the spatial overlap between wavefunctions. It can be calculated exactly for cubic NCs, but here we use the empirical relationship found by Huges *et al*, equation C.3, in order to account for the quasi-spherical spherical shape of CdSe NCs.

$$d = \beta a + \gamma \quad \text{Eq. C.3}$$

Where $\beta = .16$ nm and $\gamma = .24$ nm for the quasi-spherical NCs studied.

This model predicts a 70 meV shift in the ground state energy level for particles that “just touch”. In our PL data we see a quantized transition from emission at 545 nm to 580 nm, a change of 140 meV that matches the expected PL emission of a completely fused, spherical dimer.

C.7 Second Quantized Fusion Step

In Figure 3a, the second sharp jump in the PL emission-temperature trace for a dwell time of 250 μ s suggests another quantized NC fusion event. Compared to the transition from monomer to dimer emission, the second quantized transition is less clear. The PL attributable to the dimer population decreases, and a peak appears corresponding to NCs with a total volume of 4 ‘monomer’ particles, *i.e.*, ‘tetramers’. The 1-2-4 pattern of NC fusion has been observed previously for Au NCs during HRTEM studies¹⁶. The PL signature for the dimer-tetramer transition is less clear for two reasons. First, as noted in the text, due to FRET in NC films PL is a measure of the largest NCs in the ensemble rather than an average. Fusion from monomers into dimers leads to a less uniform film where the precise local NC population will effect both the PL emission and subsequent

fusion events. In addition, for larger CdSe NCs, the change in emission wavelength with increasing radius is smaller resulting in greater overlap between the emission between the discreet NC populations. A video of the changing spectra across a NC stripe is included in the electronic SI of the Nanoletters article¹⁷, and makes the second quantized fusion event, as well as transition between quantized and continuous PL shift clear.

C.8 Photoluminescence Intensity

Unlike the PL peak position, the PL intensity across the laser annealed stripes does not show a simple trend. Figure S4b shows the total PL emission across a 2 ms dwell time, 890 C peak temperature annealing stripe. The green bars indicate the standard deviation in intensity based on 6 separate measurements. For comparison, Figure S3a shows the PL peak position similarly averaged across 6 measurements. There is significantly more deviation in the PL intensity, which we attribute to non-uniformity in the spincoated NC film.

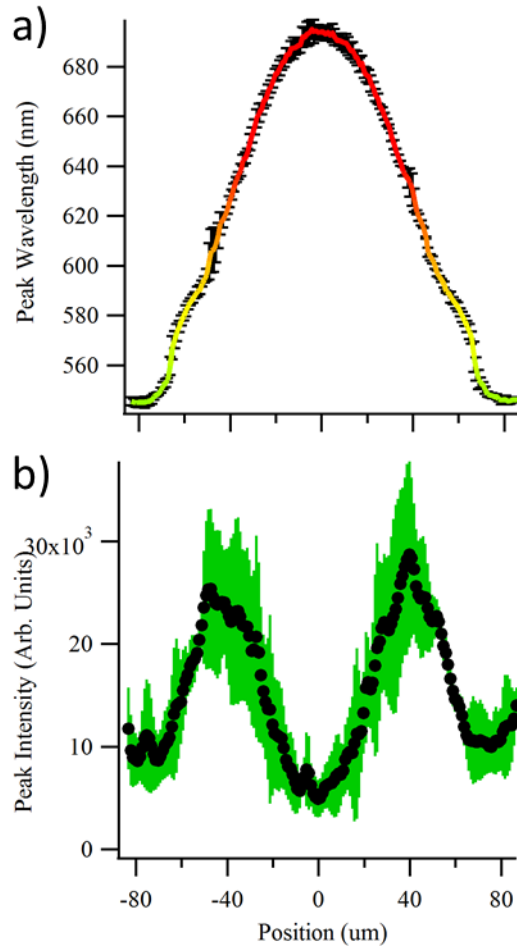


Figure C.4: a) Peak PL wavelength across a laser stripe. Black error bars indicate one standard deviation. B) Peak PL intensity across a laser stripe. Green error bars indicate one standard deviation.

The PL intensity detected by the Raman microscope can be described by

equation C.4

$$PL\ Intensity = \eta_{Detector} \phi_{photon} (1 - \exp(-\alpha t)) QY \quad \text{Eq C.4}$$

Where η is the detector efficiency, ϕ is the photon flux, α is the absorption coefficient at the excitation wavelength of 488 nm, t is the film thickness, and QY is the quantum yield of the emitting NCs. The change in detector efficiency across the range of wavelengths could only account for up to a 30% relative increase in detected PL. The

laser intensity, and hence photon flux is constant throughout the measurement. Given the sensitivity of NC to surface passivation, increased quantum yield after degradation of the ligand shell and fusion of NCs seems unlikely. The most likely reason for the initial increase in PL intensity is increased absorption of the laser resulting from a changing local dielectric constant and a change in the NC bandgap. The decrease in PL for the highest annealing temperatures (the center of the stripe) is likely due to ablation of NCs during laser annealing as a result of the decomposition of the organic ligands. Both the mechanism for increased PL emission, as well as film loss due to ablation during laser annealing will require further investigation to address more fully.

REFERENCES

1. Carbone, L.; Nobile, C.; De Giorgi, M.; Sala, F. D.; Morello, G.; Pompa, P.; Hytch, M.; Snoeck, E.; Fiore, A.; Franchini, I. R.; Nadasan, M.; Silvestre, A. F.; Chiodo, L.; Kudera, S.; Cingolani, R.; Krahn, R.; Manna, L. *Nano Lett.* **2007**, *7*, 2942-2950.
2. Iyengar, K.; Jung, B.; Willemann, M.; Clancy, P.; Thompson, M. O. *Appl. Phys. Lett.* **2012**, *100*, -.
3. Shevchenko, E. V.; Ringler, M.; Schwemer, A.; Talapin, D. V.; Klar, T. A.; Rogach, A. L.; Feldmann, J.; Alivisatos, A. P. *J. Am. Chem. Soc.* **2008**, *130*, 3274-3275.
4. Wuister, S. F.; de Mello Donegá, C.; Meijerink, A. *The Journal of Physical Chemistry B* **2004**, *108*, 17393-17397.
5. Peng, X.; Wickham, J.; Alivisatos, A. P. *J. Am. Chem. Soc.* **1998**, *120*, 5343-5344.
6. Munro, A. M.; Jen-La Plante, I.; Ng, M. S.; Ginger, D. S. *The Journal of Physical Chemistry C* **2007**, *111*, 6220-6227.
7. Landes, C.; Burda, C.; Braun, M.; El-Sayed, M. A. *The Journal of Physical Chemistry B* **2001**, *105*, 2981-2986.
8. Lu, N.; Chen, X.; Molenda, D.; Naber, A.; Fuchs, H.; Talapin, D. V.; Weller, H.; Müller, J.; Lupton, J. M.; Feldmann, J.; Rogach, A. L.; Chi, L. *Nano Lett.* **2004**, *4*, 885-888.
9. Chan, Y.-H.; Chen, J.; Liu, Q.; Wark, S. E.; Son, D. H.; Batteas, J. D. *Anal. Chem.* **2010**, *82*, 3671-3678.
10. Chen, W.; Joly, A. G.; McCready, D. E. *The Journal of Chemical Physics* **2005**, *122*, 224708.
11. Zhang, Q.; Xu, T.; Butterfield, D.; Misner, M. J.; Ryu, D. Y.; Emrick, T.; Russell, T. P. *Nano Lett.* **2005**, *5*, 357-361.
12. Okamoto, K.; Vyawahare, S.; Scherer, A. *J. Opt. Soc. Am. B* **2006**, *23*, 1674-1678.
13. Ong, W.; Rupich, S. M.; Talapin, D. V.; McGaughey, A. J.; Malen, J. A. *Nature Materials* **2013**, *12*, 410-415.
14. Hughes, B. K.; Blackburn, J. L.; Kroupa, D.; Shabaev, A.; Erwin, S. C.; Efros, A. L.; Nozik, A. J.; Luther, J. M.; Beard, M. C. *J. Am. Chem. Soc.* **2014**, *136*, 4670-4679.
15. Shabaev, A.; Efros, A. L.; Efros, A. L. *Nano Lett.* **2013**, *13*, 5454-5461.
16. Chen, Y.; Palmer, R. E.; Wilcoxon, J. P. *Langmuir* **2006**, *22*, 2851-2855.
17. Treml, B. E.; Jacobs, A. G.; Bell, R. T.; Thompson, M. O.; Hanrath, T. *Nano Lett.* **2015**.

APPENDIX D

SUPPLEMENTARY INFORMATION FOR: SIMULTANEOUS LIGAND AND CATION EXCHANGE IN PbSe/CdSe NANOCRYSTAL FILMS

D.1 Advice to Students

The surface chemistry of nanocrystals is both very complicated, and very important. Surface passivation during or after ligand exchange is critical for producing useful NC films, especially if you want to integrate them into devices. Given that the transport mechanism in these films is FRET, exchange with CdAc only is probably not sufficient for making PV devices, although as mentioned in the text it may be useful for LEDs. I think CdAc treatment may be useful in a hybrid passivation scheme, where CdAc and another ligand, such as TBAI are in the same solution. That mixture would hopefully lead to closer interparticle spacing while passivating the film via two different ionic species.

Photoluminescence is a very powerful characterization technique for NC films. Often, when we want to test the properties of our NC films, we have to put it into a device of some sort, FET, solar cell, etc. This can often be frustrating as you have to develop a good procedure for controlling the additional components of these devices so that you can be confident that the changes in performance you see are due to the changes in your NC film. In contrast, PL and TRPL can directly give you information about the surface passivation and transport in a NC film. The use of “artificial traps”, as developed by Sargent and used in this work, is especially useful for characterizing the diffusion length of excitons in NC films¹.

D.2 Materials and Methods

Materials

Lead oxide (99.99%), selenium (99.999%, powder), trioctylphosphine (90%, technical grade), oleic acid (OA 70%, technical grade), 1-octadecene (ODE 90%), diphenylphosphine (98%), and anhydrous ethanol (200 proof) were all purchased from Sigma-Aldrich. Cadmium acetate dihydrate(99.999%) was purchased from Alfa Aesar. All chemicals were used without further purification.

NC synthesis and film formation

PbSe NCs were prepared by using a modified procedure adopted from the method of Yu e al². In a typical synthesis, a 50 mL three-neck flask was loaded with 892 mg of PbO, 3.2 g of oleic acid, and 15.5 g of 1-octadecene and heated to 120 °C under vacuum with stirring for 1.5 h until the solution was transparent and colorless. The lead oleate precursor was transferred into a septa-capped vial and purged with nitrogen for 1 h at 150 °C before transferring into a glovebox for the remainder of the synthesis. Lead oleate (3 mL) was introduced into a 20 mL vial and heated to 100 °C for 15 min on a hot plate. In a separate vial, 750 µL of 1.25 M selenium in tri-n-octylphosphine was mixed thoroughly with 15 µL of diphenylphosphine and loaded into a syringe. When the lead oleate solution reached injection temperature, the selenium precursor was swiftly injected into the vial. Injection temperatures and reaction times were varied to tune the NCs to the desired size. To quench the reaction, the vial was immediately submerged into a cold ethanol bath and injected with 3.5 mL of anhydrous ethanol to arrest the NC annealing. The NCs were isolated from the crude solution by

centrifugation and precipitated twice more with toluene/acetonitrile as the solvent/antisolvent pair.

Sample Preparation and Ligand Exchange

NC films were prepared by spincoating a 20 mg/ml solution of NCs at 2000 rpm for 30s onto glass slides for optical absorption and PL measurements. Cation/Ligand exchange was performed by submerging a NC film into a 20 mM solution of Cadmium acetate in ethanol for 30 s followed by a 30 s rinse in ethanol. Mixed NC films were prepared by mixing two stock NC solutions together in an appropriate ratio. The molar concentration of NC solutions was determined following the procedure detailed by Moreels et al³. All processing was performed in a nitrogen glovebox to avoid oxidation.

Characterization

Optical absorption measurements were collected with a Cary 5000 UV-Vis-NIR spectrometer. TEM images were acquired using a FEI Tecnai T12 at 120 kV. GISAXS was performed at the D1 beamline of the Cornell High Energy Synchrotron Source (CHESS) using monochromatic radiation of wavelength 1.161 Å and a bandwidth $\Delta\lambda/\lambda = 1.5\%$. The X-ray beam was produced by a hardbent dipole magnet of the Cornell storage ring and monochromatized with Mo:B4C synthetic multilayers with a period of 30 Å. GISAXS images were collected by a MedOptics fiber coupled CCD camera with a pixel size of 46.9 μm by 46.9 μm and a total of 1024 by 1024 pixels with 14-bit dynamical range per pixel. The sample to detector distance was 900 mm, as calibrated by a silver behenate powder standard. Images were dark current corrected, distortion corrected, and flat field corrected by the acquisition software. The incident angle of the X-ray beam was 0.25°. Scattering images were calibrated using the Fit2D software[31]

The photoluminescence was measured using a home-built spectrophotometer. In the continuous measurement, a 638 nm diode laser with typical intensity of 30 mW/cm² was used for excitation. In the PL lifetime measurement, a pulse train of 1 kHz repetition rate, 800 nm wavelength, and <1 ps pulse duration was used as the excitation source. The emitted light was collected, passed through a monochromator for wavelength filtering, and then temporally resolved using a fast InGaAs photomultiplier detector, with the temporal resolution of 1 ns.

D.3 Composition of NC Film after Cation Exchange

In order to confirm our interpretation of the blueshift in absorption and PL emission as cation exchange rather than oxidation, we performed energy dispersive X-ray spectroscopy (EDX) in a LEO 1550 SEM. The EDX spectra before and after cation exchange are shown in Figure D.1. Clearly, after cation exchange a Cd signal appears in the spectra. Elemental quantification indicates that after cation exchange 23% +/- 2% of the cations are Cd. For the NC model shown in Figure 2a of the text, this corresponds to exchange of approximately half of the surface cations in agreement with the blueshift in the NC film absorption measurements. The full results from the quantification are shown in Table S1.

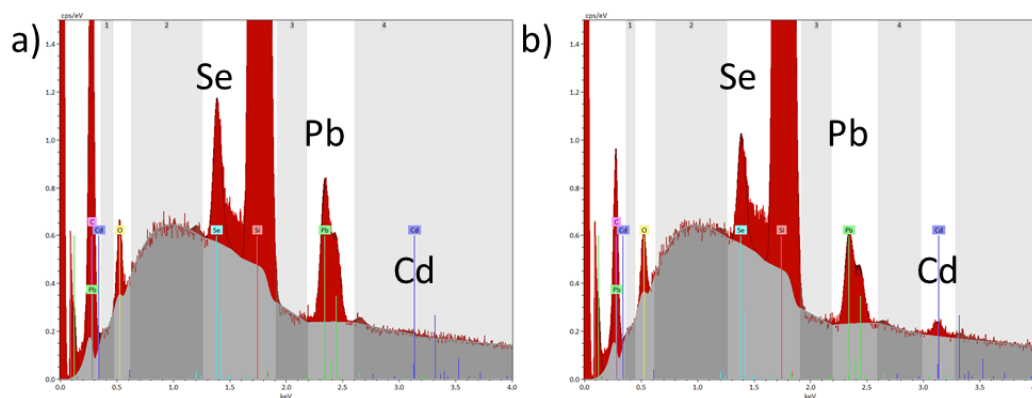


Figure D.1: EDX spectra of NC film a) Oleic acid passivated film b) Cd-acetate passivated film. The grey shading indicates the background subtraction used for quantification.

	OA		CdAc	
Element	at. %	error in at. %	at. %	error in at. %
Carbon	29.10473	3.940793	11.95444	1.847847
Oxygen	1.250058	0.252093	1.200778	0.249264
Silicon	68.72263	3.040171	85.94606	3.676394
Selenium	0.330964	0.025203	0.30066	0.024069
Cadmium	0.012052	0.006423	0.139615	0.011973
Lead	0.579559	0.025819	0.458446	0.021004
Sum	100		100	

Table D.1: Quantification of the composition of Oleic acid passivated and Cd-acetate passivated films

D.4 Kinetics of Cation Exchange

We investigated the tunability of the cation exchange during CdAc treatment by varying the temperature and time of CdAc treatment. It appears that the cation exchange saturates at approximately half a monolayer at room temperature, indicating some surface cations are too well bonded to be exchanged at room temperature. In contrast, as the temperature of the CdAc solution is increased, the degree of cation exchange is increased, showing that addition thermal energy can allow these previously inaccessible cation sites to become active and undergo Cd-for-Pb exchange. These results are consistent with studies of cation exchange in solution that indicate that cation exchange

can saturate at low temperatures even after 19 hours of exchange whereas higher temperatures can lead to significant exchange in only one hour.⁴

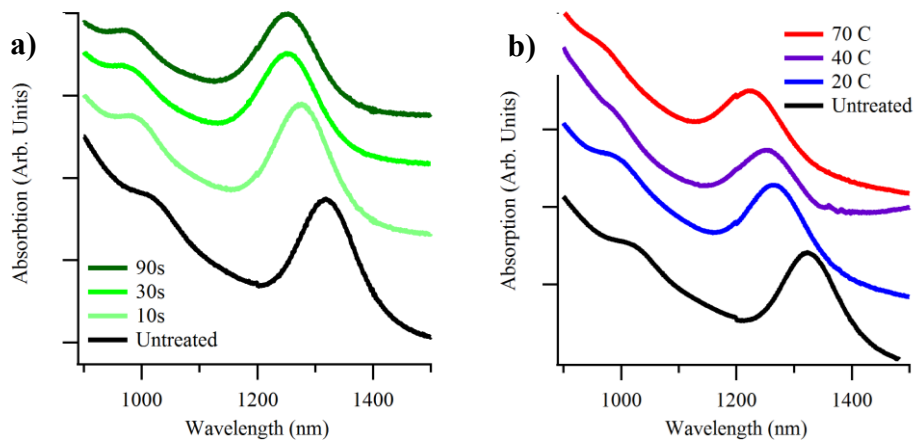


Figure D.2: Time and Temperature dependence of cation exchange

D.5 Transport of Excitons in Mixed Films

As the donor/acceptor films used in FRET measurements are almost entirely (100:1 ratio) smaller donor particles, essentially all of the excitons are generated in the donor particles. Assuming an equal quantum yield from donor and acceptor, we can use the percentage of PL emission from the acceptor particles to estimate the distance over which exciton transport occurs. As a simple model of the film, we assume the acceptors are uniformly spaced at the center of a simple cubic lattice. In order to generate the 100:1 particle ratio, the cubes must have an edge length of 4.6 particles. If we assume that acceptor particles collect all excitons generated within a sphere of radius R centered on the acceptors, we can find an exciton transport length for OA and CdAc films by finding the radius of a sphere which encapsulates the same fraction of the unit cell as the fraction of PL emission attributed from the acceptors. For OA films, we find

R=2.3 NC. After CdAc treatment R increases to 2.8 NC, presumably due to the increased FRET rate after ligand removal. Given the strong dependence of energy transfer rate on interparticle spacing, it is likely that the energy transfer does not occur in one long jump, but rather through a series of hops downhill in energy until the exciton reaches the local potential energy minimum of the acceptor particles⁵.

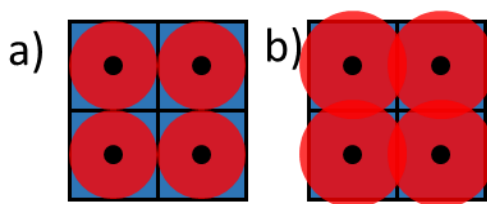


Figure D.3: A 2D model of collection of excitons by acceptor particles. Red circles indicate the region in which excitons generated in the donor film are collected by the acceptors, the blue region indicates the region where excitons are not collected. The size of the unit cells and circles match

D.6 Change in Förster Radius Following Cation/Ligand Exchange

The Förster energy transfer rate can be calculated by equation D.1⁶.

$$k_{FRET} = \frac{9000\kappa^2 \ln(10)}{128\pi^6 n^4 N_A \tau_d R^6} \int_0^\infty E_d(\nu) \epsilon_a(\nu) \frac{d\nu}{\nu^4} \quad \text{Eq. D.1}$$

Where κ^2 is an orientation factor taken to be 2/3 for randomly oriented dipoles, N_A is Avagadro's number, τ_d is the radiative lifetime of the donor, $E_d(\nu)$ is the normalized emission spectra of the donor, and $\epsilon_a(\nu)$ is the molar extinction coefficient of the acceptor. In order to correctly attribute the change in FRET transfer rate to decreased interparticle spacing, we must account for any changes in other terms in the expression. Specifically, in a system where the quantum yield, donor emission, and acceptor absorption all change after CdAc treatment, the donor lifetime and overlap integral must

be investigated. From Figure 5b in the main text, we can see that the initial decay for the acceptor particles before and after treatment does not change and that PL decay is essentially unchanged for the first 2 μ s. If we assume that the same is true for the donor particles, then it is likely that the radiative lifetime is constant. We calculate the overlap integrals before and after cation/ligand exchange using the donor emission and acceptor absorption profiles shown in Figure D.4, which come from measurements of single component films. We find only a 5% increase in overlap integral after cation/ligand exchange, indicating that the \sim 4 fold increase in FRET transfer rate is mainly due to increased interparticle spacing.

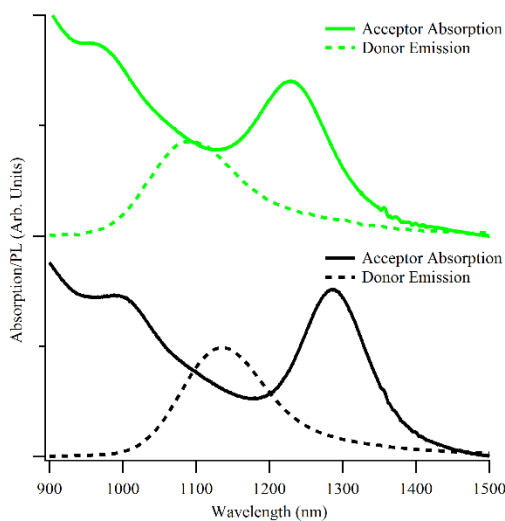


Figure D.4: Donor Emission and Acceptor Absorption used to calculate the overlap integral.

D.7 Cation/Ligand Exchange with Other Cations

In addition to the detailed analysis of CdAc treated films, we have also investigated cation/ligand exchange with other cations. In Figure D.5, we see that for Tin (II) acetate (SnAc) and Cu(II) acetate (CuAc) the excitonic absorption peak is

completely lost, indicating that a complete cation exchange occurs during the 30s cation/ligand exchange treatment. In contrast, with Zinc (II) acetate (ZnAc) only a slight redshift and broadening of the excitonic peak occurs. We attribute this redshift to limited ligand removal by the ethanol solvent. The differences in cation exchange behavior can be qualitatively explained by Hard/Soft Acid and Base interactions. Se anions are a soft base, while ethanol is a hard solvent. As a result, cation exchange will be favorable for cations that are softer than Pb and unfavorable for harder cations. The qualitative ranking of divalent cations is $\text{Ca}^{2+} > \text{Ni}^{2+} > \text{Zn}^{2+} > \text{Cd}^{2+} > \text{Pb}^{2+} > \text{Sn}^{2+} > \text{Cu}^{2+} > \text{Hg}^{2+}$ which correlates well with the observed cation exchange⁷.

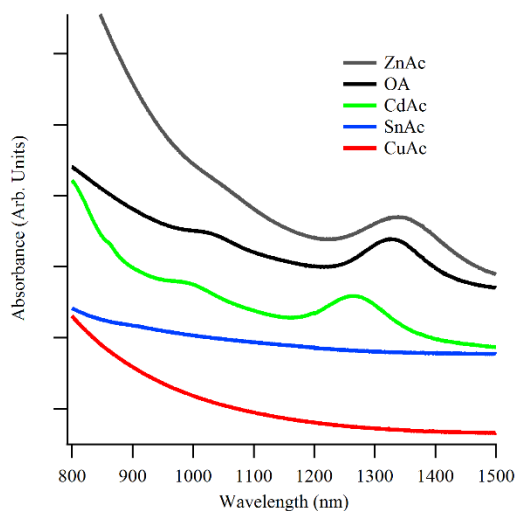


Figure D.5: Cation exchange with other cations. Exchange can be explained by Pearson Hard/Soft Acid/Base theory.

REFERENCES

1. Zhitomirsky, D.; Voznyy, O.; Hoogland, S.; Sargent, E. H. *ACS Nano* **2013**, *7*, 5282-5290.
2. Yu, W. W.; Falkner, J. C.; Shih, B. S.; Colvin, V. L. *Chem. Mater.* **2004**, *16*, 3318-3322.
3. Moreels, I.; Lambert, K.; De Muynck, D.; Vanhaecke, F.; Poelman, D.; Martins, J. C.; Allan, G.; Hens, Z. *Chem. Mater.* **2007**, *19*, 6101-6106.
4. Pietryga, J. M.; Werder, D. J.; Williams, D. J.; Casson, J. L.; Schaller, R. D.; Klimov, V. I.; Hollingsworth, J. A. *J. Am. Chem. Soc.* **2008**, *130*, 4879-4885.
5. Akselrod, G. M.; Prins, F.; Poulikakos, L. V.; Lee, E. M. Y.; Weidman, M. C.; Mork, A. J.; Willard, A. P.; Bulović, V.; Tisdale, W. A. *Nano Lett.* **2014**, *14*, 3556-3562.
6. Forster, T. *Discuss. Faraday Soc.* **1959**, *27*, 7-17.
7. Pearson, R. G. *J. Am. Chem. Soc.* **1963**, *85*, 3533-3539.

APPENDIX E

SUPPLEMENTARY INFORMATION FOR: SUCCESSIVE IONIC LAYER ABSORPTION AND REACTION FOR POST-ASSEMBLY CONTROL OVER INORGANIC BONDS IN LONG RANGE ORDERED NANOCRYSTAL FILMS

E.1 Advice for Students

Each set of NCs used for making CBCs is different. While a concentration of 5 μM is generally a good starting point, you may need to adjust this by a factor of 5 in either direction for a specific batch of particles. This shouldn't be surprising, as 8 nm particles have a correctional area 4X higher than 4 nm particles.

As I mentioned in the future work and conclusions section, I think CBCs are a really interesting and promising material that I think will make great strides in the future. As can be seen from the transport data in this paper, and presented below, the SILAR film growth procedure detailed here produces degenerately doped, metallic p-type films. While this may be interesting for thermoelectric applications, or to show delocalization due to high carrier concentrations as predicted recently¹, I think that if these films are to be integrated into devices like solar cells and photodectors, such large doping will need to be avoided. I used 20 mM solutions for both the cation and anion solution, following previous papers. I think the best way to prevent the degenerate doping from the Se solution will be to reduce the concentration of both precursors, and use many more SILAR cycles. I believe that if each half cycle only adds a few atoms to the surface of a NC, then the corresponding half cycle may be more likely to effectively bond to the newly added ions preventing any drastic changes in stoichiometry. Another interesting way forward for CBCs may be to add a thermal annealing step. Annealing may allow surface atoms in the amorphous shell to diffuse and crystalize, forming more stable bonds that could reduce trapping.

E.2 Materials and Methods

Materials

Lead oxide (99.99%), selenium (99.999%, powder), trioctylphosphine (90%, technical grade), oleic acid (OA 70%, technical grade), 1-octadecene (ODE 90%), diphenylphosphine (98%), Sodium Borohydride (98.5%), Lead acetate trihydrate (99.99%), ethylene diamine, anhydrous ethylene glycol, and anhydrous ethanol (200 proof) were all purchased from Sigma-Aldrich. Cadmium acetate dihydrate(99.999%) was purchased from Alfa Aesar. All chemicals were used without further purification.

PbSe NC synthesis

PbSe NCs were prepared by using a modified procedure adopted from the method of Yu e al². In a typical synthesis, a 50 mL three-neck flask was loaded with 892 mg of PbO, 3.2 g of oleic acid, and 15.5 g of 1-octadecene and heated to 120 °C under vacuum with stirring for 1.5 h until the solution was transparent and colorless. The lead oleate precursor was transferred into a septa-capped vial and purged with nitrogen for 1 h at 150 °C before transferring into a glovebox for the remainder of the synthesis.

Lead oleate (3 mL) was introduced into a 20 mL vial and heated to 160 °C for 15 min on a hot plate. In a separate vial, 750 µL of 1.25 M selenium in tri-n-octylphosphine was mixed thoroughly with 15 µL of diphenylphosphine and loaded into a syringe. When the lead oleate solution reached injection temperature, the selenium precursor was swiftly injected into the vial and allowed to react for 5 minutes. Injection temperatures and reaction times can be varied to tune the NCs to the desired size. To quench the reaction, the vial was immediately submerged into a cold ethanol bath and injected with 3.5 mL of anhydrous ethanol to arrest the NC annealing. The NCs were

isolated from the crude solution by centrifugation and precipitated twice more with toluene/acetonitrile as the solvent/antisolvent pair.

Selenide Solution Synthesis

The solution of selenide ions used in SILAR film growth was prepared through reduction of selenium powder with NaBH_4 in ethanol in a 1:2 ratio of Se to NaBH_4 following established procedures³. A nominally .2 M solution was filtered through a μm filter and then diluted to a nominal concentration of 20 mM in ethanol for use. The solution exhibited a reddish brown color typical of polyselenides.

CBC Film Formation

Long range ordered, epitaxially connected NC films were produced through liquid interface assembly. 1 ml of anhydrous ethylene glycol was added to a 1 cm by 1 cm square trough. 20 μl of NC dissolved in hexane at a concentration of 5 μM was added to the surface of the ethylene glycol and the well was immediately covered using a glass slide. The molar concentration of a NC solution was determined using the empirical sizing curve and NC size independent molar absorption coefficient determined by Moreels *et al*⁴. The NC film was left to dry for 30 minutes. Then, 25 μl of ethylene diamine was injected into the ethylene glycol subphase. The NC film visibly contracts following injection of the ethylene diamine. After 5 minutes, samples were taken from the NC film using the Langmuir-Schaefer method, and excess ethylene glycol was rinsed off of the sample using acetonitrile.

SILAR Film Growth

For all SILAR film growth, solutions of 20 mM concentration for both the cationic and anionic solution were used. One SILAR cycle consisted of 30 s of exposure

to the Se solution, a 30 s rinse in clean ethanol, 30 s exposure to a cationic solution, and another rinse in clean ethanol. Films were allowed to dry for 30s between dips in solution. For TEM samples, TEM grids were directly dipped into the solutions. For absorbance and FET measurements, the samples were flooded with a solution for 30s before spincoating at 2000 RPM for 30s to remove the solution and dry the film.

Characterization

Optical absorption measurements were collected with a Cary 5000 UV-Vis-NIR spectrometer. Electrical characterization was performed on a home built probe station in a nitrogen glovebox using Keithley 2400 and Keithley 6430 source meters. Low resolution, brightfield TEM images were acquired using a FEI Tecnai T12 at 120 kV. HAADF STEM images were acquired on a NION superSTEM at an accelerating voltage of 60 keV. Lens aberrations were corrected up to and including fifth order, and an aperture size of 30 mrad was used.

E.3 Additional TEM Images

While the main text focuses on small regions of a CBC film in order to study the structural changes occurring to the inter NC epitaxial bonds during SILAR film growth, CBC films show uniformity over much larger areas. Figure E.1 contains additional, wider field of view TEM images that show a single CBC grain containing thousands of NCs, the selected area that produced the electron diffraction pattern inset in Figure 2b of the main text, also reproduced in Figure E.1d, and the uniformity of a CBC monolayer across a TEM grid. We believe the cracks observed in CBC films are artifacts of the Langmuir-Schaefer transfer method, as the CBC grain seems to be continuous across the cracks.

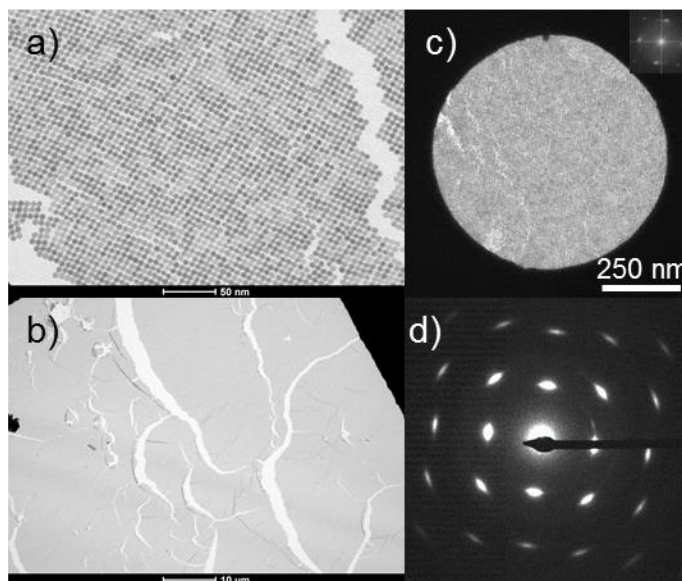


Figure E.1: Wider field of view images of CBCs showing a) a single CBC grain showing long range order over 100's of nm b) uniform monolayer across a TEM window c) TEM of the selected area aperture used to produce d) and inset into Figure 2b. Inset in c): FFT of the NC assembly in c

Figure E.2 shows the wider field of view HAADF STEM images used for automated particle analysis and quantification of the particle size, bond width, and connectivity in CBC films before and after SILAR exchange. Red circles indicate particles that the image analysis program has identified. The regions with partial multilayers in Figure E.2b were masked as shown in order to avoid inaccurate particle identification in those regions.

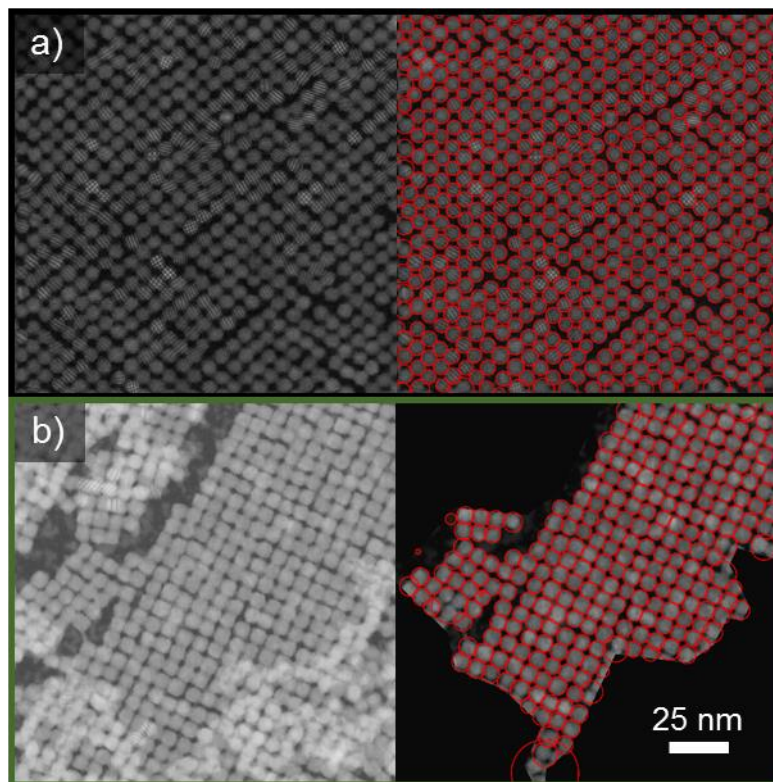


Figure E.2: Automated particle analysis of CBC films. a) Control CBC films b) CdSe SILAR treated films. The partial bilayers were masked to avoid inaccurate particle detection. All images are at the same scale.

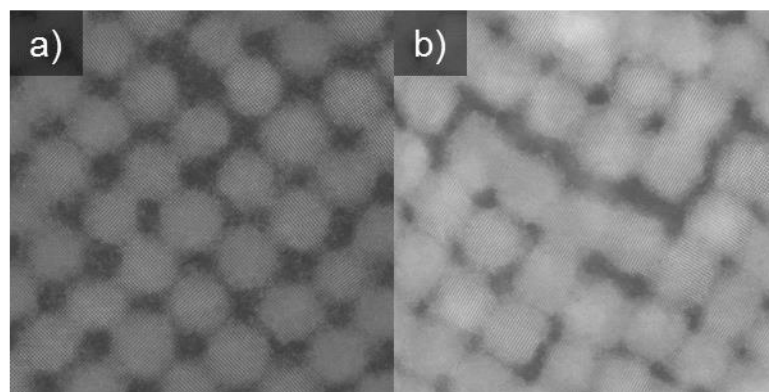


Figure E.3 Additional HAADF STEM images of a) control and b) CdSe SILAR monolayer films.

E.4 Details of EELS Analysis

Figure E.4 shows an example EELS spectrum. The background was fit over the blue region of 405-449 eV using the linear combination of power laws method and

oversampling with $\sigma=2$ pixels⁵. The Cd concentration was determined by integrating over the Cd-M_{4,5} edge from 460-493 eV, as shown by the tan window.

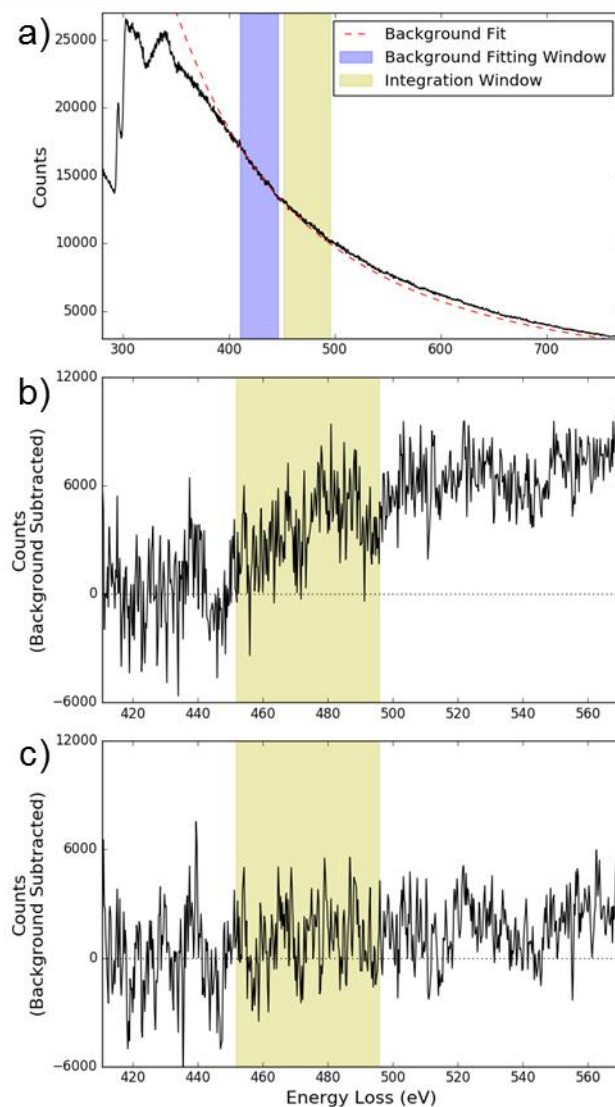


Figure E.4: a) Full EELS spectrum, blue indicates the background fitting window, tan indicates the window used for Cd quantification b) the background subtracted Cd-M_{4,5} edge on the particle. c) the same energy window off of the particle, showing no Cd signal

E.5 Transport in Se Terminated NC Films

In addition to the data presented in the main text, FET transport measurements, shown in Figure E.5, were also taken following Se treatment steps (ie half of a SILAR

cycle). This allowed us to attribute the initial sharp increase in both hole mobility and film conductance to the first Se treatment. Interestingly, as SILAR processing continued, there was a clear difference in the mobility of holes between cation terminated and anion terminated films while the conductance of the film increases nearly monotonically. While more experiments are required to conclusively determine the source of this behavior, we currently believe that Se terminated films have lower mobility due to an increased number of trap states originating from unpassivated Se states^{6,7}. During the cationic half of a SILAR cycle, the Pb cations bind to the surface Se atoms, passivating the surface and eliminating some of the surface trap states.

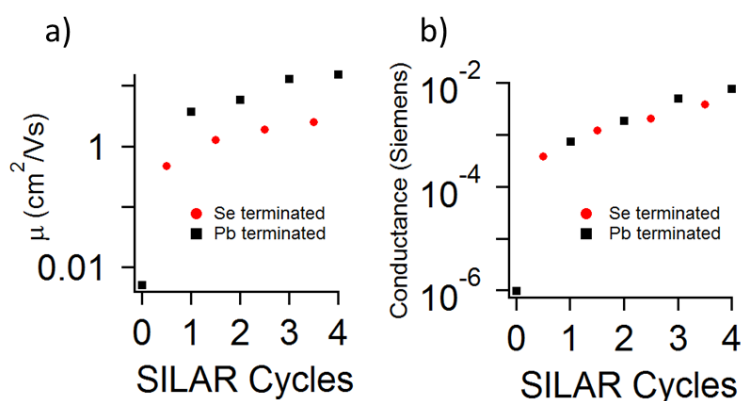


Figure E.5: a) Change in hole mobility with SILAR cycle and surface termination b) Change in film conductance with SILAR cycles and surface termination

The nearly monotonically increasing conductance leads to another question, if the mobility changes by over an order of magnitude depending upon the surface termination, why doesn't the conductance show similarly large swings? The conductance of a film can be expressed in Eq E.1.

$$G = \frac{A}{l} ne\mu \quad \text{Eq. E1}$$

Where G is the conductance, A is the cross-sectional area of the film, l is the channel width, n is the density of carriers, e is the elementary charge, and μ is the mobility of the carriers. If we assume that A and l are unchanged during a half of a SILAR cycle, and the mobility increases by an order of magnitude, the carrier density must decrease by about the same amount. The trap states created by unpassivated surface anions lie just above the valence band in lead chalcogenides⁷, and contribute to p-doping the material, when these anions are passivated, the doping level decreases even as the carrier mobility increases. Hall measurements of PbSe films with stoichiometric excess of Se have seen increasing hole concentration with increasing Se excess, which can be compensated through subsequent cation treatment^{8,9}.

REFERENCES

1. Chen, T.; Reich, K. V.; Kramer, N. J.; Fu, H.; Kortshagen, U. R.; Shklovskii, B. I. *Nat Mater* **2016**, 15, 299-303.
2. Yu, W. W.; Falkner, J. C.; Shih, B. S.; Colvin, V. L. *Chem. Mater.* **2004**, 16, 3318-3322.
3. Klayman, D. L.; Griffin, T. S. *J. Am. Chem. Soc.* **1973**, 95, 197-199.
4. Moreels, I.; Lambert, K.; De Muynck, D.; Vanhaecke, F.; Poelman, D.; Martins, J. C.; Allan, G.; Hens, Z. *Chem. Mater.* **2007**, 19, 6101-6106.
5. Cueva, P.; Hovden, R.; Mundy, J. A.; Xin, H. L.; Muller, D. A. *Microsc. Microanal.* **2012**, 18, 667-675.
6. Katsiev, K.; Ip, A. H.; Fischer, A.; Tanabe, I.; Zhang, X.; Kirmani, A. R.; Voznyy, O.; Rollny, L. R.; Chou, K. W.; Thon, S. M.; Carey, G. H.; Cui, X.; Amassian, A.; Dowben, P.; Sargent, E. H.; Bakr, O. M. *Adv. Mater.* **2014**, 26, 937-942.
7. Kim, D.; Kim, D.-H.; Lee, J.-H.; Grossman, J. C. *Phys. Rev. Lett.* **2013**, 110, 196802.
8. Oh, S. J.; Berry, N. E.; Choi, J.-H.; Gaubling, E. A.; Lin, H.; Paik, T.; Diroll, B. T.; Muramoto, S.; Murray, C. B.; Kagan, C. R. *Nano Lett.* **2014**.
9. Oh, S. J.; Berry, N. E.; Choi, J.-H.; Gaubling, E. A.; Paik, T.; Hong, S.-H.; Murray, C. B.; Kagan, C. R. *ACS nano* **2013**, 7, 2413-2421.

Appendix F

INCOMPLETE AND UNPUBLISHED EXPERIMENTS

Experiments fail. Throughout my graduate career, I have had many experiments, ideas, and things that I just wanted to try that either failed or were not interesting enough or did not show enough promise for me to continue pursuing the work. Rather than let all of this work sit buried in my lab notebook and computer hard drive I have included it here so that if someone had a similar idea, they can avoid repeating my mistakes. I consider this to be my scientific “blooper reel” so I suggest reading it with the Benny Hill theme music in the background.

I will try to be as clear as possible about the experiment, the rationale for pursuing it, and why I think it failed or I abandoned it. I will also provide some suggestions for ways to move forward with the work. If you are reading this and would like some more information beyond what I have included here, feel free to email me at btrem1 at outlook.com and I will try to help the best I can.

F.1 Nanoparticle Epitaxy

The ability to create long range ordered monolayer NC films via liquid interface assembly made me interested in producing novel 3° structures by stacking monolayers of NCs on top of each other. Because we can synthesize NC to be the same size with the same ligands, but a different core, I thought we could alternate NC of different compositions and see if any interesting collective properties emerged. I imagined that this would work like molecular beam epitaxy (MBE) except for nanoparticles, so I thought of it as nanoparticle epitaxy (NPE).

The first thing I tried was to stack two monolayers of the same NC on top of each other. While the Fe₂O₃ particles formed the same hexagonally close packed monolayer for both layers, they have an orientational misalignment between the layers,

as shown in Figure F.1a. To fix this, I tried solvent annealing the assembly, with the idea that the additional mobility provided by solvent annealing would allow particles in the top monolayer to align themselves with the bottom NC layer.

However, the rough approach to solvent annealing that I used, filling the moat in a vacuum flange with hexane while covering the sample to confine the hexane vapor, was likely too high of a hexane vapor concentration that lead to redissolution of the NCs and created large, thick multilayer NC islands as shown in Figure F.1b rather than the desired coherent bilayer.

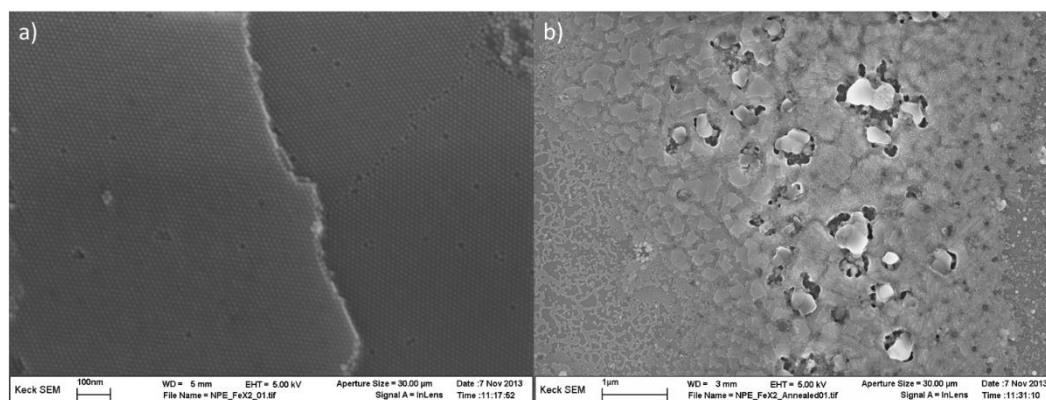


Figure F.1: a) Bilayer of NC showing misorientation between the layers. b) Film after solvent annealing, showing large supercrystals.

I think that this approach to creating unique 3° structures could still be successful. However, I think that much more precise control over the solvent vapor concentration would be required. I think the best way to do this experiment would be *in situ* at CHESS using Dr. Detlef Smilgies's solvent vapor chamber. You could then monitor the swelling and order in the film in real time. Detlef has some previous papers studying thin Langmuir-Blodgett films that would be helpful in determining when the multilayers begin to stack in an ordered, coherent fashion^{1, 2}.

F.2 Self-Striping Nanocrystal Inks

I became interested in 3D printing of NC, and in particular how to solve the problem of ligand removal. In addition to being critical for enabling conduction in NC films after deposition, it is critical that bottom layers of NCs do not redissolve when you go to print a new layer of NCs. My approach for this was to borrow a technique used by people who want to print highly conductive metal via inkjet printing and include a ligand stripping agent in the NC ink. As the solvent evaporates, the ligand stripping chemical will increase in concentration and eventually pull the ligands off the NCs³. The idea behind this experiment is detailed schematically in Figure F.2a.

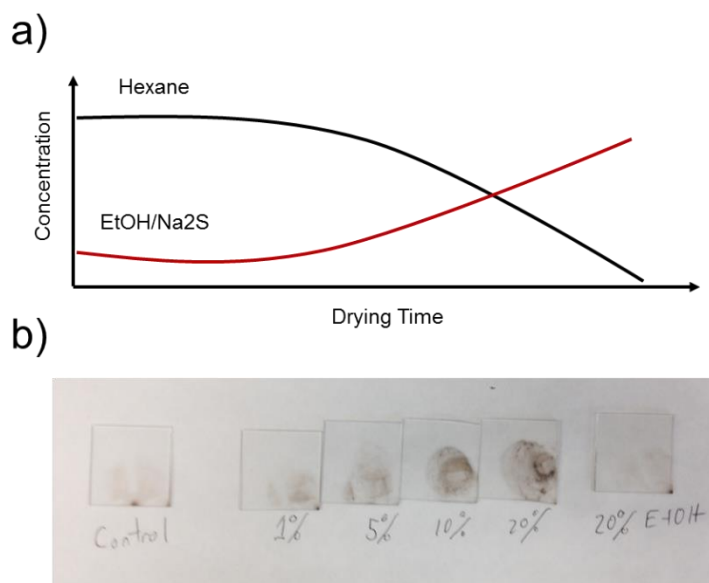


Figure F.2: a) Hypothesized concentration of hexane and ethanol during drying of the two phase NC ink. b) NC remaining on a glass slide following a rinse with hexane.

I used Na₂S dissolved in ethanol as the ligand removal agent. Hexane evaporates faster than ethanol, so the droplet of NC ink slowly transforms from NC in solution to crashed out particles undergoing ligand exchange. The results from a quick experiment

are shown in Figure F.2b. We see an increasing volume fraction of ligand stripping solution results in a larger fraction of particles remaining on the glass slide after a rinse with hexane. This experiment never went further as the development of a 3D printer for printing NC inks encountered issues with ink dispensing and wetting of the substrate by the NC ink. There have been other attempts at creating NC inks that are conductive without needing a ligand exchange step, such as NC with metal chalcogenide complex ligands^{4,5}. These sorts of NC inks may work for 3D printing applications without having to resort to the complicated two phase system I investigated.

F.3 Inductive Heating of Binary Nanocrystal Assemblies

In the summer of 2014, Ben Richards got an inductive heater for his nanowire growth research. I was working on nanothermite reactions between Al NCs and Fe₂O₃ NCs. Fe₂O₃ NCs are superparamagnetic, and so in a rapidly oscillating magnetic field the NCs are heated as a result of rapidly flipping the magnetic dipole. I was interested in using the inductive heater to ignite a nanothermite. As a first experiment, I used Fe₂O₃/PbSe binary mixtures as PbSe melts at relatively low temperatures. I hoped that this would provide me with an initial indication of if the Fe₂O₃ particles were coupling with the inductive heater. Figure F.3 shows a TEM grid after inductive heating. It seems that the Fe₂O₃ NC must have been heated somewhat, as there are clearly some PbSe particles that have fused together. The interesting observation for me is that in the areas that form an AB₂ BNSL, the PbSe NC are not fused because the larger Fe₂O₃ NCs keep the PbSe NC isolated.

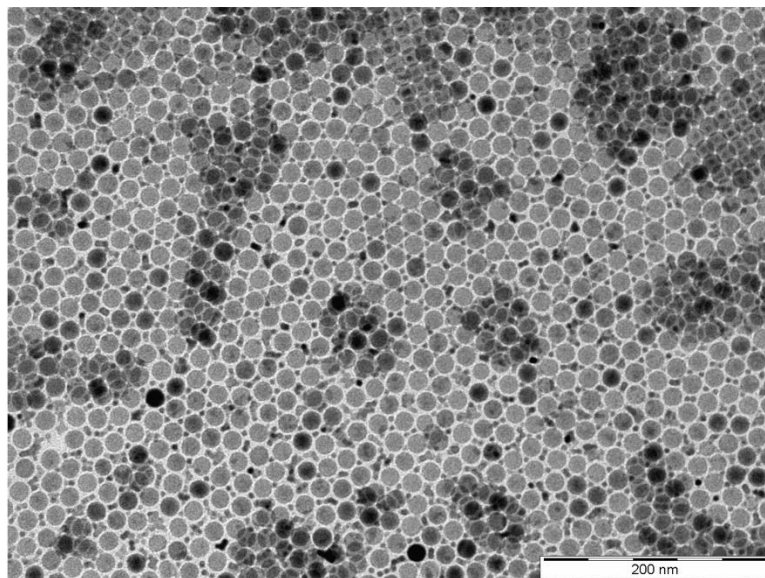


Figure F.3: $\text{Fe}_2\text{O}_3/\text{PbSe}$ BNSL after inductive heating to create local heating in the NC films. Isolated PbSe particles do not fuse, showing the enhanced thermal stability of BNSLs.

Given this positive initial result, I tried using the inductive heater to ignite a thermite reaction. I was never able to get this to work. I believe this is because of poor coupling between the Fe_2O_3 NC and the inductive heater. The characteristic time scale for flipping of a dipole in a magnetic NC is highly dependent on the size of the NC. Unfortunately, we cannot tune the frequency of our magnetic heater to match a NC, so instead we would need to synthesize NC at the precise size needed to couple with the heater. This seemed impractical, and so I moved onto other projects.

F.4 Confined-but-Connected Film Formation on PEG Functionalized Substrates

As I mentioned in Chapter 8, in addition to improving CBCs at the nm to μm scale, we should also investigate ways to make larger area CBCs. Through a collaboration with Prof. Ober, we investigated assembling CBCs on silicon wafers that were functionalized with a polyethylene glycol brush on the surface. The idea was that PEG brushes should present similar surface chemistry to the ethylene glycol subphase

used in CBC assembly and so may provide NC with additional mobility needed to form CBCs.

The open ended question for this work was how to deliver the EDA. Because the PEG brushes were only ~100nm thick, EDA could not be injected into the PEG layer like it is injected into the subphase. We tried a variety of EDA delivery methods, soaking the PEG in EDA before assembling a film, a standard ligand exchange procedure with dilute EDA in acetonitrile, and vapor phase delivery of EDA, as diagrammed in Figure F.4a. Vapor phase delivery seemed to produce the results we were looking for, 100 oriented PbSe films as shown in the GIWAXS pattern in Figure F.4b. However, when I examined these films in the SEM I found that the PbSe NCs had become significantly larger as shown in Figure F.4d.

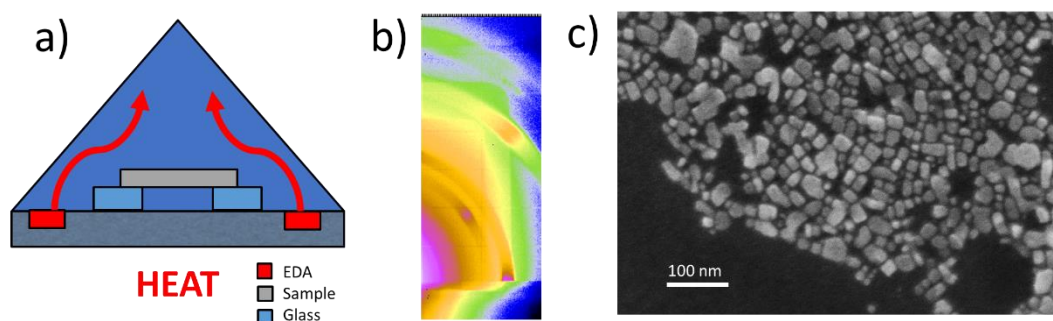


Figure F.4: a) Schematic of vapor phase EDA delivery b) GIWAXS of a NC film after EDA vapor treatment showing 100 up orientation c) SEM of the film showing very large, cubic PbSe NCs formed during EDA treatment

I believe that the excessive growth of PbSe NCs into ~20 nm cubes was due to condensation of EDA on the NC film. Because there was nowhere else for the EDA to go after it had removed ligands, it could continue to chelate Pb or Se ions and lead to way more particle growth than we were shooting for. As I mentioned in Chapter 8, I believe a better approach to large area fabrication of CBCs is through die slot coating that involves a nonpolar subphase. I think it is critical that the EDA-Pb-oleate complex has somewhere to go rather than sitting around and continuing to affect the NCs.

F.5 Magic to Magic Cation exchange

My undergraduate was interested in using the SILAR film growth method to fill the interstitial space between PbSe NCs with PbS. The idea was that by filling the ~30% of empty space in a close packed NC film with another absorbing material sunlight could be absorbed in a thinner film, and so photogenerated charges could be collected more easily. Initial experiments showed that PbS SILAR growth onto a PbSe film lead to a redshift in the excitonic peak as the quantum confinement was reduced by the growth of a shell material with only slightly higher bandgap.

The Shockley-Queisser maximal PV efficiency has a relatively flat maxima between about 1.5 eV and 1 eV. So, given that the PbS treatment would reduce the bandgap of the NC film, we wanted to start with as high a bandgap as possible. Because surface termination and passivation with Cd and Cl ions has been critical to improving performance in state of the art solar cells, I looked into the synthesis method used by Zhang et al to produce 6% PbSe cells fabricated in air⁶. Their method involved a cation exchange from CdSe particles to PbSe particles. The CdSe particles I synthesized were very small, with a very sharp absorption peak and seemed to match one of the last CdSe magic cluster families⁷. After cation exchange, the absorption peak of the PbSe NCs likewise seems to correspond to one of the previously observed PbSe magic cluster families⁸.

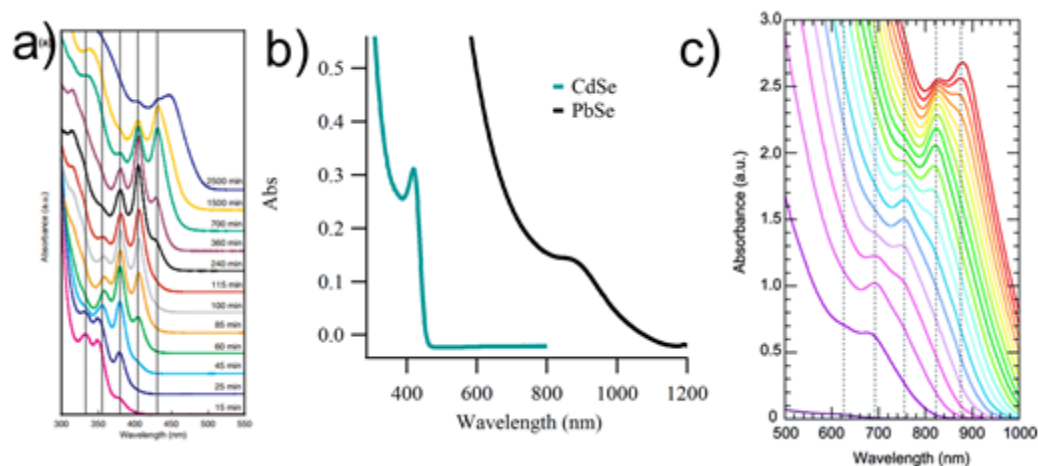


Figure F.5: a) CdSe magic clusters b) My magic clusters before (CdSe) and after (PbSe) cation exchange c) PbSe magic clusters. a) is adapted from ⁷ Copyright 2007 Wiley b) is adapted from ⁸ Copyright 2008 American Chemical Society

My undergraduate never continued the project to actually make solar cells, and I focused my SILAR related efforts on CBC structures. I think the potential to create PbX magic sized clusters from CdX clusters is exciting, especially in light of recent work in our group by Doug and Curtis. As I mentioned in Chapter 8, using magic sized building blocks is one possible way to eliminate disorder in CBCs.

REFERENCES

1. Smilgies, D.-M.; Heitsch, A. T.; Korgel, B. A. *The Journal of Physical Chemistry B* **2012**, 116, 6017-6026.
2. Heitsch, A. T.; Patel, R. N.; Goodfellow, B. W.; Smilgies, D.-M.; Korgel, B. A. *The Journal of Physical Chemistry C* **2010**, 114, 14427-14432.
3. Grouchko, M.; Kamyshny, A.; Mihailescu, C. F.; Anghel, D. F.; Magdassi, S. *ACS nano* **2011**, 5, 3354-3359.
4. Fischer, A.; Rollny, L.; Pan, J.; Carey, G. H.; Thon, S. M.; Hoogland, S.; Voznyy, O.; Zhitomirsky, D.; Kim, J. Y.; Bakr, O. M.; Sargent, E. H. *Adv. Mater.* **2013**, n/a-n/a.
5. Kovalenko, M. V.; Scheele, M.; Talapin, D. V. *Science* **2009**, 324, 1417-20.
6. Zhang, J.; Gao, J.; Church, C. P.; Miller, E. M.; Luther, J. M.; Klimov, V. I.; Beard, M. C. *Nano Lett.* **2014**, 14, 6010-6015.
7. Kudera, S.; Zanella, M.; Giannini, C.; Rizzo, A.; Li, Y.; Gigli, G.; Cingolani, R.; Ciccarella, G.; Spahl, W.; Parak, W. J. *Adv. Mater.* **2007**, 19, 548-552.
8. Evans, C. M.; Guo, L.; Peterson, J. J.; Maccagnano-Zacher, S.; Krauss, T. D. *Nano Lett.* **2008**, 8, 2896-2899.